

NOVEL IMPLANTABLE DISTRIBUTIVELY  
LOADED FLEXIBLE RESONATORS FOR  
MRI

A THESIS

SUBMITTED TO THE DEPARTMENT OF ELECTRICAL AND  
ELECTRONICS ENGINEERING  
AND THE GRADUATE SCHOOL OF ENGINEERING AND SCIENCES  
OF BILKENT UNIVERSITY  
IN PARTIAL FULLFILMENT OF THE REQUIREMENTS  
FOR THE DEGREE OF  
MASTER OF SCIENCE

By

Sayım Gökyar

August 2011

I certify that I have read this thesis and that in my opinion it is fully adequate, in scope and in quality, as a thesis for the degree of Master of Science.

---

Assoc. Prof. Dr. Hilmi Volkan Demir (Supervisor)

I certify that I have read this thesis and that in my opinion it is fully adequate, in scope and in quality, as a thesis for the degree of Master of Science.

---

Prof. Dr. Ergin Atalar

I certify that I have read this thesis and that in my opinion it is fully adequate, in scope and in quality, as a thesis for the degree of Master of Science.

---

Prof. Dr. Üstün Aydınöz

Approved for the Graduate School of Engineering and Sciences:

---

Prof. Dr. Levent Onural  
Director of Graduate School of Engineering and Sciences

**ABSTRACT**

**NOVEL IMPLANTABLE DISTRIBUTIVELY LOADED  
FLEXIBLE RESONATORS FOR MRI**

Sayım Gökyar

M.S. in Electrical and Electronics Engineering

**Supervisor:** Assoc. Prof. Dr. Hilmi Volkan Demir

August 2011

Magnetic resonance imaging (MRI) is an enabling technology platform for imaging applications. In MRI, the imaging frequency falls within the radio frequency (RF) range where the tissue absorption of electromagnetic power is conveniently very low (e.g., compared to X-ray imaging), making MRI medically safe. As a result, MRI has evolved into a major imaging tool in medicine. However, in MRI, it is typically difficult to receive a magnetic resonance signal from tissue near a metallic implant, which hinders imaging of the implant device neighborhood to observe, monitor, and make assessment of the recovery and tissue compatibility. This can be accomplished by using locally resonating implants, but such implantable local resonators compatible with MRI that simultaneously feature reasonable chip size are currently not available (although there are some MRI-guided catheter applications). In this thesis, we proposed and developed a new class of implantable chip-scale local resonators that operate at radio frequencies of MRI, despite their small size, for the purposes of enhancing the signal-to-noise ratio (SNR) and thus the resolution in their vicinity. Here we addressed the scientific challenge of achieving low resonance frequency while maintaining chip-scale size suitable for potential MR-compatible implants. Using only biocompatible materials (gold, nitrides, and silicon or polyimide) within a substantially reduced footprint (miniaturized by 2 orders of magnitude), we demonstrated novel chip-scale designs based on the basic concept of split ring resonators (SRRs). Different than classical SRRs

or those loaded with lumped elements (e.g., thin-film lumped loading), however, in our designs we loaded the SRR geometry in a distributive manner with a micro-fabricated dielectric thin-film layer to increase effective capacitance. For a proof-of-concept demonstration, we fabricated  $20\text{ mm} \times 20\text{ mm}$  resonators that operate at the resonance frequency of 130 MHz (compatible with 3 T MRI system) when distributively loaded with the capacitive film, which would otherwise operate around 1.2 GHz as a classical SRR of the same size if not loaded. It is worth noting that this resonance frequency of 130 MHz would normally require a classical SRR of  $20\text{ cm} \times 20\text{ cm}$ , a chip size 100-fold larger than ours. Designing and fabricating flexible thin-film resonators, we also showed that this architecture can be tuned by bending and is appropriate for non-planar surfaces, which is often the case for *in vivo* imaging. The phantom images indicated that, depending on the resonator configuration, these novel self-resonating structures increase SNR of the received signal by a maximum factor of 4 to 150 and over an enhancement penetration up to 10 mm into the phantom. This corresponds to a resolution enhancement in the 2D image by a factor of 2 to 12, respectively, under the same RF power. These *in vitro* experiments prove that it is possible to operate our local resonators at reduced frequencies via the help of distributive loading on the same chip. These findings suggest that proposed implantable resonator chips make promising candidates for self-resonating MR-compatible implants.

**Key Words:** Magnetic resonance imaging (MRI), thin film loading, MR-compatible implants, wearable MRI coils, inductively coupled radio frequency coils (ICRF).

ÖZET

MANYETİK REZONANS GÖRÜNTÜLEME ÇİN  
DA İLİMSAL YÜKLENİM İMPLANT EDİLEBİLİR  
ÖZGÜN ESNEK REZONATÖRLER

Sayım Gökyar  
Elektrik ve Elektronik Mühendisliği Bölümü Yüksek Lisans  
Tez Yöneticisi: Doç. Dr. Hilmi Volkan Demir  
Ağustos 2011

Manyetik rezonans görüntüleme (MRG), görüntüleme uygulamalarına imkan tanıyan bir teknoloji platformudur. MRG'nin görüntüleme frekanslarının dokuların elektromanyetik gücün emiciliğinin oldukça az olduğu radyo frekansı (RF) aralığında olması, MRG'yi diğer birçok yöntemle göre (örneğin: x-ray) sağlıklı açısından oldukça güvenli yapmaktadır. Bunun sonucu olarak da, MRG, yaygın bir tıbbi görüntüleme yöntemi haline gelmiştir. Ancak, MRG'de, canlı içindeki metalik implantların yakınlarından genellikle görüntü sinyalinin alınamıyor olması, bu yapıların çevresinin gözlenip, izlenmesine, iyileşmenin analizine ve yapıların doku uyumluluklarına bakılmasına engel olmaktadır. Bu durum, bölgesel olarak rezonans eden yapıların kullanılması ile çözülebilir, ama (her ne kadar MRG rehberli bazı girişimsel kateter uygulamaları varsa da) hem MR uyumlu hem de yeterince küçük boyutlarda bölgesel rezonatörler günümüzde mevcut değildir. Bu tezde, vücut içi implantların yakınında sinyal-gürültü oranını, dolayısıyla çözünürlüğü, artıracak küçük boyutlarına rağmen MRG frekanslarında çalışan yeni bir bölgesel rezonatör türünü önerip geliştirdik. Bununla, MR uyumlu olası implantlara uygun, yonga ebatlarında kalarak düşük rezonans frekansını elde edebilme problemini bilimsel olarak ele aldık. Yarık halka rezonatörlerin (YHR) temel mantığından hareketle, oldukça küçük bir baskı alanında (100 kat küçültülmüş alanda) yalnızca biyo-uyumlu malzemeler kullanarak (altın, nitrürler, ve silisyum veya polimit), yonga

ebatlarında özgün tasarımları gerçekleştirdik. Klasik YHR'lerden ya da bir noktadan elemanlarla yüklenmiş (örneğin, ince film noktasal yükleme) rezonatörlerden farklı olmanın yanında, tasarımlarımızda etkin kapasitif etkiyi artırmak için YHR geometrisini dağınık tarzda mikro-üretimle yapılmış yalıtkan ince-filmle yükledik. Kavramın kanıtının gösterimi için, standart YHR olması durumunda 1.2 GHz frekansında rezonans edecek, ancak dağınık olarak ince filmle yüklendiğinde (3T MRG sistemine uygun) 130 MHz'de rezonans eden, 20 mm × 20 mm ebatlarında, yapılar ürettik. Bu ebatların, standart YHR mimarisinin kullanılması durumunda, 130 MHz'de rezonans edebilmesi için tasarımımdan 100 kat daha büyük, 20 cm × 20 cm, olması gerekir. Ayrıca esnek ince-film yüklü rezonatörler tasarlayıp ve üretip, aynı zamanda bu yapının bükülerek akortlanabildiğini ve düzlemsel olmayan vücut içi yüzeylerin görüntülenmesi için uygun olduğunu gösterdik. Kendi kendine rezonans edebilen özgün yapılarımızın uzaydaki durumuna göre, fantom görüntüleri alınan sinyallerin iddetlerini en fazla 4 ile 150 kata kadar ve etki derinliğini de 10 mm'ye kadar artırılabilir olduğunu gösteriyor. Bu durum, aynı RF gücünü kullanarak, 2 boyutlu görüntülerde çözünürlüğü yaklaşık 2 ile 12 kat artırabilmeye karşılık geliyor. Bu test ortamındaki deneyler, bölgesel rezonatörlerin aynı yonga üstünde dağınık yüklenmeleri sayesinde çok daha düşük frekanslarda çalışmalarının mümkün olduğunu gösteriyor. Bu bulgular, vücut içine uygulanabilir rezonatör çiplerimizin MR uyumlu kendi kendine rezonans edebilen implantlar için kullanımını vaat ediyor.

**Anahtar Kelimeler:** Manyetik rezonans görüntüleme (MRG), ince film yükleme, MR uyumlu implantlar, giyilebilir MRG bobinleri, indüklenerek elde edilen radyo frekans (ERF).

# Acknowledgements

I would like to express my deepest appreciation to my supervisor Professor Hilmi Volkan Demir for his brilliant and wise comments on my research during this thesis. Not only his comments but also his endless energy and motivating personality propel me to work in a more disciplined way. He guided me through this blessed way that is long, tough and very difficult to finish without his help. I believe that the words are not enough to define his contributions to this thesis but in short, he is certainly one of the masters in his fields.

Human being crawled before he stands and walked before he runs. It is great pleasure for me to state my kind regards to Professor Ergin Atalar since he helped me to learn how to stand without crawling. He opened the doors of MRI to my life and helped us to use UMRAM (National MR Research Center) for our experiments. His invaluable discussions determined the milestones of this research work.

I would like to express my gratitude to Professor Üstün Aydınğöz for his interest and spending his valuable times to evaluate this thesis and give precious comments about it.

Although the way is long, it starts with a first step and it is important to have kind colleagues traveling with you. I would like to thank to each and every member of Devices and Sensors Group for their kind and eternal friendship. They are the indispensable part of this thesis.

I cannot forget thanking Biomedical Engineering Group members at UMRAM. They have trained me on how to use the scanner and allowed me to use their experimental workbenches.

I would like to express my special thanks to Dr. Rohat Melik for his help and synergy during my first steps in this way. His broad perspective on academic issues and sincere personality in nonacademic environment attracts me to imitate

him. Together with Dr. Melik, Emre Ünal is one of my heroes in this research work. His experience on microfabrication and talent on experimental work has allowed me to make an accelerated progress in my research work.

The most exciting part of the life is the present time, which shows the continuity of the research. Actually, I think it is the most exciting instant if the scientific research is making progress. We are not searching for ordinary reasons; we are researching for the wisdom of the matter, which I think triggers the astonishment of human being.

This is the right time for me to declare my appreciation to my family. We always need reasons to do things and all of my appreciation during this thesis work has valid and valuable reasons. However, there is no reason to thank my family, because they love me without any reason. Simply, Thank YOU.

This work is partially supported by TUBITAK BİDEB 2228.

# Table of Contents

<b>1. INTRODUCTION.....</b>	<b>1</b>
1.1 HISTORY AND BACKGROUND INFORMATION OF MRI.....	1
1.2 MOTIVATION AND THE SCOPE OF THE THESIS .....	1
<b>2. FUNDAMENTALS OF MRI.....</b>	<b>4</b>
2.1 BASIC CONCEPTS OF MRI.....	4
2.1.1 Physics of Spin.....	4
2.1.2 Frequency Characteristics of Different Nuclei .....	6
2.2 FIELDS OF MRI .....	7
2.2.1 Main Magnetic Field .....	7
2.2.2 Radio Frequency Magnetic Field.....	7
2.2.3 Gradient Fields.....	12
2.3 HARDWARE.....	13
2.3.1 Main Field Magnet.....	13
2.3.2 Gradient Field Electromagnets .....	14
2.3.3 RF Field Electromagnets .....	15
2.3.3.1 <i>Magneto Static Field Solutions for Birdcage Coil...</i>	<i>16</i>
2.3.3.2 <i>Equivalent Circuit Analysis of High Pass Birdcage</i>	
<i>Coil.....</i>	<i>20</i>
<b>3. RESONATORS.....</b>	<b>23</b>
3.1 LC RESONATORS.....	23
3.2 RING RESONATOR ANALYSIS.....	24
3.2.1 Electromagnetic Analysis .....	24
3.2.2 Resonance Frequency Analysis .....	31
3.3 RECTANGULAR SRR CHARACTERISTIC .....	33
<b>4. LOADING OF RESONATORS .....</b>	<b>36</b>
4.1 LUMPED ELEMENT LOADING .....	36
4.2 THIN FILM LOADING .....	39
4.3 ELECTROMAGNETIC ANALYSIS OF DISTRIBUTIVE LOADING .....	43

4.4 CIRCUIT EQUIVALENT ANALYSIS OF DISTRIBUTIVE LOADING .....	50
4.4.1 Lumped model .....	51
4.5 PHANTOM SIMULATIONS FOR LOSS TERM EFFECTS .....	58
<b>5. MRI OF DISTRIBUTIVELY LOADED RESONATORS .....</b>	<b>64</b>
5.1 MICRO-FABRICATION OF RESONATORS .....	64
5.1.1 Micro-fabrication of Resonators on a Rigid Substrate.....	65
5.1.2 Micro-fabrication of Resonators on a Flexible Substrate.....	70
5.2 RESONATORS EMPLOYED AS EXTERNAL DEVICES .....	73
5.3 RESONATORS EMPLOYED AS INTERNAL DEVICES .....	84
5.3.1 Phantom Imaging Using Classical Resonator.....	84
5.3.2 Phantom Imaging Using Novel Rigid Resonators .....	85
5.3.3 Phantom Imaging Using Novel Flexible Resonators .....	89
5.3.3.1 <i>Planar Imaging with the Flexible Resonators</i> .....	89
5.3.3.2 <i>Nonplanar Imaging with the Flexible Resonators</i> <i>Having Different Curvatures</i> .....	94
<b>6. CONCLUSIONS AND FUTURE WORK.....</b>	<b>108</b>
<b>7. BIBLIOGRAPHY .....</b>	<b>112</b>

# List of Figures

Figure 2.1 Definition of spin from a) quantum mechanical and b) classical mechanics perspectives, with c) excited spin, rotating along B axis.....	5
Figure 2.2 Excited spin with transverse magnetization and receiving coils.....	8
Figure 2.3 Longitudinal and transverse magnetization of fat after RF excitation.....	11
Figure 2.4 Transverse magnetizations of fat and muscle after excitation.....	11
Figure 2.5 Effect of the gradient field on emitted signal to extract spatial point of sources. ....	13
Figure 2.6 A single excitation spin echo imaging sequence.....	14
Figure 2.7 Coil placements of an MRI Scanner. ....	16
Figure 2.8 Example of a low pass birdcage coil.....	16
Figure 2.9 B field distributions for different dimensions of square loops.....	18
Figure 2.10 Circuit equivalent of high pass birdcage coil. ....	20
Figure 3.1 Series RLC circuit. ....	23
Figure 3.2 Structure of a circular resonator a) a closed ring resonator and b) a split ring resonator. ....	24
Figure 3.3 Field maxima of ring resonators for their first two modes: a) for $n=1$ , b) for $n=2$ , c) for $n=1.5$ , and d) for $n=2$ . ....	26
Figure 3.4 Footprint of a) circular b) rectangular SRRs. ....	27
Figure 3.5 Transmission of a circular SRR.....	28

Figure 3.6 Current distribution of the circular SRR at different frequencies: a) at 100 MHz, b) at 500 MHz, c) at 900 MHz, d) at 1.1 GHz, e) at 1.5 GHz (on resonance), and f) 2.0 GHz. ....	29
Figure 3.7 Electric field distributions of the circular SRR at different frequencies: a) at 100 MHz, b) at 500 MHz, c) at 900 MHz, d) at 1.1 GHz, e) at 1.5 GHz, f) at 2.0 GHz,.....	30
Figure 3.8 First two modes of circular SRR for different gap widths. ....	31
Figure 3.9 Resonance frequency as a function of the gap size for the circular SRR. ....	32
Figure 3.10 Effective capacitance due to gap size.....	33
Figure 3.11 Transmission characteristics of the circular and rectangular SRRs. ....	34
Figure 3.12 Complete field comparisons of the circular and rectangular resonators on resonance: E field of a) the rectangular SRR and b) the circular SRR, and.....	35
Figure 4.1 Normalized transmission of the rectangular SRR with a footprint of 20 cm by 20 cm. ....	36
Figure 4.2 a) E-field and b) current distribution of the rectangular SRR at resonance frequency. ....	37
Figure 4.3 Transmission spectrum of the rectangular SRR for different lumped capacitances.....	38
Figure 4.4 Cross-section view of metal-tissue boundary.....	40
Figure 4.5 Our rectangular SRR with distributively thin film loading. ....	42

Figure 4.6 Cross section view of SRR with thin film loaded region. .....	43
Figure 4.7 Normalized transmission of SRR for a dielectric film thickness of 500 $\mu\text{m}$ .....	44
Figure 4.8 Amplitude of E-field distribution: a) on the lower ring and b) on the upper overlay at the resonance frequency. ....	45
Figure 4.9 Current distribution of SRR at the resonance frequency.	45
Figure 4.10 Normalized transmission of the partially loaded SRR for various dielectric film thicknesses. ....	46
Figure 4.11 Layout of a fully distributively loaded resonator (almost one full turn).....	47
Figure 4.12 E-field and current distribution for the novel structure for a) E-field amplitudes on the lower ring at resonance frequency, b) current distribution on resonance, c) E-field distribution on the dielectric region, d) a closer look at the current directions on resonance, e) E-field distribution on the upper ring, and f) current distribution of the second mode. ....	49
Figure 4.13 Transmission of fully distributively loaded SRR for various dielectric film thicknesses. ....	50
Figure 4.14 Proposed unit cell configuration for distributive loading. .....	52
Figure 4.15 Circuit equivalent of structure for $n=1$ .....	52
Figure 4.16 Circuit response for $n=1$ . ....	53
Figure 4.17 Unit cell representation for $n=2$ . ....	53
Figure 4.18 Circuit response for $n=2$ . ....	54
Figure 4.19 Circuit equivalent for $n=4$ .....	54
Figure 4.20 Modified circuit equivalent for $n=4$ .....	55

Figure 4.21	Frequency response of the modified circuit for $n=4$ .....	55
Figure 4.22	Circuit equivalent for $n=16$ .....	56
Figure 4.23	Frequency response of the equivalent circuit for $n=16$ .....	57
Figure 4.24	Sample unit cell including the loss parameters. ....	58
Figure 4.25	Simulation layout for lossy environment. ....	59
Figure 4.26	Cross section of the simulation environment (not drawn to on scale). ....	59
Figure 4.27	Transmission of a distributive loaded resonator inside the phantom. ....	60
Figure 4.28	Electric field distribution of the structure for different planes: a) 1 mm inside the phantom on the back, b) at the bottom ring, c) in the middle of the plates, and d) at the top ring .....	62
Figure 4.29	Current distribution of the structure.....	62
Figure 5.1	Layout of our chrome coated quartz mask for the lower ring (the first metal layer). ....	66
Figure 5.2	Layout of the chrome coated quartz mask for the upper ring (the second metal layer).....	68
Figure 5.3	Process flow for fabrication on a rigid substrate. ....	69
Figure 5.4	Process flow for fabrication on a flexible substrate.....	72
Figure 5.5	MRI of the resonators with a flip angle of $5^\circ$ . ....	75
Figure 5.6	Intensity level distribution along the horizontal axes of the resonators. ....	75
Figure 5.7	MRI of the resonators with a flip angle of $10^\circ$ . ....	76
Figure 5.8	Intensity level distribution along the horizontal axes of the resonators. ....	76
Figure 5.9	MRI of the resonators with a flip angle of $15^\circ$ . ....	77

Figure 5.10 Intensity level distribution along the horizontal axes of the resonators.....	77
Figure 5.11 MRI of the resonators with a flip angle of 20°.....	78
Figure 5.12 Intensity level distribution along the horizontal axes of the resonators.....	78
Figure 5.13 MRI of the resonators with a flip angle of 25°.....	79
Figure 5.14 Intensity level distribution along the horizontal axes of the resonators.....	79
Figure 5.15 MRI of the resonators with a flip angle of 50°.....	80
Figure 5.16 Intensity level distribution along the horizontal axes of resonators. ....	80
Figure 5.17 Intensity amplification of the resonators for different flip angles. ....	81
Figure 5.18 Enhancement factor due to flip angle excitation. ....	83
Figure 5.19 Enhancement limit for external imaging due to different flip angles. ....	83
Figure 5.20 A sample image of an SRR inside the phantom. ....	84
Figure 5.21 MRI of the novel resonating structure on a rigid substrate for a flip angle of 5°.....	85
Figure 5.22 MRI of the novel resonator structure on a rigid substrate for 10° flip angle.....	86
Figure 5.23 MRI of the novel resonator structure on a rigid substrate for 15° flip angle.....	86
Figure 5.24 MRI of the novel resonator structure on a rigid substrate for a flip angle of 20°.....	87
Figure 5.25 MRI of the novel resonator structure on a rigid substrate for a flip angle of 45°.....	87

Figure 5.26 Characteristic of rigid resonator due to different flip angles. ....	88
Figure 5.27 MRI of the novel resonator structure on a flexible substrate for 5° flip angle (planar configuration).....	89
Figure 5.28 MRI of the novel resonator structure on a flexible substrate for 10° flip angle (in planar configuration).....	90
Figure 5.29 MRI of the novel resonator structure on a flexible substrate for 15° flip angle (in planar configuration).....	90
Figure 5.30 MRI of the novel resonator structure on a flexible substrate for 20° flip angle (in planar configuration).....	91
Figure 5.31 MRI of the novel resonator structure on a flexible substrate for 45° flip angle (in planar configuration).....	91
Figure 5.32 Comparison of the flexible and rigid resonators for different flip angles.....	92
Figure 5.33 Enhancement factor of the resonators for different flip angles. ....	93
Figure 5.34 Enhancement limit for internal planar imaging due to different flip angles.....	93
Figure 5.35 Sketch of the flexible resonator. ....	95
Figure 5.36 Side view of the bent resonator.....	95
Figure 5.37 MRI of the bent resonator for 5° flip angle (in nonplanar configuration).....	96
Figure 5.38 MRI of the bent resonator for 10° flip angle (in nonplanar configuration).....	96
Figure 5.39 MRI of the bent resonator for 15° flip angle (in nonplanar configuration).....	97

Figure 5.40 MRI of the bent resonator for 20° flip angle (in nonplanar configuration).....	97
Figure 5.41 MRI of the bent resonator for 45° flip angle (in nonplanar configuration).....	98
Figure 5.42 Maximum intensity characteristics of the bent resonator for different flip angles (in nonplanar configuration). ....	99
Figure 5.43 Enhancement factor of the bent structure with a curvature of 83.3 m <sup>-1</sup> (in nonplanar configuration). ....	99
Figure 5. 44 Enhancement limit of the bent structure with a curvature of 83.3 m <sup>-1</sup> (in nonplanar configuration). ....	100
Figure 5.45 Side view of the flipped and bent resonator. ....	100
Figure 5.46 MRI of the flipped and bent resonator for 1° flip angle (in nonplanar flipped configuration). ....	101
Figure 5.47 MRI of the flipped and bent resonator for 2° flip angle (in nonplanar flipped configuration). ....	101
Figure 5.48 MRI of the flipped and bent resonator for 3° flip angle (in nonplanar flipped configuration). ....	102
Figure 5.49 MRI of the flipped and bent resonator for 4° flip angle (in nonplanar flipped configuration). ....	102
Figure 5.50 MRI of the flipped and bent resonator for 5° flip angle (in nonplanar flipped configuration). ....	103
Figure 5.51 MRI of the flipped and bent resonator for 10° flip angle (in nonplanar flipped configuration). ....	103
Figure 5.52 MRI of the flipped and bent resonator for 15° flip angle (in nonplanar flipped configuration). ....	104
Figure 5.53 MRI of the flipped and bent resonator for 20° flip angle (in nonplanar flipped configuration). ....	104

Figure 5.54 MRI of the flipped and bent resonator for 25° flip angle (in nonplanar flipped configuration). .....	105
Figure 5.55 MRI of the flipped and bent resonator for 45° flip angle (in nonplanar flipped configuration). .....	105
Figure 5.56 Characteristic of bent resonator due to different flip angles. ....	106
Figure 5.57 Enhancement factor of the bent structure with a curvature of 166.7 m <sup>-1</sup> (in nonplanar configuration).....	107
Figure 5. 58 Enhancement limit of the bent structure with a curvature of 166.7 m <sup>-1</sup> (in nonplanar configuration). ....	107
Figure 6.1 A novel flexible resonator designed in the shape of a crescent moon for MR imaging. ....	110

# List of Tables

Table 2.1 Gyromagnetic ratios and sensitivities of H, C, F, N and P atoms.....	6
Table 2.2 Relaxation time values for some of the tissues at 1.5 and 3.0 T.....	10
Table 4.1 Comparisons of computed resonance frequencies L is calculated as 60 nH [14]. .....	39
Table 4.2 Resonance frequencies changing due to the different dielectric film thicknesses.....	46

# Chapter 1

## INTRODUCTION

### 1.1 History and Background Information of MRI

The short story of magnetic resonance imaging (MRI) started early 1970s, with the seminal work of Paul Lauterbur, which was later awarded a Nobel Prize in 2003. This late payback was due to the great contribution of Lauterbur to the nuclear magnetic resonance (NMR) instead of MRI. Relatively long story of NMR started at the beginning of this century. Upon discovery of spins, the relationship between the magnetic field and the resonance frequency of these spins was first explained by the Irish physician, Joseph Larmor. (His governing equation will be given and explained in the second chapter of this thesis.)

However, the real inventors of NMR were different; it took almost 50 years to propose the idea that this property can be used to identify different materials. In 1946, two genius researchers, Felix Bloch from Stanford University [1] and Edward Mills Purcell from Harvard University [2], independently achieved the first NMR identification of materials for liquids and solids. They shared the Nobel Prize in physics in 1952 [3]. This is the starting point of NMR for chemical identification and new concepts have been investigated to understand material behavior under magnetic field since then.

Humanity would have to wait until 1973 to see the first MRI of medical tissues [8]. The name of the hero, who has realized this dream, was Paul Lauterbur. His inventions of magic fields, called gradient fields, are still one of the greatest research topics of MRI community [4].

### 1.2 Motivation and the Scope of the Thesis

This thesis aims to design and demonstrate a new class of self-resonating chip-scale structures that operate at the predetermined frequency of MRI and the characterization of these resonators both for in-phantom and ex-phantom cases.

Analysis under both conditions is necessary to foresee potential applications of these novel structures. The external case can be a starting point for wearable antennas while the internal case can be a milestone for self-resonating MRI compatible implants, where the latter has never been investigated in the literature to date.

Obtaining MRIs with high resolution without increasing the acquisition time and decreasing its SNR is a challenging task in most of the cases. For the treatment of epilepsy diseases, it is a common method to use subdural electrodes to image defected parts of the brain, where the positioning of the electrodes has crucial importance for the surgery [5]. The correct positioning of subdural electrodes, which cannot be seen in MRI without MR visible coatings, determines the success of the surgery.

Classical solution to this problem requires two steps to estimate the position of the subdural electrodes correctly. The first step requires the MRI, which shows the details of the brain clearly, of the environment for the mapping of soft tissues. The second step includes the computerized tomography (CT) of the metallic electrodes with the skull to map their positions on the brain. By using both of the images, approximate places of the electrodes obtained and the surgery area is determined due to these observations.

To determine the positions of subdural electrodes using only MRI, we propose the distributively loaded thin film resonating structures that can be implanted to the body with the subdural electrodes during the pre-surgical evaluation period. This method allows one to evaluate the positions of the electrodes without using CT images and with a great correctness. To achieve this, we designed, fabricated and characterized a chip-scale resonating structure, which can be further used for implantable devices for other surgical procedures.

This thesis starts with a short introduction to MRI presenting its fundamental principles and imaging methods (Chapter 2). This brief introduction prepares readers to be familiar with the relationship between the material types and their MRIs. It continues with the magnetic fields of MRI and their coils for imaging.

A relatively detailed analysis of RF coils stresses the importance of resonance and reviews the main properties of an antenna for MRI.

In the following chapter, Chapter 3, the classical resonance characteristics of conventional resonators are investigated and their complete electromagnetic analysis with simulations is provided. The circuit equivalent model and the current distributions together with the electric field confinement properties of split ring resonators (SRRs) are also presented here.

Chapter 4 introduces the new method of thin film distributive loading for local resonators to achieve lower resonance frequencies. It further continues with the detailed electromagnetic and circuit equivalent analysis of these self-resonating structures, called distributively loaded resonators. A unit cell approach and cascaded system models are given for and the characteristic analysis based on the given circuit models are performed using circuit theory simulation tools.

Finally, Chapter 5 deals with the explanation of microfabrication processes for different designs and their characterization using MRI. Tuning of these structures to 123 MHz for 2.89 T MRI system at UMRAM [6] and their mechanical properties are discussed and then the detailed analysis of these resonators explained. Experimental work is presented in this chapter for resonators serving as external and internal devices. Phantom images for different flip angles and different device configurations are analyzed and the most striking images are included. The thesis is completed with concluding remarks and outlook in Chapter 6.

# Chapter 2

## FUNDAMENTALS of MRI

Before the seminal work of Lauterbur in 1973, NMR was a powerful method to understand the content of gaseous mixtures that can only achieve material identification. A clear understanding of NMR was necessary to figure out the basic principles of MRI that is described as the behavior of a nucleus under a certain magnetic field. The details of NMR can be accurately explained by quantum mechanics. Here, we will explain NMR using the principles of classical mechanical model with the contribution of quantum mechanics.

### 2.1 Basic Concepts of MRI

#### 2.1.1 Physics of Spin

Quantum mechanics defines a fundamental property of nucleus called spin, which is due to the rotation of protons along their axis. From a classical mechanics perspective, this rotating positively charged small object with a mass exhibits angular momentum in the direction of rotation axis, and its net charge movement will result in current, which in turn, produces a magnetic field. Therefore, if we apply an external magnetic field to the proton, its angular momentum will be aligned along the direction of the applied field. Quantum mechanics explains the magnetic resonance by using the notion of energy quantization. It states that, when an external magnetic field is applied to a system, the energy levels of this system will be divided into two distinct energy levels. These defined levels are  $-1/2$  (the highest energy state, against magnetic field direction) and  $+1/2$  (the lowest energy state, through magnetic field direction). The energy difference between these two states is given by Equation (2.1).

$$\Delta E = \frac{h}{2\pi} \omega \quad (2.1)$$

where  $h$  is the Planck's constant and  $\omega$  is the angular frequency (in rad/s) corresponding to the spinning frequency of the proton. For a nucleus with an even number of spins, each of every two protons has opposite energy level that cancels each other and results in zero net magnetic moment ( $\vec{m}_s$ ). Such nuclei do not interact with the external magnetic field; thus, we are not interested in these atoms. On the other hand, atoms with odd number of protons exhibit good NMR characteristics and it is impossible to obtain zero net magnetic moment for any configuration of their spins. To visualize these, let us have a look at Figure 2.1

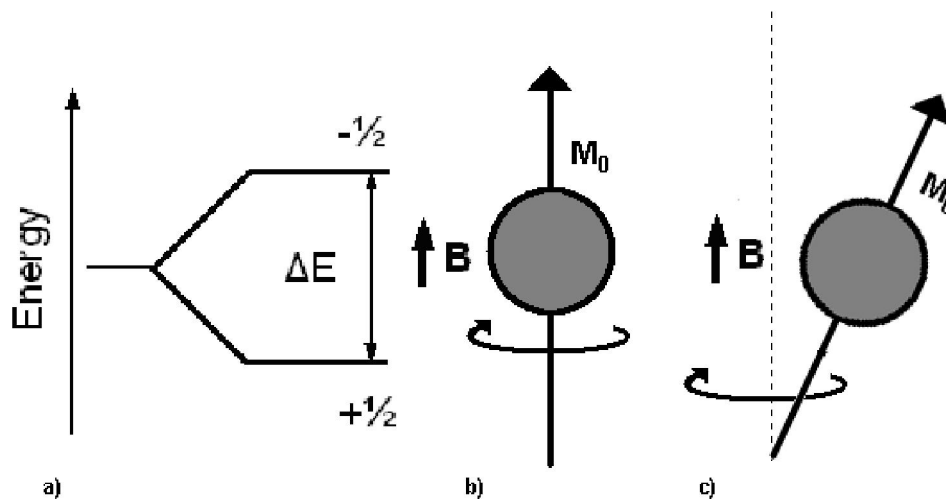


**Figure 2.1 Definition of spin from a) quantum mechanical and b) classical mechanics perspectives, with c) excited spin, rotating along B axis.**

Here,  $\vec{B}$  represents the magnetic field vector and  $\vec{M}$  is the total magnetization vector of nuclei with amplitude of  $M_0$ . If it is a single  $^1\text{H}$ , then it is the magnetization of a single proton and can be represented by  $\vec{m}_s$ . Total net magnetization ( $M_0$ ) is the macroscopic parameter, as opposed to the magnetization of a single atom ( $\vec{m}_s$ ), for materials with many nuclei.

## 2.1.2 Frequency Characteristics of Different Nuclei

At the beginning of the 20<sup>th</sup> century, Joseph Larmor (1857), an Irish physician, proposed a formula that defines the relationship between the external magnetic field and the angular frequency of the spins as given in Equation (2.2).

$$\omega = \gamma B \quad (2.2)$$

Here,  $B$  is the magnetic field intensity (tesla) and  $\omega$  is the angular frequency (rad/s) of the nuclei. This expression emphasizes the linear relationship between the rotational frequency and the external magnetic field with a characteristic coefficient known as gyromagnetic ratio ( $\gamma$ ). The gyromagnetic ratios and sensitivities of some atoms are given in Table 2.1 [7]. Sensitivity of an atom is defined as the MRI signal emission ratio of an atom after excitation.

Atom	<sup>1</sup> H	<sup>13</sup> C	<sup>19</sup> F	<sup>23</sup> N	<sup>31</sup> P
$\gamma/2$ (MHz/T)	42.575	10.705	40.054	11.262	17.235
Relative Sensitivity	1.000	0.016	0.830	0.093	0.066

**Table 2.1 Gyromagnetic ratios and sensitivities of H, C, F, N and P atoms.**

After these explanations, we now explain medical imaging frequencies. Hydrogen atom (<sup>1</sup>H), which is abundant in all organic tissues, has the key role in determining the operating MR frequency. Commercially available MRI scanners with  $B$  of 1.5 T and 3 T are commonly used at the corresponding hydrogen resonance frequencies of 63.8 and 127.7 MHz, respectively. Depending on typical  $B$  values adapted in the MRI, the imaging frequency falls within the radio frequency (RF) range where the tissue absorption of electromagnetic (EM) power is conveniently very low (e.g., compared to X-ray imaging).

## **2.2 Fields of MRI**

### **2.2.1 Main Magnetic Field**

As we mentioned in the previous section, the direction of magnetic moment of the spins will be parallel to the direction of the magnetic field, thus having non-zero net magnetization. Since the net macroscopic magnetic moment ( $\mathbf{M}_0$ ) is the summation of microscopic magnetic moments, which are randomly oriented in the absence of external magnetic field with zero net magnetization, it will be an obligation to apply a unidirectional, time independent (DC), homogeneous magnetic field. Nuclei under such a homogeneous field will exhibit uniform magnetization vector pointed in the magnetic field (B) direction called the longitudinal direction, which is commonly taken as the z-direction. It should be noted that DC magnetic field, which is used to obtain a total net nonzero magnetization, does not excite the spins to transmit magnetic energy to the environment. To sum up, we only have magnetized spins resonating at a Larmor frequency inside the given DC field (Figure 1.b), but not rotating along any axis or emitting any signal to capture for imaging.

As mentioned earlier, commercially available MRI scanners for medical imaging with magnetic flux densities (B) from 0.1T to 3 T are commonly used at the corresponding hydrogen resonance frequencies from 4.26 MHz to 127.7 MHz, respectively. There are also high field NMR scanners with the B field strength of up to 25 T for material identification.

### **2.2.2 Radio Frequency Magnetic Field**

As we see in Figure 1.b, DC magnetic field causes nucleus to spin along its direction. The excitation of spins, in other words their rotation along longitudinal direction, should be achieved to allow them to transmit their magnetization as illustrated in Figure 1.c. Since nuclei are spinning at the given Larmor frequency, the excitation signal should also be have the same frequency to rotate spins coherently. Now we have the combination of two motions,

rotation along the longitudinal axis and spinning along this rotating axis at the same frequency. Flip angle, the angle between the magnetization vector ( $M_0$ ) and the longitudinal direction, will determine the amount of signal that will be transmitted to the receiver antennas, located at the transverse plane, as sketched in Figure 2.2.

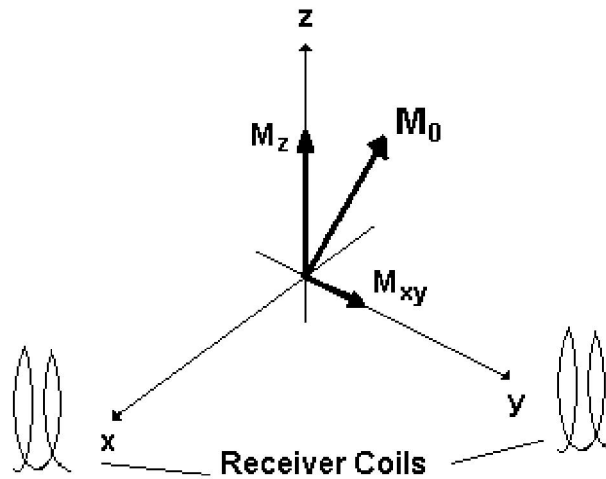


**Figure 2.2 Excited spin with transverse magnetization and receiving coils.**

In three-dimensional space, the excited magnetization vector will have components not only in z-direction, but also on x-y plane. If the value of flip angle is  $90^\circ$  then the magnetization vector will completely lie on the transverse plane. The net magnetization can now be implemented by two components,  $M_z$  and  $M_{xy}$ . The rotating nature of magnetization, not the spinning, will result in net current, thus an electromagnetic radiation emitted from the nuclei at the Larmor frequency can be detected by the receiver antennas. In MRI systems, the excitation typically takes place in the first few milliseconds and the rest of the duration before the next excitation is reserved for signal reception, which can last for several seconds.

After the excitation of nuclei, rotation of spins along longitudinal axis will continue only for a certain amount of time. Since there is a time invariant magnetic field in the z-direction, the net magnetization will tend to be aligned

along the z-direction, which is known as recession. We can infer that the transverse magnetization will decrease as the time elapses, resulting in decreased signal reception over time. On the other hand, longitudinal magnetization will increase to its initial value,  $M_0$ . The nature of recession is identified by two specific coefficients, T1 and T2, called longitudinal and transverse relaxation constants, respectively. At this point, we should have a short look at the Bloch equation.

Assume  $\vec{M}(t)$  is defined with its scalar components  $M_x$ ,  $M_y$  and  $M_z$  in the directions of x, y and z, respectively. For the sake of simplicity, we will be using i, j and k for the directions of x, y and z; then, the popular Bloch equation can be written as in Equation (2.3):

$$\frac{d\vec{M}}{dt} = \vec{M} \times \gamma \vec{B} - \frac{M_x \hat{i} + M_y \hat{j}}{T2} - \frac{(M_z - M_0) \hat{k}}{T1} \quad (2.3)$$

When we analyze this differential equation separately, we can express the longitudinal relaxation as in Equation (2.4).

$$\frac{dM_z}{dt} = -\frac{M_z - M_0}{T1} \quad (2.4)$$

This has the solution in the form of exponential function as follows:

$$M_z(t) = M_0(1 - e^{-t/T1}) \quad (2.5)$$

The transverse relaxation equation becomes as in Equation (2.6).

$$\frac{dM_{xy}}{dt} = -\frac{M_{xy}}{T2} \quad (2.6)$$

with a solution given as:

$$M_{xy}(t) = M_0 e^{-t/T2} \quad (2.7)$$

where  $M_{xy}$  is the vector summation of  $M_x$  and  $M_y$  and given in Equation (2.8)

$$M_{xy} = \hat{i}M_x + \hat{j}M_y \quad (2.8)$$

Equation 2.8 states that the vectorial summation of transverse magnetization decays exponentially. From previous explanations, we already know that it is also a rotating field due to the left hand rule, which means that another time dependent parameter should be added. Mathematical expressions for a complete solution are given as follows [7].

$$M_{xy} = M_0 e^{-t/T2} e^{-i2\pi f_0 t} \quad (2.9)$$

Typical relaxation time values for some of the tissues are summarized in Table 2.2 both for 1.5 and 3.0 T magnetic field strengths [8].

Tissue	1.5 T		3.0 T	
	T2 (ms)	T1 (ms)	T2 (ms)	T1 (ms)
Gray matter	100	900	100	1820
White matter	92	780	70	1084
Muscle	47	870	45	1480
Fat	85	260	83	490
Liver	43	500	42	812

**Table 2.2 Relaxation time values for some of the tissues at 1.5 and 3.0 T.**

By Equations 2.5 and 2.7, we can calculate the longitudinal and transverse components of magnetization for fat with unity initial magnetization ( $M_0$ ) at 1.5 T as shown in Figure 2.3.

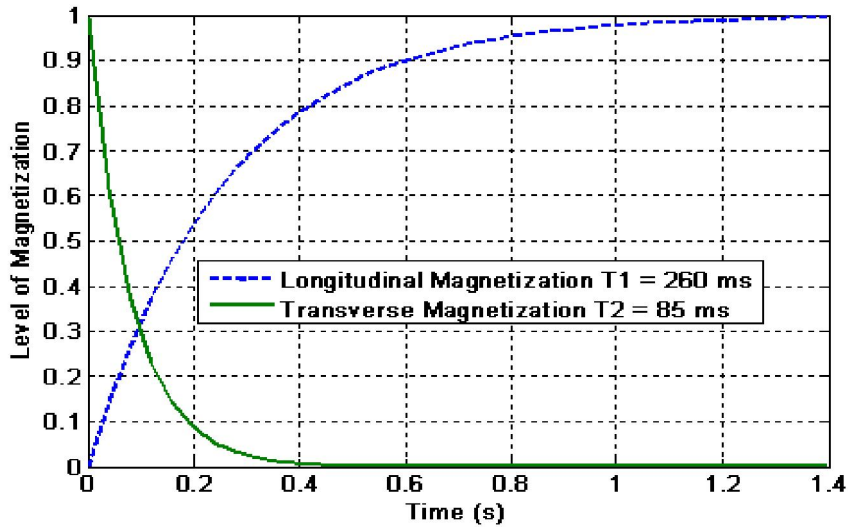


Figure 2.3 Longitudinal and transverse magnetization of fat after RF excitation.

As clearly seen from Figure 2.3, the transverse magnetization decays very fast, which means its imaging signal should be recorded at the beginning of the excitation. To understand the importance of relaxation parameters, let us have a look at the Figure 2.4 for contrast between different tissues.

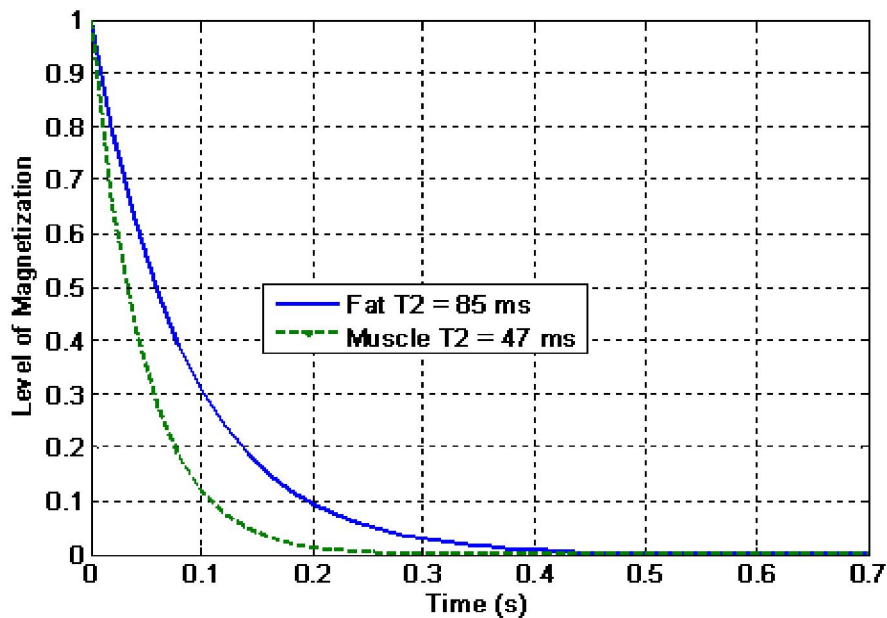


Figure 2.4 Transverse magnetizations of fat and muscle after excitation.

Figure 2.4 states that, under the same imaging conditions, the decay of transverse magnetization of fat is slower than the decay of transverse magnetization of muscle. We can roughly claim that, with the same amount of nuclei, fat will emit more signal than muscle at any instant of imaging due to its slowly decaying transverse magnetization thus can be seen brighter than muscle in the received image. However, we have to remember that it is too early to speak about the contrast between tissues since the opposite can also happen due to the other imaging parameters.

### 2.2.3 Gradient Fields

It is clear that the material identification can be achieved by using static and RF magnetic fields due to the characteristic coefficients of materials such as:  $\gamma$ , T1 and T2,. However, mapping the spatial distribution of materials, locating the signal sources in three-dimensional spaces, is not possible with only these two fields. Since the signal coming from all of  $^1\text{H}$  nuclei in any substance has the same frequency, the receiver coils will detect a signal that has a single frequency and amplitude. By using amplitude data, it will be possible to obtain, which substances are being imaged, but their physical coordinates cannot be determined.

Paul Christian Lauterbur, an American chemist, proposed that introducing gradient fields into the imaged medium would make it possible to map the sources of emitted signals. It was the beginning of 70's when he first obtained the first medical MRI images [9]. Later on his awesome work was awarded with a Nobel Prize in Physiology or Medicine in 2003, shared with Peter Mansfield [10].

Introducing gradient fields to the imaging medium will change the spinning frequency of nuclei that results in a bandwidth of absorbed/emitted signal. The detected signal now has different frequencies associated with their physical coordinates and amplitudes related to their material types.

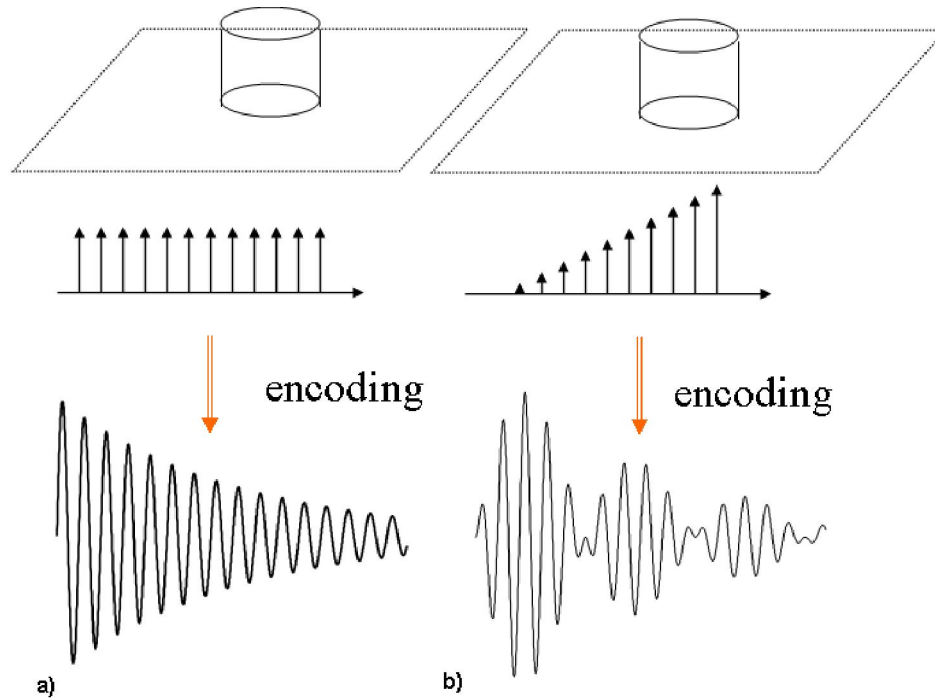


**Figure 2.5 Effect of the gradient field on emitted signal to extract spatial point of sources.**

Figure 2.5a, shows an exponentially decaying signal with a single frequency, whereas the Figure 2.5b shows another decaying signal, which seems to be a modulated by another frequency. Due to the bandwidth of the emitted fields from nuclei, Fourier transform of this modulated signal will be in rectangular, with each of its frequencies corresponding to a spatial point in space. The detailed mathematical expressions related to the gradient fields and RF excitation can be found in [Ref 7](#).

## 2.3 Hardware

### 2.3.1 Main Field Magnet

Since the main magnetic field determines the resonance frequency, this magnet can be renamed as the identity of the system. Although permanent magnets can be used as the open coils for the patients with claustrophobia, this is mostly an electromagnet constructed as a solenoid to produce uniform magnetic field

inside it. To eliminate non-uniformities due to other equipment, shimming coils are also included inside [11].

### 2.3.2 Gradient Field Electromagnets

As we mentioned in the previous section, gradient fields are responsible for image construction. They are effective at slice selection, determination of phase and frequency distribution. Their dimensions are comparable with the scanner's, and thus they have very high inductance that can create high voltages in the case of instant current deviations. Since they are working only at the specific instances of imaging, they should easily be turned on and turned off. For a typical imaging sequence as shown in Figure 2.6, gradient fields are generally activated in the range of T2 duration, which is too short to switch on and off such a high inductance. There are sophisticated circuitry and physical designs such as including shielding of coils that overcome such problems [12].

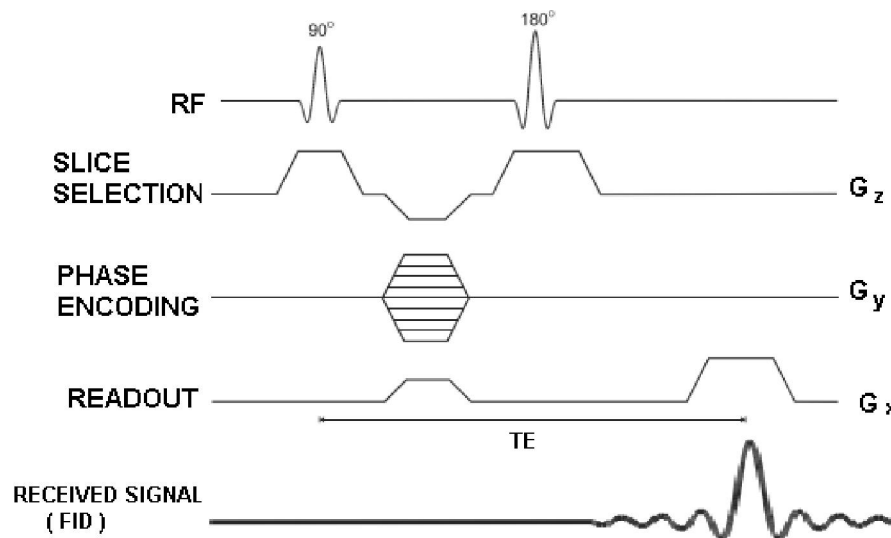


Figure 2.6 A single excitation spin echo imaging sequence.

In Figure 2.6, slice selection should be performed simultaneously with the RF excitation. Direction of the applied gradient field determines the orientation of the imaging plane and the rest of two gradient fields will be responsible from frequency and phase distributions. Free induction decay (FID) is the NMR signal that is emitted from the imaged object to be used for imaging. TE is the instant at which the signal emitted from the nuclei becomes the maximum and the hardware of the scanner is adjusted to receive and store the data.

### **2.3.3 RF Field Electromagnets**

This is the most interesting topic about the electromagnetic of MRI. This topic is much more complicated than we are interested; we will only introduce the necessary information and focus on the current distribution of electrically resonating structures. Since nuclei are spinning at Larmor frequency along magnetic field, to achieve the resonance condition, it should be excited at the same frequency to rotate along the same axis. We already mentioned that the angular momentum, in other words the magnetization vector, of the spin would be directed toward the magnetic field direction. If we apply a transverse magnetic field to the system, the resultant field will make an angle, called the flip angle, with the longitudinal direction. If the amplitude of transverse magnetic field is rotating in x-y plane, then the tip of the magnetization vector will also follow that resultant field at the frequency of rotation. If these rotational and spinning frequencies are the same, then the magnetic resonance condition will occur. To achieve this condition, several coils will be placed perpendicular to the radial direction of the imaging space and will be turned on and off sequentially. There are fantastic RF designs, for example, called birdcage coils that have uniform field distribution in the region of interest. Birdcage coils also combine the coils by proper electrical connection, leading to a single structure that resonates at the necessary frequency band. The principle MRI magnet configuration can be seen in Figure 2.7 and a low pass birdcage coil is shown in Figure 2.8.

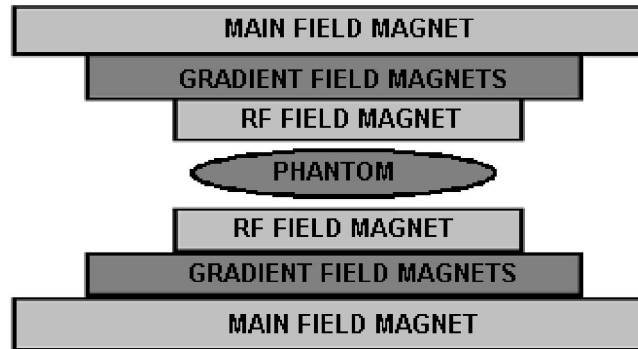


Figure 2.7 Coil placements of an MRI Scanner.

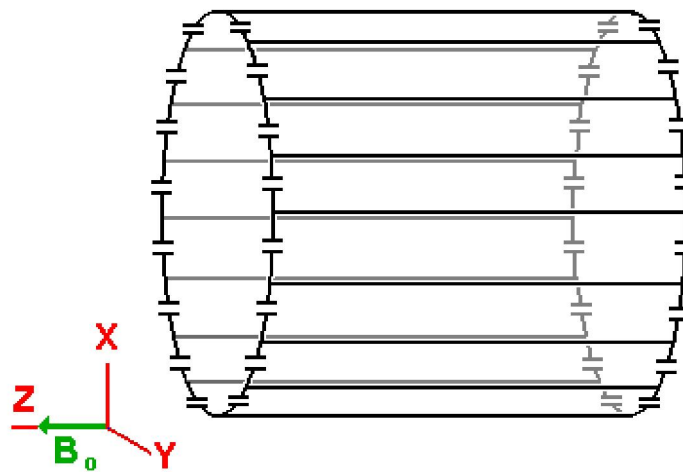


Figure 2.8 Example of a low pass birdcage coil.

### 2.3.3.1 Magneto Static Field Solutions for Birdcage Coil

Before going into details of birdcage coil, we must review the effect of current distribution on magnetic field pattern. Time independent electric current produces a steady magnetic field and the differential equations regarding this is given in Equation (2.10) and Equation (2.11):

$$\nabla \cdot \mathbf{B} = 0 \quad (2.10)$$

$$\nabla \times \mathbf{B} = \mu_0 \mathbf{J} \quad (2.11)$$

where,  $J$  is the electrical current density (A/m) and  $\mu_0$  is the magnetic permeability of free space ( $4 \times 10^{-7} \text{ H}\cdot\text{m}^{-1}$ ). By applying the vector identity in Equation (2.12) to the Equation (2.11) we can derive the Equation (2.13) also called continuity equation.

$$\nabla \cdot (\nabla \times \mathbf{A}) = 0 \quad (2.12)$$

$$\nabla \cdot \mathbf{J} = 0 \quad (2.13)$$

To solve the Equation (2.10), called Gauss' magnetic law, we introduce a fictitious field quantity called magnetic vector potential  $\mathbf{A}$  as given in Equation (2.14):

$$\mathbf{B} = \nabla \times \mathbf{A} \quad (2.14)$$

When we substitute Equation (2.14) into Equation (2.11), we can get Equation (2.15):

$$\nabla \times \nabla \times \mathbf{A} = \mu_0 \mathbf{J} \quad (2.15)$$

This can be simplified to Equation (2.16):

$$\nabla \nabla \cdot \mathbf{A} - \nabla^2 \mathbf{A} = \mu_0 \mathbf{J} \quad (2.16)$$

According to the vector theorems, both divergence and curl of a vector should be defined for a solution with an additive constant. Therefore, we need to define the divergence of the vector magnetic field. To simplify the previous equations, we defined divergence as in Equation (2.17):

$$\nabla \cdot \mathbf{A} = 0 \quad (2.17)$$

Thus the Equation (2.16) can be rewritten as in Equation (2.18):

$$\nabla^2 \mathbf{A} = -\mu_0 \mathbf{J} \quad (2.18)$$

This is the well-known Poisson's vector equation and has the solution in the form of Equation (2.19).

$$\mathbf{A}(\mathbf{r}) = \frac{\mu_0}{4\pi} \iiint_{V'} \frac{\mathbf{J}(\mathbf{r}')}{R} dV' \quad (2.19)$$

where the parameter R is given in Equation (2.20):

$$R = |\mathbf{r} - \mathbf{r}'| \quad (2.20)$$

Substituting Equation (2.19) into Equation (2.14) yields the necessary formula for the magnetic calculations. For a line current with constant amplitude  $I_0$ , the magnetic field is given as in Equation (2.21):

$$\mathbf{B}(\mathbf{r}) = \frac{\mu_0 I_0}{4\pi c} \int \frac{d\mathbf{l}' \times \mathbf{R}}{R^3} \quad (2.21)$$

Equation 2.21 states that calculation of magnetic field from induced current is straightforward given the current. As an example, let us have a look at the Figure 2.9, which gives the magnetic field pattern of a square loop along its central direction with a side length of  $w$  and a current level of 1 A. This trend is also similar to the circular loop with a small intensity enhancement at the center [12].

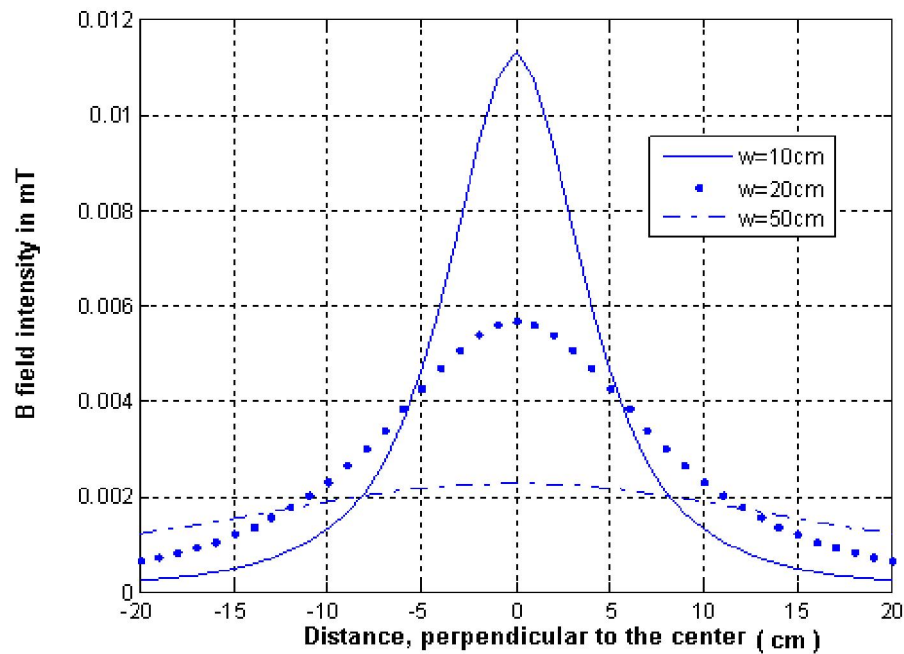


Figure 2.9 B field distributions for different dimensions of square loops.

By using the Biot-Savart's formula, given in Equation 2.18, we can derive the transmission pattern of any coil with a given current distribution. Reception and transmission pattern will be the same due to the reciprocity.

At this point, we have to derive another relation to understand the effect of cylindrical and spherical surface currents on source free regions. Maxwell's equations can be rewritten as in Equations (2.22) and (2.23):

$$\dot{\nabla} \bullet \dot{\mathbf{B}} = 0 \quad (2.22)$$

$$\dot{\nabla} \times \dot{\mathbf{B}} = 0 \quad (2.23)$$

We now define a fictitious field called the scalar magnetic potential with the property given in Equation (2.24):

$$\dot{\mathbf{B}} = -\dot{\nabla}\Psi \quad (2.24)$$

By substituting into Equation (2.22), we obtain Equation (2.25):

$$\dot{\nabla} \bullet \dot{\mathbf{B}} = \dot{\nabla} \bullet (-\dot{\nabla}\Psi) = \nabla^2\Psi = 0 \quad (2.25)$$

This is the popular Laplace equation. Assume there is no variation in z-direction, then we have the closed form solution as in Equation (2.26) in cylindrical coordinates:

$$\Psi(\rho, \phi) = \sum_{m=-\infty}^{\infty} \rho^m (A_m \cos(m\phi) + B_m \sin(m\phi)) \quad (2.26)$$

Here  $A_m$  and  $B_m$  are the constants computed using the boundary and source conditions. By applying (2.24),  $\dot{\mathbf{B}}$  can be rewritten as in Equation (2.27):

$$\begin{aligned} \mathbf{r} \dot{\mathbf{B}}(\rho, \phi) &= -\hat{\rho} \sum_{m=-\infty}^{m=\infty} m \rho^{m-1} (A_m \cos m\phi + B_m \sin m\phi) \\ &+ \hat{\phi} \sum_{m=-\infty}^{m=\infty} m \rho^{m-1} (A_m \sin m\phi + B_m \cos m\phi) \end{aligned} \quad (2.27)$$

As an important example, surface current distribution given in Equation (2.28)

$$\dot{\mathbf{J}}_s = \hat{z} J_0 \sin \phi \quad (2.28)$$

has a  $\hat{B}$  field distribution given in Equation (2.29) [12].

$$\hat{B}(\rho, \phi) = \hat{x} \frac{\mu_0 J_0}{2} \quad (2.29)$$

The field distribution inside a cylinder with a sinusoidal surface current distribution on z direction is a constant. This is the starting point of a birdcage design.

### 2.3.3.2 Equivalent Circuit Analysis of High Pass Birdcage Coil

High pass birdcage coil, given in Figure 2.8, is a circular loop, with longitudinal and circular conducting lines, called legs and rungs, respectively. Rungs also include lumped capacitors to control the current distribution and let the circuit resonate at the predetermined frequency. If capacitors were placed only at the legs, then the coil will be named low pass birdcage coil. If both legs and rungs have lumped capacitors, then the coil will be named hybrid birdcage coil. In either type of the coil, the analysis will be the same in terms of circuit equivalent parameters. Here we will only concentrate on the high pass birdcage coil. The circuit equivalent of the coil is given in Figure 2.10.

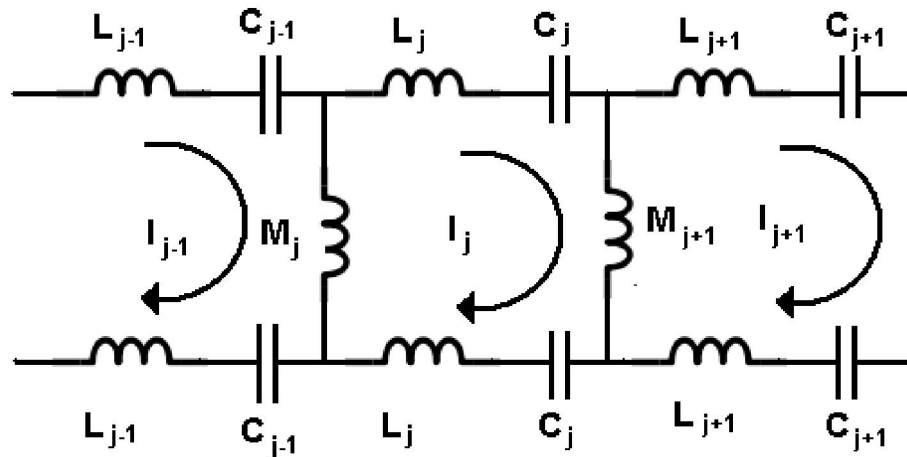


Figure 2.10 Circuit equivalent of high pass birdcage coil.

To simplify the circuit equations, let's choose all the capacitor values (C), inductor values (L), and self inductor terms (M) equal to each other. For the sake

of simplicity, ignore the mutual inductances, which affect the overall resonance solution less than 10%.

By using Kirchhoff's voltage law for the loop consisting of  $j$  and  $j+1^{\text{th}}$  legs and  $j^{\text{th}}$  rungs, we can write Equation (2.30).

$$-i\omega M(I_j - I_{j-1}) - i\omega M(I_j - I_{j+1}) - 2i\omega LI_j + \frac{2i}{\omega C}I_j = 0, \quad j = 1, 2, \dots, N \quad (2.30)$$

Here  $I_j$  is the mesh current for the  $j^{\text{th}}$  loop. Further simplifications lead to Equation (2.31).

$$M(I_{j+1} + I_{j-1}) + 2\left(\frac{1}{\omega^2 C} - L - M\right)I_j = 0, \quad j = 1, 2, \dots, N \quad (2.31)$$

Since the birdcage coils are cylindrically symmetric with  $N$  legs, the solutions of  $I_j$  must satisfy Equation (2.32)

$$I_{j+N} = I_j \quad (2.32)$$

which leads to  $N$  linearly independent solutions, modes, as in Equation (2.33).

$$(I_j)_m = \begin{cases} \cos \frac{2\pi n j}{N} & m = 0, 1, 2, \dots, \frac{N}{2} \\ \sin \frac{2\pi n j}{N} \mathbf{M} & m = 1, 2, 3, \dots, \frac{N}{2} - 1 \end{cases} \quad (2.33)$$

$(I_j)_m$  denotes the current of  $I_j$  in the  $m^{\text{th}}$  solution. To find the total current on the  $j^{\text{th}}$  leg, we need to subtract  $I_{j-1}$  from  $I_j$  thus results in Equation (2.31).

$$(I_j)_m - (I_{j-1})_m = \begin{cases} -2 \sin \frac{\pi n}{N} \sin \frac{2\pi n(j - \frac{1}{2})}{N} & m = 0, 1, \dots, \frac{N}{2} \\ 2 \sin \frac{\pi n}{N} \cos \frac{2\pi n(j - \frac{1}{2})}{N} & m = 1, 2, \dots, \frac{N}{2} - 1 \end{cases} \quad (2.34)$$

It is clear that the solution for  $m=1$  is very similar to  $\sin(\ )$  or  $\cos(\ )$ , which produces a very uniform transverse magnetic field distribution inside the coil.

From the principles of MRI and derived equations, we concluded that the current distribution and amplitude determines the magnetic field pattern of a coil. Uniformity of RF field pattern and high field intensity are required for better imaging. All of the previous equations were dependent on current, which should be optimized to have better patterns. Since we are using LC type circuits to control current distribution on an RF coil, it is crucial to maximize current amplitude at the same time. Maximization of current amplitude simply depends on minimization of impedance of the circuit. From basic circuit theory, we know that the total impedance of an LC circuit at the resonance frequency is zero. This opens a new perspective to us to design new resonant structures with a desired current distribution. After a brief description of ring resonators in the following chapter, we will investigate the characteristics of a new design in the upcoming chapters.

# Chapter 3

## RESONATORS

### 3.1 LC Resonators

In RLC circuits, the frequency where the inductive and capacitive characteristics neutralize each other called the resonance. At the resonance, large oscillations occur. To further study RLC circuits, let's have a look at the following circuit and analysis.

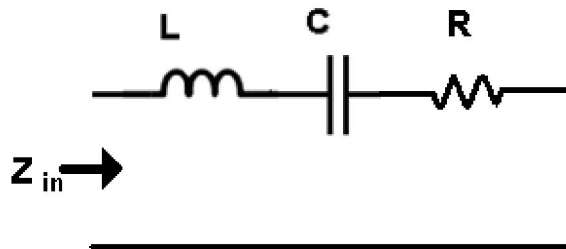


Figure 3.1 Series RLC circuit.

$Z_{in}$  is the input impedance seen by the left port of the circuit and formulated by Equation (3.1).

$$Z_{in} = R + j\omega L + \frac{1}{j\omega C} \quad (3.1)$$

Here  $\omega$  is the angular frequency, R is the resistance, L is the inductance and C is the capacitance of the system, respectively. One can easily conclude that the resonance frequency can be written as in Equation (3.2).

$$\omega_r = \frac{1}{\sqrt{LC}} \quad (3.2)$$

The input impedance of the circuit at the resonance frequency is computed by substituting Equation (3.2) into Equation (3.1) as in Equation (3.3)

$$Z_{in} = R \quad (3.3)$$

The quality factor of a circuit, is the ratio of stored energy to the dissipated energy per cycle, is given by Equation (3.4).

$$Q = 2\pi f \frac{\text{Energy stored in one cycle}}{\text{Energy dissipated in one cycle}} = \frac{\omega L}{R} = \frac{1}{R} \sqrt{\frac{L}{C}} \quad (3.4)$$

Since the impedance of a system is the minimum at the resonance frequency, the current running in the system becomes the maximum on resonance, which is the desired case for RF coil design in MRI. Next section will help us to visualize current distribution on a ring resonator for different frequencies and their analytical solutions for field patterns.

## 3.2 Ring Resonator Analysis

### 3.2.1 Electromagnetic Analysis

Ring resonators are an example of transmission lines designed as closed loops in a certain shape such as circular and rectangular (or any other geometrical structure). The most basic one is of course a circular ring resonator, given in Figure 3.2.

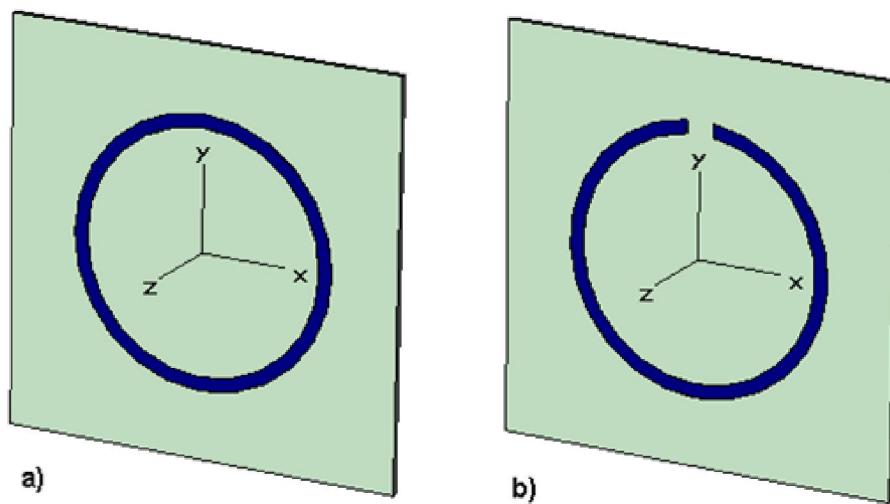


Figure 3.2 Structure of a circular resonator a) a closed ring resonator and b) a split ring resonator.

These resonators can be fabricated on a substrate with a ground plane coated on the backside, and excited by using micro-strip transmission lines from desired points. For double micro-strip feed lines, the wavelength of a guided wave in a micro-strip ring resonator is given by Equation (3.5)

$$\lambda_g = \frac{2\pi r}{n} \quad (3.5)$$

Where  $r$  is the diameter of the ring and  $n$  is an integer, which represents the mode number. For a single feed line, this is given by Equation (3.6).

$$\lambda_g = \frac{4\pi r}{n} \quad (3.6)$$

So, a single feed line structure supports longer wavelengths, (or equivalently smaller frequencies). Details of feeding and coupled line analysis can also be found at Ref.13.

Solving Maxwell's equations in circular coordinates for this resonator system with TM excitation ( $\partial/\partial z = 0$ ) yields Equations (3.7-3.9).

$$E_z = \{A J_n(kr) + B N_n(kr)\} \cos(n\phi) \quad (3.7)$$

$$H_r = \frac{k}{j\omega\mu_0 r} \{A J_n(kr) + B N_n(kr)\} \sin(n\phi) \quad (3.8)$$

$$H_\phi = \frac{k}{j\omega\mu_0} \{A J'_n(kr) + B N'_n(kr)\} \cos(n\phi) \quad (3.9)$$

with the boundary condition of

$$H_\phi = 0 \quad \text{at } r=r_i \text{ and } r_0 \quad (3.10)$$

where  $A$  and  $B$  are constants and  $k$  is the wave number,  $\omega$  is the angular frequency,  $J_n$  is the Bessel function of the first kind with an order of  $n$  and  $N_n$  is the second kind Bessel function with an order of  $n$ .  $J'_n$  and  $N'_n$  are the derivatives of their original functions. Applying boundary conditions leads to an eigenvalue equation, which includes the solutions of resonance frequencies [13].

As seen in this example, analytical solutions to the modes of a resonator, even in a single and fixed excitation point, are laborious and make the design of practical applications cumbersome. Instead, we can check the field distribution of ring resonators for different modes calculated by the help of computational tools. For example for a double port-excited system, the field maximums are depicted as in Figure 3.3 for the first two modes [13]:

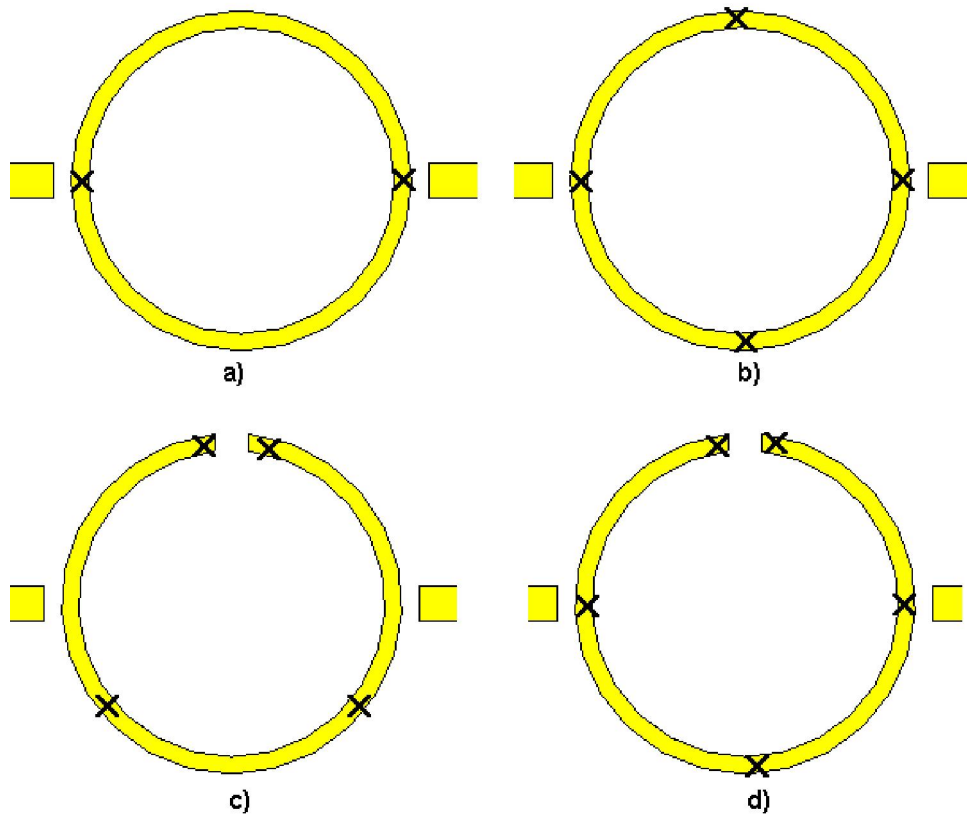


**Figure 3.3** Field maxima of ring resonators for their first two modes: a) for  $n=1$ , b) for  $n=2$ , c) for  $n=1.5$ , and d) for  $n=2$ .

As seen from the Figure 3.3, modes with integer multiples have field maximum near the port coupling gaps. This was expected and theoretically shown in literature [13].

Since split ring resonators (SRR) offer more flexible resonant characteristics than closed ring resonators, we will concentrate on the field and current distribution of SRRs from now on. To find the resonance frequency of a SRR,

we performed EM simulations by using a finite integral method (FIM) solver of CST Microwave Studio®. For these simulations, a circular ring was placed on a 380  $\mu\text{m}$  thick silicon wafer that has the dimensions of 30 mm by 30 mm and the ring was set to have a diameter of 20 mm with 1 mm wide gold lines and has the thickness of 20  $\mu\text{m}$ . the gap size set to 1 mm to keep aspect ratio reasonable. The structure of this SRR is shown in Figure 3.4(a).

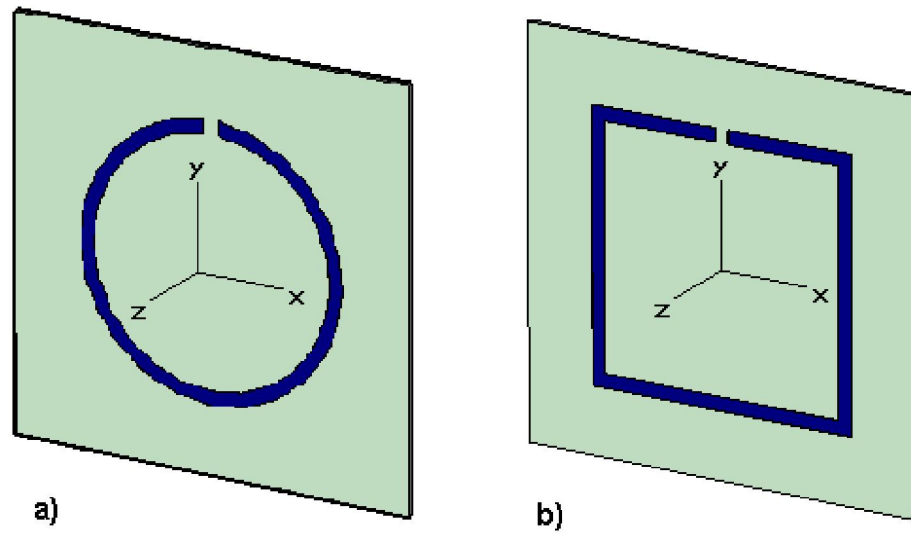


**Figure 3.4 Footprint of a) circular b) rectangular SRRs.**

The normalized transmission of the structure is given in Figure 3.5.

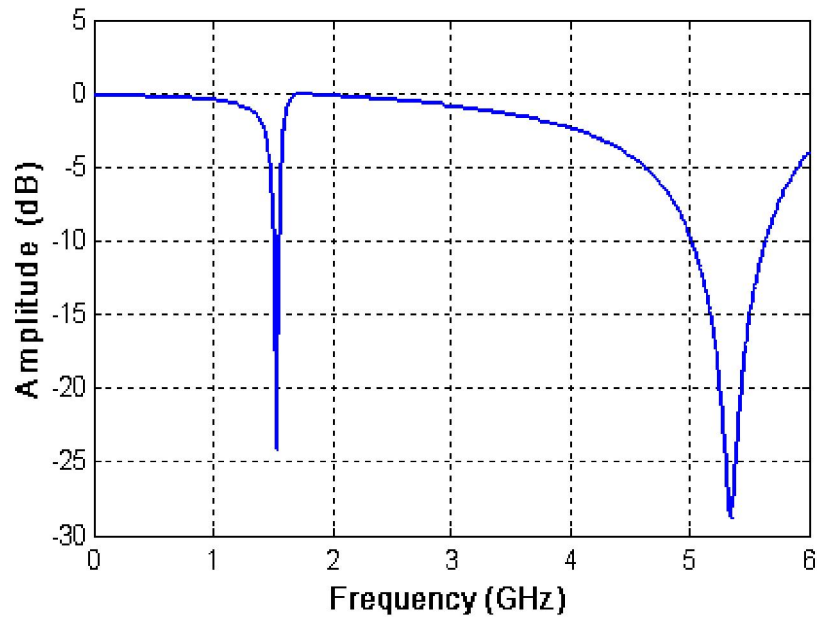


**Figure 3.5** Transmission of a circular SRR.

The first two modes can be seen in Figure 3.5. Since we will be interested in lower order modes, we investigate the current distribution of the structure for several frequencies lower than the first mode as in Figure 3.6.

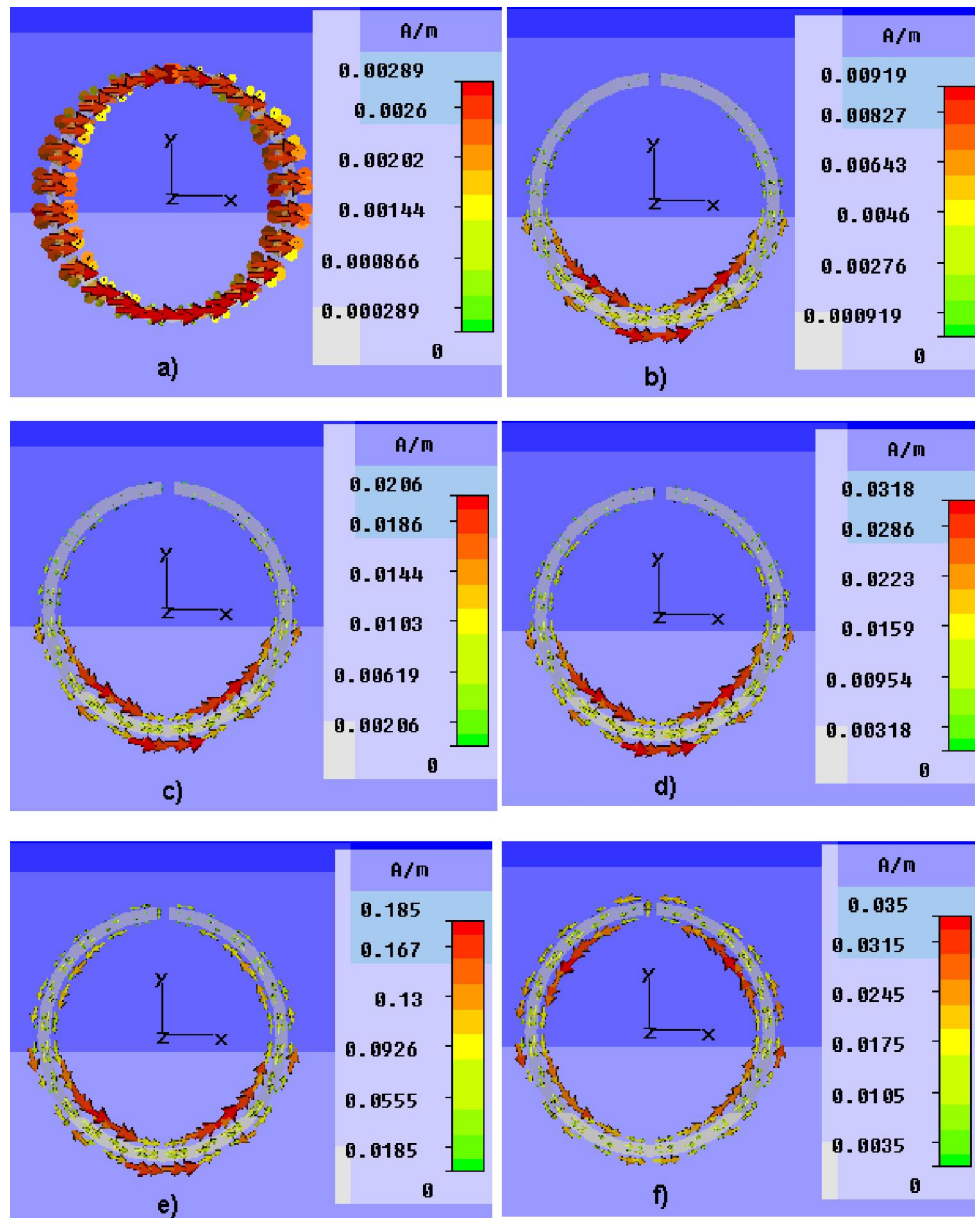
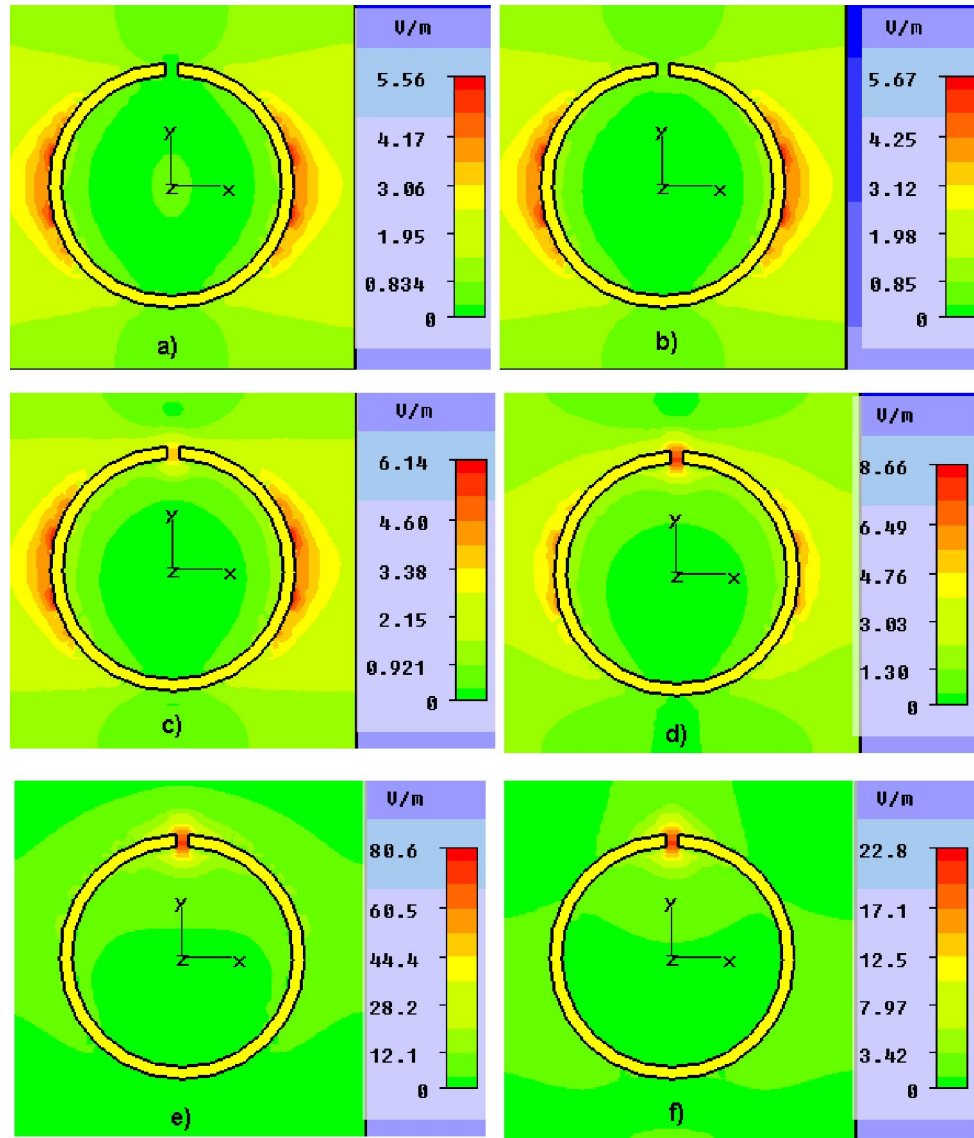


Figure 3.6 Current distribution of the circular SRR at different frequencies: a) at 100 MHz, b) at 500 MHz, c) at 900 MHz, d) at 1.1 GHz, e) at 1.5 GHz (on resonance), and f) 2.0 GHz.

It is evident that the current amplitude is at the peak level when the frequency is at the resonance value of 1.5 GHz. Only the current amplitude is not enough to justify our claims that the resonance is the best case for a coil to improve its MRI performance. We should check the E-field distribution of the resonator.

This will give idea us an idea about where the electromagnetic field is confined and at what frequency is the volume of the field amplification is maximized. Let us have a look at the E field patterns at different frequencies in Figure 3.7.



**Figure 3.7** Electric field distributions of the circular SRR at different frequencies: a) at 100 MHz, b) at 500 MHz, c) at 900 MHz, d) at 1.1 GHz, e) at 1.5 GHz, f) at 2.0 GHz,

It is clear that the E-field intensity is higher for 1.5 GHz and the field is confined at the resonator gap location, which can be controlled, and specific absorption

ratio (SAR) of the body can be minimized by isolating this part from the living tissue.

After this brief analysis of a circular ring resonator, it is time to understand the relationship between its resonance frequency and physical dimensions. The most effective parameter, as can be seen from the previous discussion, is the gap size. The capacitive region confines the E-field and thus controls the resonance frequency. Next section discusses this issue in detail.

### 3.2.2 Resonance Frequency Analysis

For a plane wave excitation, which means no coupling to the source or any other measurement equipment, SRRs have the equivalent circuit given in Figure 3.1. For an SRR, inductance is due to its conducting lines and geometry, whereas capacitance is due to its gap and self-capacitance of the metallic lines. To analyze the effect of gap capacitance on the resonance frequency, we performed the electromagnetic simulations. Transmission of the SRR structure is analyzed for each gap size and their magnitudes (in dB scale) are depicted in Figure 3.8.

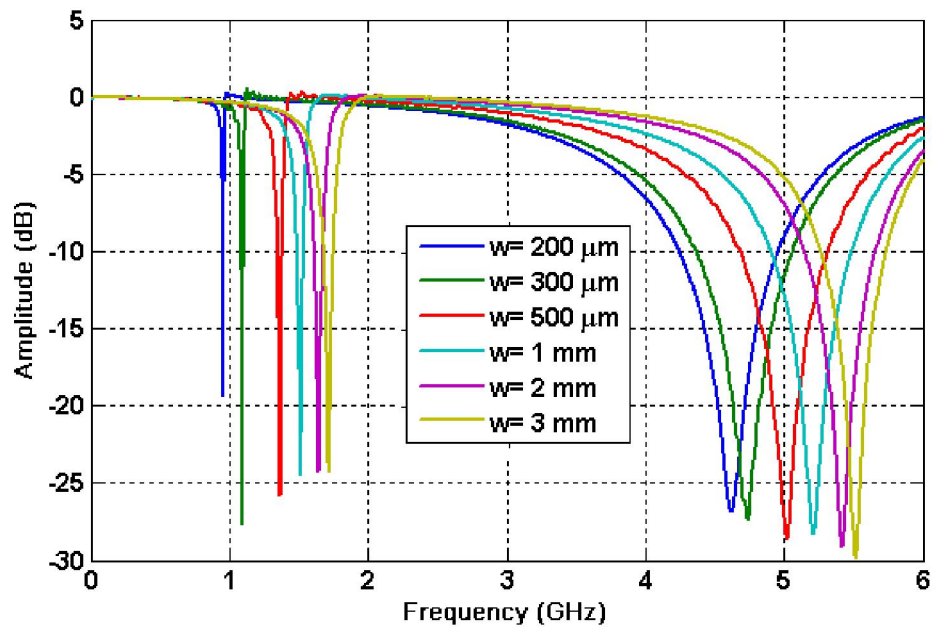
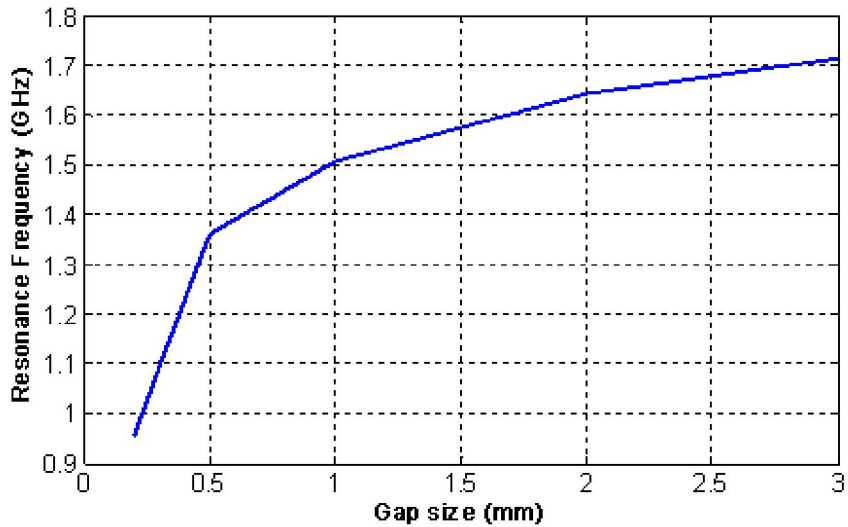


Figure 3.8 First two modes of circular SRR for different gap widths.

As seen from Figure 3.8, decreasing the gap size increases the gap capacitance, to decreases the resonance frequency. To understand the model better, let us analyze the first mode resonance frequency and the corresponding effective capacitance of the gap.



**Figure 3.9 Resonance frequency as a function of the gap size for the circular SRR.**

Figure 3.9 is derived from the Figure 3.8 that shows the relationship between the gap size and the resonance frequency. Inductance, which is only dependent on the size of conducting lines, does not change significantly with such gap size change, and thus, allow us to conclude that the frequency change is due to the variations in the gap capacitance. The inductance of the circular ring is calculated to be 60 nH [14]. Given resonance frequency, we can extract the effective capacitance for each frequency as in Figure 3.10.

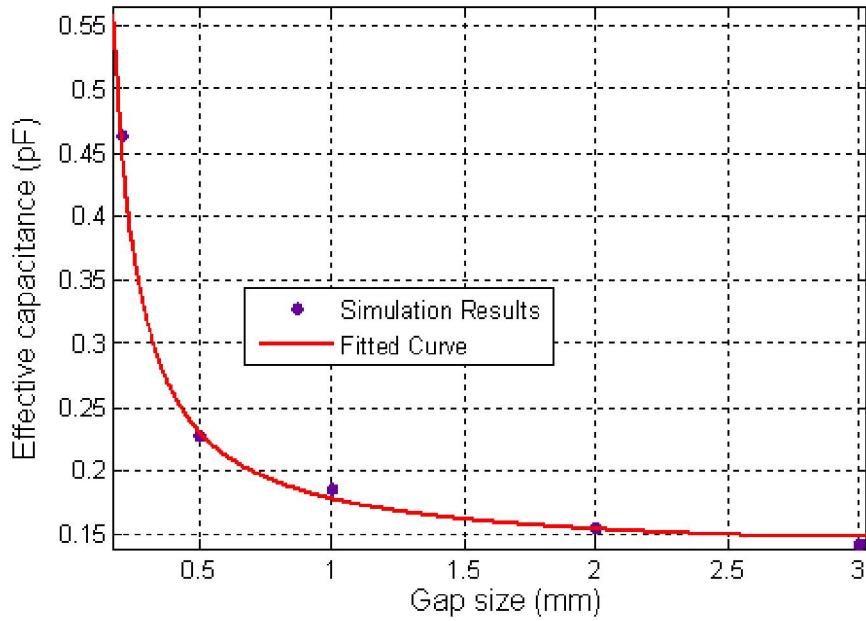


**Figure 3.10 Effective capacitance due to gap size.**

This fitted curve can be represented by the Equation (3.11).

$$C_{effective} = 134.2 + \frac{41160}{g - 75} (fF) \quad (3.11)$$

where,  $g$  is the gap size taken in  $\mu\text{m}$ .

Another point related to (3.11) is the constant 134.2 fF, which states that there exists a fixed effective capacitance due to both the conductor itself and fringing fields of the gap. Also, this numerical fit fails for  $g$  close to 75  $\mu\text{m}$  or smaller. All of these calculations are carried out to obtain a circuit equivalent of circular SRR in the given physical dimensions. It is difficult to generalize a circuit model that includes all of the parameters and estimates the solution for all frequencies correctly. To understand detailed derivations, one can check the [Ref. 23](#) and the references therein.

### 3.3 Rectangular SRR Characteristic

After this brief discussion about circular resonators, it will be better to summarize the properties of rectangular resonator shown in Figure 3.3b, which

is used in our structures. Its analytical solutions are easy compared to the circular case due to its Cartesian structure. The rectangular SRR leads to a higher inductance for the same footprint area that helps us to decrease the resonance frequency of the resonator.

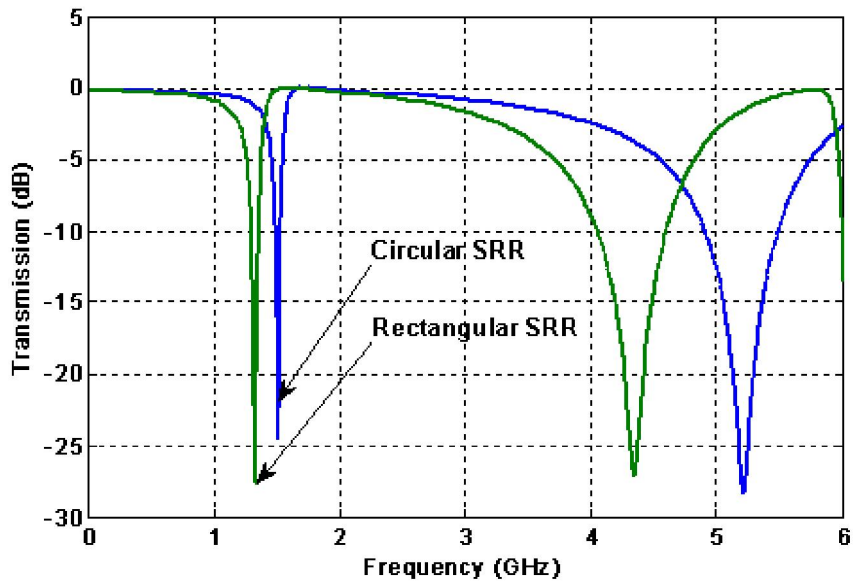


**Figure 3.11** Transmission characteristics of the circular and rectangular SRRs.

To compare their resonance characteristics, we computed the Figure 3.11, which presents the frequency characteristics of the both circular and rectangular resonators with the same footprint area and gap size. Here, their footprint area is 20 mm by 20 mm and their gap size is 1 mm with the line width of 1 mm and metallization thickness of 20  $\mu\text{m}$ , placed on a 380  $\mu\text{m}$  thick, silicon substrate.

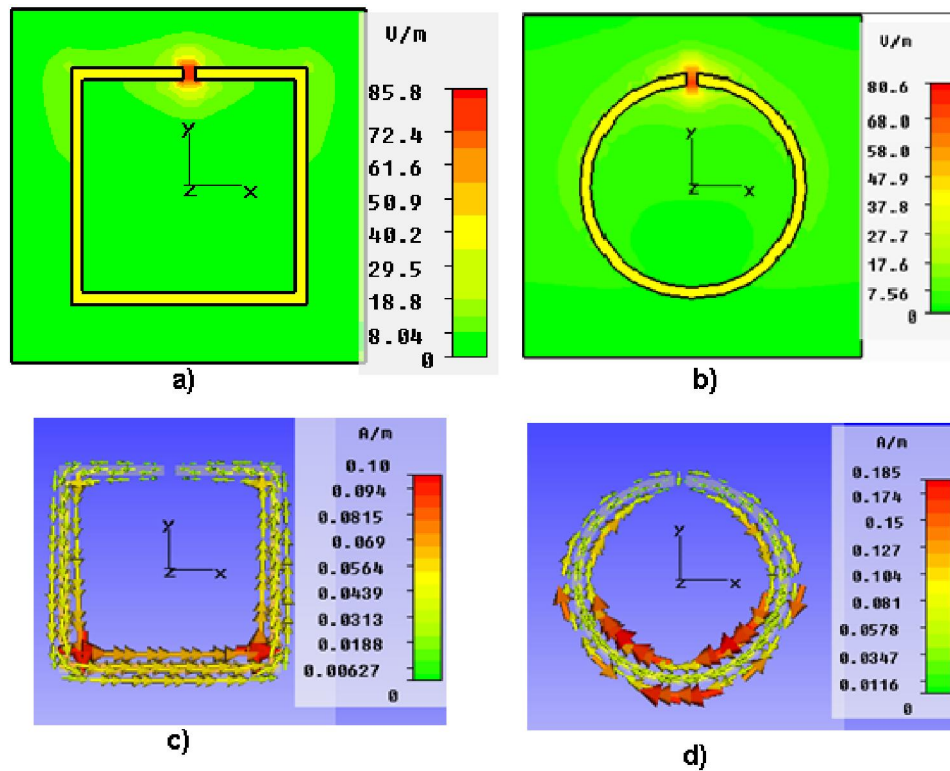


**Figure 3.12 Complete field comparisons of the circular and rectangular resonators on resonance: E field of a) the rectangular SRR and b) the circular SRR, and H field of c) the rectangular SRR and d) the circular SRR.**

Figure 3.12 compares the properties of both resonators. It is clear that the E-field confinement of the rectangular resonator is better than the circular resonator, on the other hand, the circular resonator is better than the rectangular resonator in terms of its higher current level on resonance. Since both resonators were illuminated by the same TEM plane wave source, polarized in  $x$ -direction, due to its greater area, the rectangular SRR can capture more electromagnetic power that results in a stronger E-field confinement. It also consists of linear metallic lines that span more spatial points to amplify the electric field, whereas the circular geometry cannot support outer points strongly. The circular SRRs can amplify the fields at their centers better than the rectangular SRRs, but their outer patterns are not as promising.

# Chapter 4

## LOADING OF RESONATORS

### 4.1 Lumped Element Loading

Despite their strong resonance characteristics and relative ease of fabrication, SRRs are not used in MRI due to their physical constraints. First, to have an SRR resonating around 130 MHz, one has to scale the previous dimensions by a scaling factor of 10, requiring a footprint area of 20 cm × 20 cm. You can see the transmission characteristics of this scaled version of the rectangular SRR as in Figure 4.1 and its field characteristics in Figure 4.2.

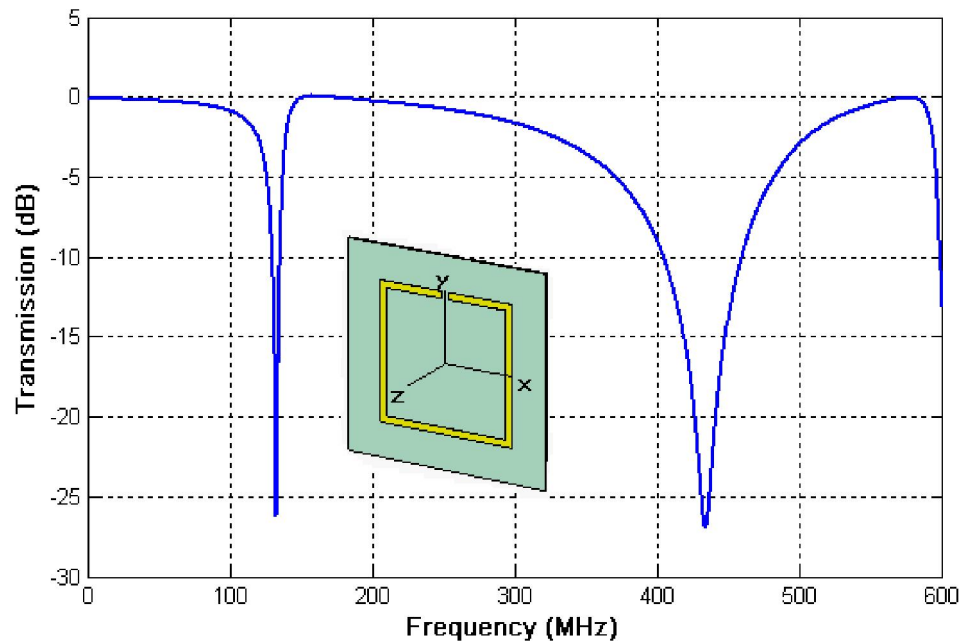
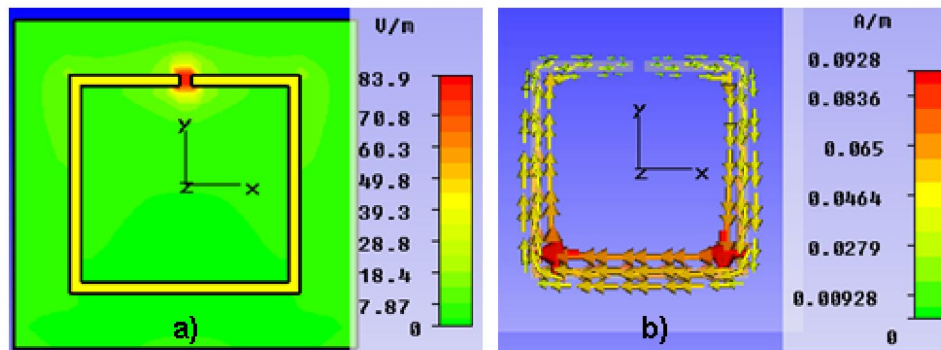


Figure 4.1 Normalized transmission of the rectangular SRR with a footprint of 20 cm by 20 cm.



**Figure 4.2 a) E-field and b) current distribution of the rectangular SRR at resonance frequency.**

This structure has the resonance frequency of 132 MHz with a quality factor of 132. Instead of an SRR, if you use birdcage coil architecture with the given dimensions, you will definitely have a better resonating RF coil with uniform field distribution. SRR's field patterns are not uniform and cannot be homogenized without changing their resonant characteristics.

Decreasing the resonance frequency, while maintaining the size of an SRR in 2 cm  $\times$  2 cm region, is the first challenge that we have to overcome to use an SRR in MRI. Since the inductance of a rectangular SRR is higher than the circular one with similar dimensions, which helps us to decrease the resonance frequency, we will concentrate on the rectangular SRR. Tuning, adjusting the resonance frequency, of SRR should be done to resonate at 123 MHz. Free space wavelength is 2.44 m which is 120 times greater than the dimensions of SRR. Working in such sub-wavelength scale allows us to use the wealth of circuit theory as the starting point. The circuit model of the structure is composed of a lumped inductor, a lumped capacitor, and a resistor, connected in series as in Figure 3.1. To understand the resonance characteristics of SRR due to lumped capacitor located at the gap, we performed circuit theory and electromagnetic simulations simultaneously for the rectangular SRR. They have small disagreements with each other due to the imperfect implementation of the circuit model of the physical structure and the results of electromagnetic simulations are given in Figure 4.3.

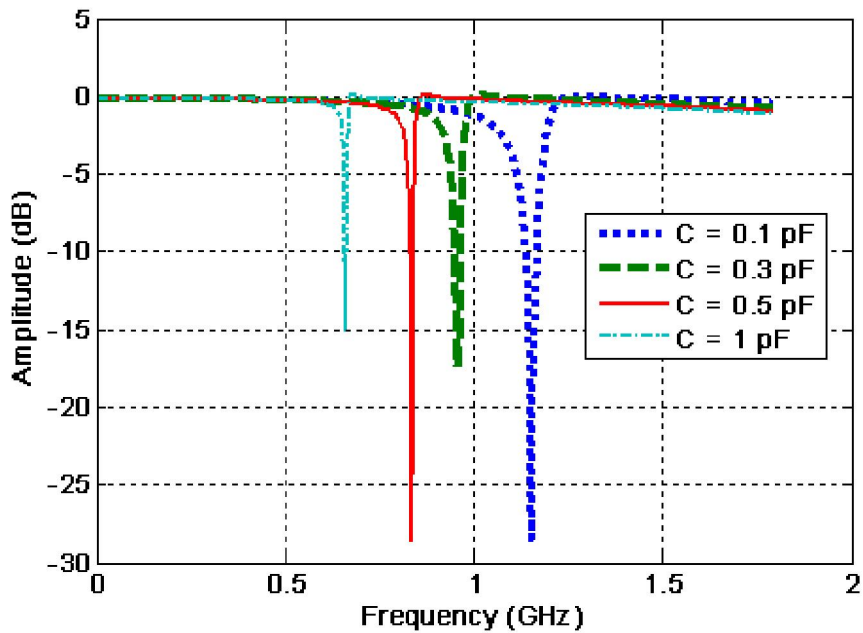


**Figure 4.3** Transmission spectrum of the rectangular SRR for different lumped capacitances.

From a circuit theory perspective, if the capacitance increases with an order of magnitude then the resonance frequency should decrease to  $1/\sqrt{10}$  of its initial value. Since the gap capacitance of the structure is calculated to be around 185 fF as discussed in Chapter 3, which is parallel to the lumped capacitance, we cannot neglect it in these comparisons. We can simply say that, overall capacitance is increased from 285 to 1185 fF, approximately at factor of 4, and resonance frequency is decreased from 1152 to 660 MHz, with factor of  $1/\sqrt{3}$ . We also performed the circuit analysis by neglecting the effect of this gap capacitance and presented the results in Table 4.1. These results state that gap capacitance of the structure is important when we add comparably lower lumped capacitance values to the system. On the contrary, for higher lumped capacitor values, only the effect of lumped capacitor is remained. EM analysis does not diverge from the realistic frequencies anymore, for  $L=60$  nH and  $C=1$  pF, which states that the wireless measurements of the resonance of a structure is the same with its circuit resonance behavior. Since we will be using SRR as a wireless resonator, its EM simulation results are more reliable than its circuit analysis.

Lumped capacitance (pF)	Resonance frequency (MHz)		
	Circuit model with additional 185 fF	Circuit model without additional 185 fF	EM simulation
0.1	942	2055	1152
0.3	722	1186	954
0.5	608	918	834
1.0	462	650	660

**Table 4.1 Comparisons of computed resonance frequencies L is calculated as 60 nH [14].**

## 4.2 Thin Film Loading

By using a proper circuit equivalent of an SRR, it would be possible to analyze it in a convincing way. Once we achieved the desired resonance frequency in such dimensions, it would be possible to go inside the body, invasively or by endoscopic ways, and image the tissue of interest potentially with a higher resolution. Before we increase the value of lumped capacitor in such a medium, we have to analyze its electromagnetic characteristics and, if necessary, modify our structure.

It is well known that human body contains more than 75% of water with several ionic minerals such as Mg, K, Ca, Fe, Na, and I, which make the body conductive. The sodium-potassium pump mechanism in cell membrane also contributes to its electrical conductivity [15]. Solving Maxwell's equations in such a lossy medium is necessary to understand the behavior of a resonator in living tissues. Conductivity of the medium is the main source of the loss mechanism in electromagnetic. Recall Maxwell's equations in time domain as in Equations (4.1) & (4.2)

$$\nabla \times \mathbf{E} = -\mu_0 \frac{\dot{\mathbf{H}}}{\partial t} \quad (4.1)$$

$$\nabla \times \mathbf{H} = \epsilon_0 \frac{\partial \mathbf{E}}{\partial t} + \mathbf{J}_{cond} + \mathbf{J}_{external} \quad (4.2)$$

Here  $\mathbf{J}_{external}$  is the external current source that is zero for source free case and  $\mathbf{J}_{cond}$  is the loss term due to conductivity of the medium, which is given by

$$\mathbf{J}_{cond} = \sigma \mathbf{E} \quad (4.3)$$

Equation (4.3) tells us to the relationship between the E-field and loss mechanism. If the field confinement is high, with the given conductivity, loss will also be higher due to confinement. This expresses the importance of isolation of capacitive regions from lossy media. Isolation material increases the bulk dimensions of resonators and thus, makes it difficult to be used as an implantable device.

To analyze the effect of loss term ( ) on the field pattern of an SRR, we have to understand the current directions as well. For the sake of simplicity, let us assume that the conductivity is constant and does not depend on position. The induced current on the lines of SRR will create a potential difference between adjacent points on the current direction, hence having E-field to direct from one point to adjacent one. For a good conductor, E-field should be perpendicular to the surface, which means there will be E-field paths passing through the lossy media at a cost of current level reduction. The cross-section view of the boundary between a piece of tissue and the resonator with the mentioned current degeneration can be seen in Figure 4.4.

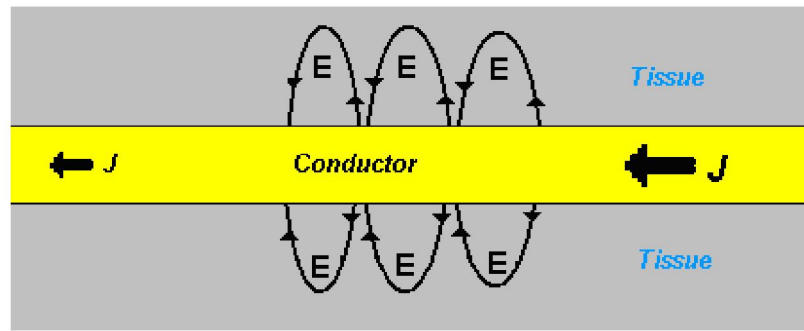


Figure 4.4 Cross-section view of metal-tissue boundary.

In order to induce the same average current level as in the lossless case, we have to couple more power to the resonator, which may be dangerous to the patient. Another drawback is the decrease of quality factor for the resonating structure. Such lossy media cause resistive elements to be dominant in the circuit equivalent. Due to Equation (3.4), quality factor strongly depends on resistance of the system, which is dependent both on the conductor and on medium conductivity parameters. This makes the magnetic field pattern distribution inhomogeneous and difficult to calculate. By coating the surface of metals with proper biocompatible materials, it would be possible to save the tissue from hot spots and most of the problems related to the conductivity of tissue can be overcome. As mentioned before, this will increase the dimensions of the structure for in vivo applications, which is not desired for the implantable devices.

Before starting to the analysis of thin film loading, it is worth mentioning the source of inspiration in this thesis work. In our group, Melik *et al.* proposed inductively coupled strain sensing resonators to telemetrically sense strain and stress on fracture plates during healing process, by which its resonance shift due to its deformation can be monitored in a wireless manner [16]. Our group further decreased the frequency of resonators by keeping their quality factors higher for wireless sensing and investigated the effect of array structures on rigid and flexible substrates [17,18,19]. Our group further improved the resonator and proposed the idea of adding capacitive regions to make a new class of comb-like structures [20]. These novel designs are called nested SRR, which are proven to make a very good candidate to detect strain and stress wirelessly in biological tissues. Our group showed that the nested SRR, with a footprint area of 5 mm by 5 mm, can resonate at around 100 MHz with an acceptable sensitivity and performed the strain measurements 20 cm away from the sensors in soft tissue, which had not been achieved before in this frequency range.

To handle all of the previously mentioned problems of loading, we proposed an idea of loading with distributed capacitance, which we also name distributively

thin film loading. We started our design by adding capacitive regions, which imitate the parallel plate capacitor in their gap region as shown in Figure 4.5.

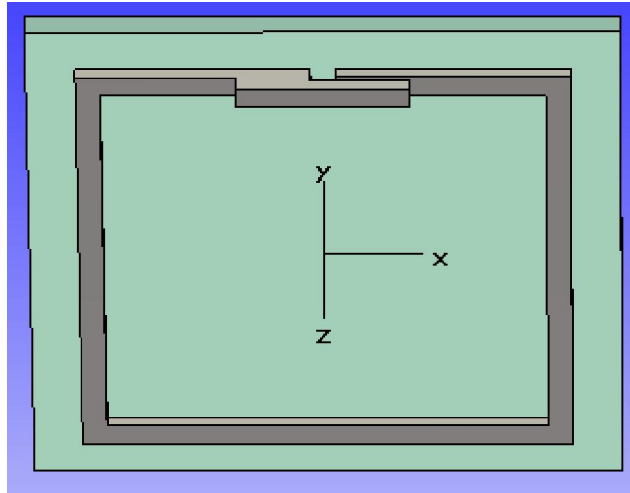


**Figure 4.5 Our rectangular SRR with distributively thin film loading.**

As seen from Figure 4.5, the gap capacitance can be adjusted by various parameters such as line widths, the length of the overlap region, and the thickness of capacitive region. This provides us with an ability to obtain broad range of capacitance values and allows us to control current passing through the conductor by modifying capacitive regions. The side view is depicted in Figure 4.6.

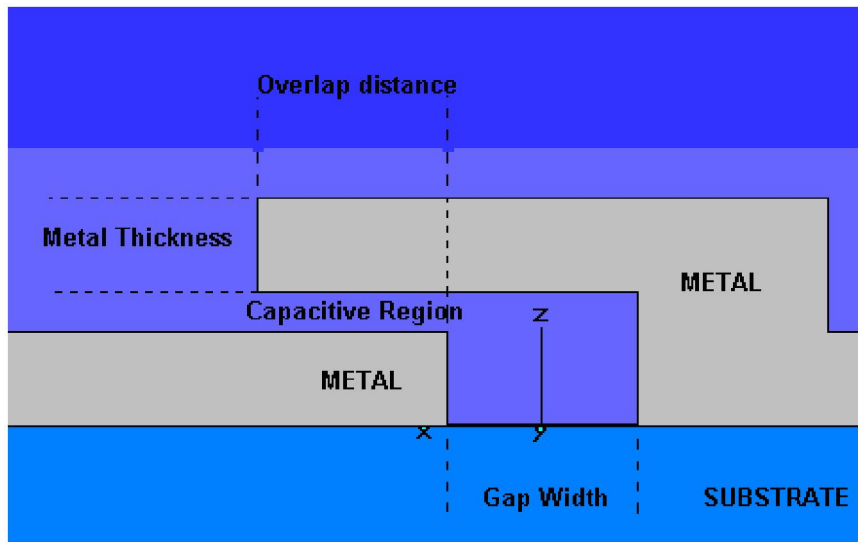


**Figure 4.6 Cross section view of SRR with thin film loaded region.**

Basic circuit theory predicts that a capacitance of 50 pF will be enough to tune the proposed structure to 123 MHz. To achieve this, using a 20- $\mu\text{m}$  thick dielectric film capacitive region with a relative permittivity of four, we need a 56 mm overlap region. These numbers, also slightly more aggressive aspect ratios, are achievable by standard micro-fabrication processes. Since our structure has 20 mm of length for each side, this capacitive region should also be enlarged to other sides. This is the design that we were expecting to reach and characterize. We know that the lumped model parameters, which were given above, will not be in exact agreement with the electromagnetic simulation results. That is why we need to analyze our proposed structure from electromagnetic point of view.

### **4.3 Electromagnetic Analysis of Distributive Loading**

Since there are many geometric parameters to adjust the value of capacitance, we fixed the overlap region take 10 mm long and the metal line width to be 1 mm to start our analysis. The gap width will not matter much after this point due to its relatively smaller capacitance compared to the overlay region. To keep it

in a safe region to distribute E-field (and not to confine it with strong localization in the gap), we kept the gap to be 1 mm. Figure 4.7 shows the transmission frequency characteristics of the proposed design for a 500  $\mu\text{m}$  thick dielectric film.

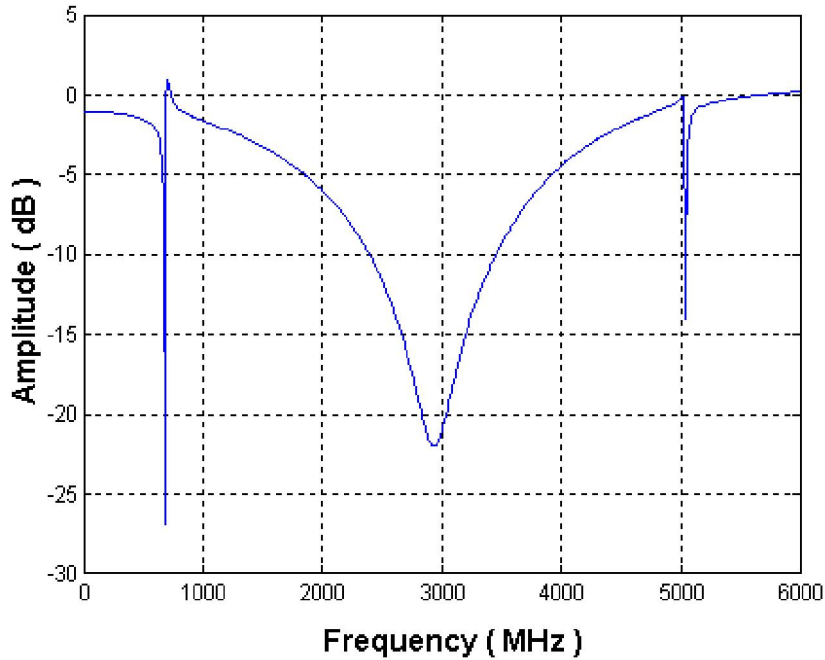


**Figure 4.7 Normalized transmission of SRR for a dielectric film thickness of 500  $\mu\text{m}$ .**

Using parallel plate capacitor formula given in (4.4), capacitance of the overlap section is calculated to be 708.3 fF.

$$C_{overlap} = \epsilon_r \epsilon_0 \frac{A}{d} \quad (4.4)$$

When we look at Figure 4.3, we effectively need approximately 1 pF lumped capacitance to achieve the resonance frequency of 684 MHz by considering all lumped elements. However, we do not need this high level of capacitance anymore because of the additive inductance of the overlap region. We actually have a stacked inductor with an upper winding, which also creates a self-capacitance to decrease the resonance frequency. The contribution of the structure is now clarified that it should be possible to achieve smaller resonances

by decreasing the thickness of the dielectric layer without compromising from the quality of the structure. This proposed structure definitely lowers the tissue losses, which was due to the high E-field confinement inside the tissue and conductivity of the tissue, by instead spreading the E-field on across the distributed capacitive layer. Figures 4.8 and 4.9 show the E-field amplitude and current distribution of the proposed distributively loaded SRR at the resonance frequency.

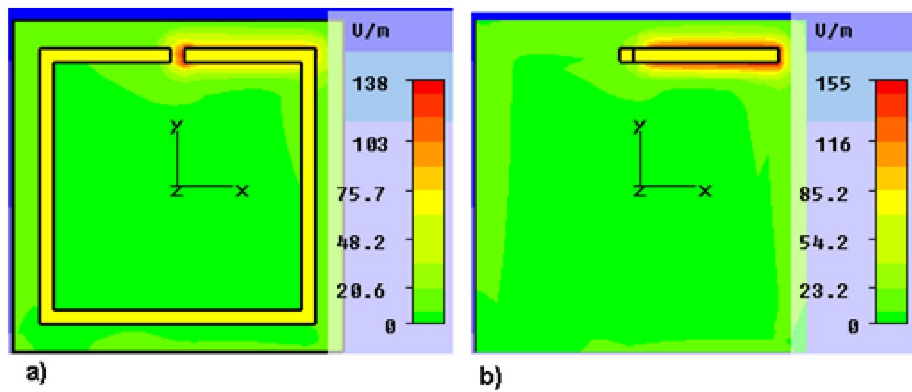


Figure 4.8 Amplitude of E-field distribution: a) on the lower ring and b) on the upper overlay at the resonance frequency.

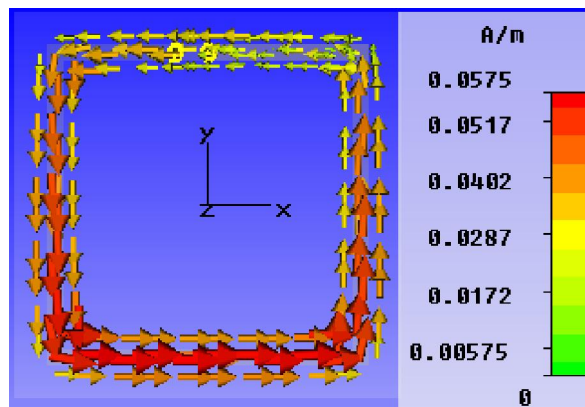


Figure 4.9 Current distribution of SRR at the resonance frequency.

As clearly seen from Figure 4.8, E-field is distributed along the capacitive region through the parallel plate capacitor, which is not contributing to the tissue losses as much anymore, while maintaining a continuous current flow around the ring as shown in Figure 4.9. These figures support the idea of distributed

capacitance phenomenon and its application to lossy medium will be studied in the rest of this thesis.

In order to make sure that this reduction in the resonance frequency is due to the dielectric region, we sweep the dielectric film thickness to analyze its effect. Due to the inverse relationship between the capacitance and dielectric thickness, the resonance frequency is expected to decrease when the dielectric film thickness decreases. Figure 4.10 shows the simulation results of this effect.

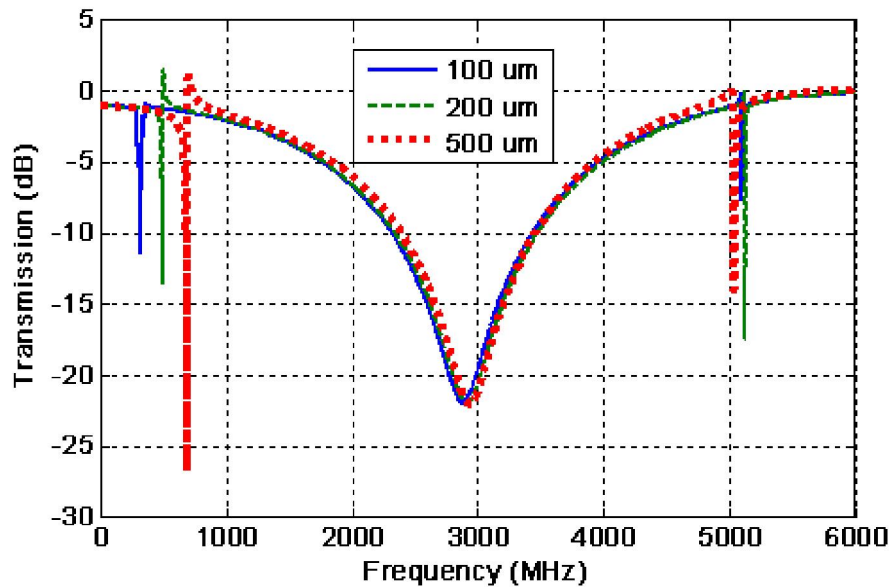


Figure 4.10 Normalized transmission of the partially loaded SRR for various dielectric film thicknesses.

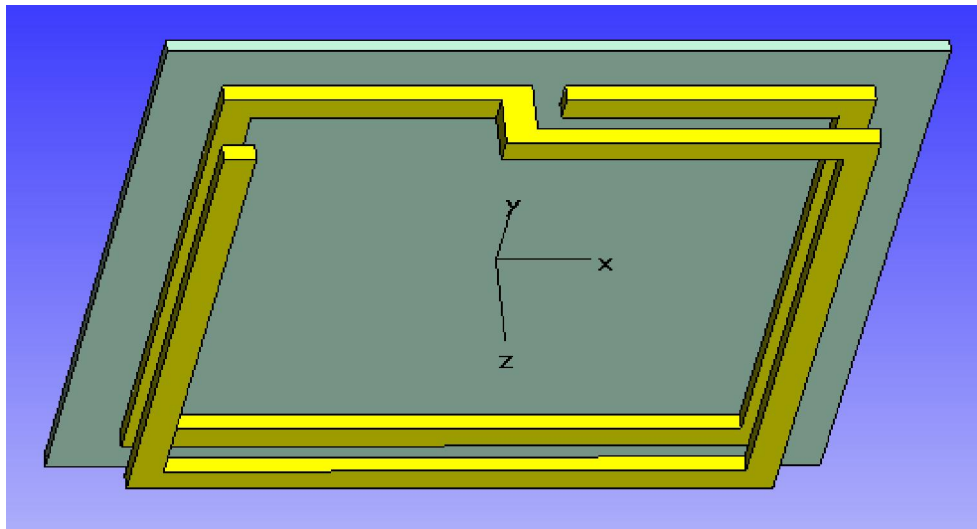
Dielectric thickness ( $\mu\text{m}$ )	100	200	500
Resonance frequency (MHz)	320	456	684

Table 4.2 Resonance frequencies changing due to the different dielectric film thicknesses.

To achieve 123 MHz of resonance frequency, we need to have a dielectric film with a thickness of approximately 15  $\mu\text{m}$ . If we use another dielectric film such as  $\text{Si}_3\text{N}_4$ , and  $\text{Al}_2\text{O}_3$ , film thickness can be 30  $\mu\text{m}$  and 45  $\mu\text{m}$  due to their relative permittivity of 8 and 12, respectively. Again, these dimensions are not difficult

to achieve for micro-fabrication processes. The total thickness of the partially loaded structure is less than  $100\mu\text{m}$  in the final case.

Since the proposed distributive loading of an SRR is a promising technique to decrease the resonance frequency, loading it in a full turn is also examined to see its limits. For full turn loading, with the layout given in Figure 4.11, we also examined the frequency characteristics and its field distributions along its metallic lines. The simulation results were in good agreement with the previous case, which points out that the size of the resonator, can be decreased significantly. This is not an urgent task yet but will be significant in medical applications in our next step.



**Figure 4.11** Layout of a fully distributively loaded resonator (almost one full turn).

Figure 4.12 shows the electric field distributions at the lower ring, upper ring, and the dielectric region between the rings separately and the current distributions at different resonance frequencies (modes) for a  $500\mu\text{m}$  thick dielectric film. Note that the E-field is confined within the region between the plates, instead of outside the plates, which makes this structure to lead to lower levels of loss in a lossy medium than classical SRR. Another point is the current directions for different modes that the first mode current distributions (Figures 4.12 b and d) are better than the second mode (Figure 4.12f). In addition, decreasing the thickness of the dielectric film will make the capacitive regions to

have stronger confinement. Numerically predicted free space quality factors of these resonators are above 100 based on the simulation results using (4.5)

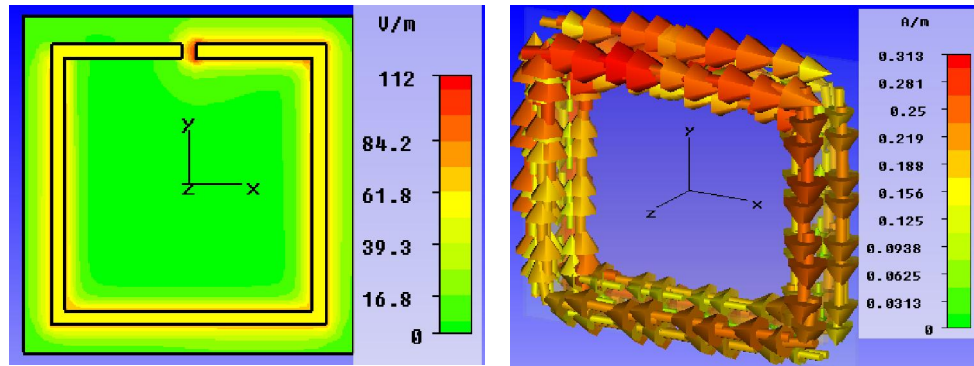
$$Q = \frac{f}{\Delta f} \quad (4.5)$$

where  $f$  is the operating resonance frequency and  $\Delta f$  is the full-width-at-half-maximum amount of  $f$ . Theoretically expected quality factor is around 300 using (4.6).

$$Q = \frac{1}{R} \sqrt{\frac{L}{C}} = \frac{1}{0.1} \sqrt{\frac{60nH}{50pF}} \approx 346 \quad (4.6)$$

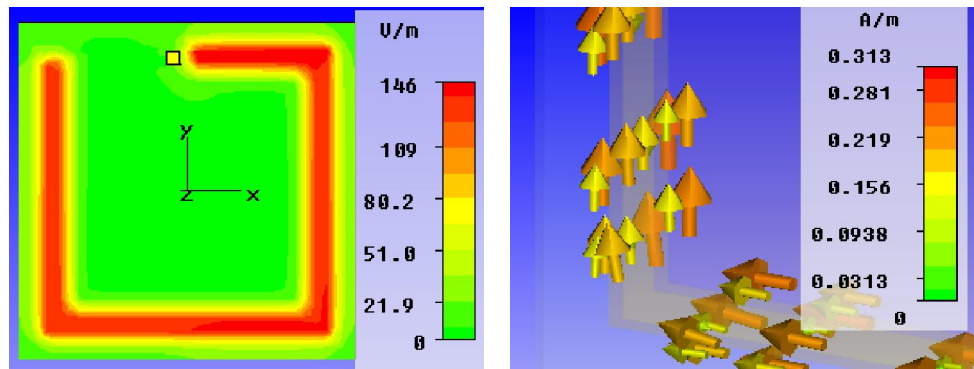
To discuss the quality factor of the structure, we have to be careful about the resonance frequency. For a rectangular SRR geometry as used in this thesis work with a  $2 \text{ cm} \times 2 \text{ cm}$  footprints, has the inductance is 60 nH and the resistance of 0.1 . To tune this structure to 123 MHz it necessary to use a capacitor value approximately 50 pF. When we distributively load the structure, its inductance becomes 240 nH, and resistance increases to 0.2 that does not causes any quality factor enhancement. But the capacitor value to tune this structure to 123 MHz almost decreased to 12.5 pF, which results in quality factor enhancement close to 2.

Without the concern of resonance frequency, quality factor of the resonator does not increase by simply making its metallic lines longer since it results in increased resistive loss. The point is the fixed resonance frequency, which results in decreased capacitance due to increased inductance.



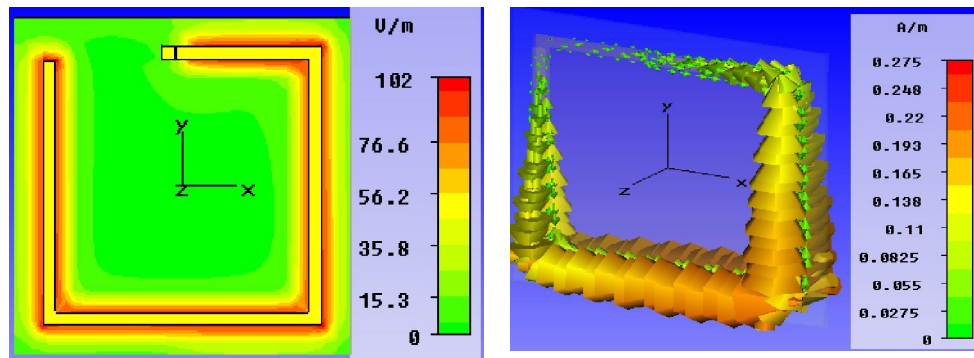
(a)

(b)



(c)

(d)



(e)

(f)

**Figure 4.12 E-field and current distribution for the novel structure for a) E-field amplitudes on the lower ring at resonance frequency, b) current distribution on resonance, c) E-field distribution on the dielectric region, d) a closer look at the current directions on resonance, e) E-field distribution on the upper ring, and f) current distribution of the second mode.**

Figure 4.13 expresses the frequency transmission characteristics of thin film distributively loaded rectangular SRR for various film thicknesses.

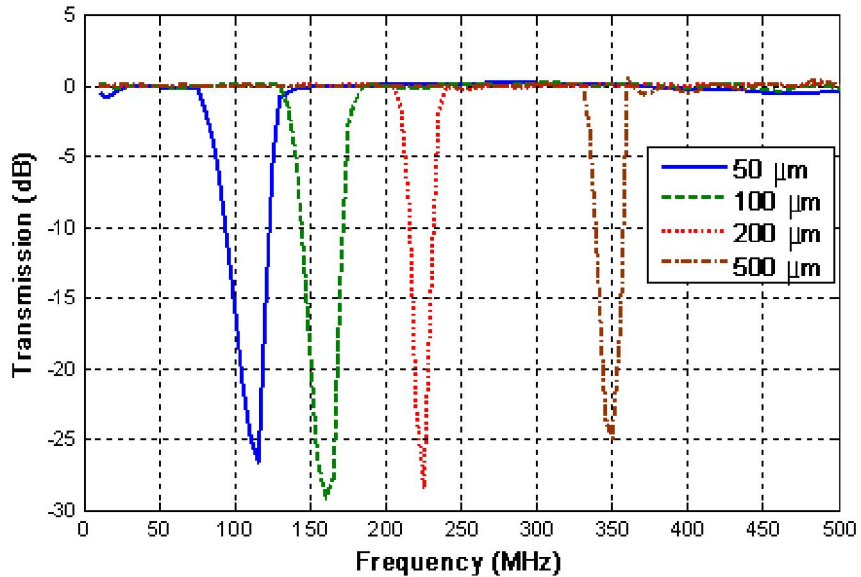


**Figure 4.13** Transmission of fully distributively loaded SRR for various dielectric film thicknesses.

Now we have addressed the challenge of decreasing resonance frequency. To decrease the size further, we need to understand the fabrication challenges and the limitations of micro-fabrication processes. For example, to decrease the side of SRR to 1 cm, L decreases to 24 nH, which corresponds to a 20  $\mu\text{m}$  thickness of the dielectric layer with a relative permittivity of four. This still seems possible to fabricate. The details of fabrication will be discussed in the following chapter.

## 4.4 Circuit Equivalent Analysis of Distributive Loading

The simulation based electromagnetic analysis for the distributively loaded resonator is not easy to perform due to its higher aspect ratio and sub-wavelength dimensions. Free space wavelength at 123 MHz is 2.44 m whereas

the required thin film thickness is around 20  $\mu\text{m}$ , which makes the mesh size less than  $\lambda/122,000$ . Therefore, obtaining accurate numerical solutions becomes difficult and simulations typically last several days for a single structure. Parameter optimization and frequency adjustment can take months with these high aspect ratios. Analytical solutions in phantom regions are not possible due to the Green's function derivation [21]. To make our analysis simpler, we pursued the idea of treading rings as transmission lines with smaller repeating units, called unit cells, and cascade them to predict overall circuit response. It is easy to implement and understand loss terms and the effect of any parameter in the physical model represented by a lumped element. That allows us to analyze our proposed structure quickly using classical circuit simulation tools. This approach is very efficient to estimate the resonance frequency and an example is given in the following section.

#### 4.4.1 Lumped model

As we mentioned earlier, our structure can be represented by combinations of its lumped equivalent circuit elements of inductance, capacitance, and resistance. Initially, let's assume the system is lossless. Therefore there is no resistance term, and we have a pure LC oscillator. Lumped values for the upper and lower rings are the same and, since these two rings are very close to each other, the coupling coefficient,  $k$ , can be accepted to be unity as mentioned in [22]. For a fully loaded structure,  $L_1=L_2=L$  with the mutual coupling given in Equation (4.7)

$$M = k\sqrt{L_1 L_2} \cong L \quad (4.7)$$

Due to the current directions on each loop, this mutual coupling affects both elements positively, and the new inductance value for each inductor is given by (4.8)

$$L + M = 2L \quad (H)$$

These two inductances are connected to each other with a shorted via and coupled to each other with a capacitance  $C_{\text{overlay}}$ . Parallel plate capacitance is

calculated as 50 pF assuming parallel plate capacitance, and  $L$  is calculated as 60 nH as previously mentioned. Instead of  $L$ , we will use  $2L$  for each ring and the overall inductance will be  $4L=240$  nH.

To follow the ascending order in circuit analysis, let's assume we divide this circuit as a single unit cell with upper and lower rings, with a total number of cells  $n=1$ . For unit cell configuration given in Figure 4.14, a lumped capacitance is placed at the middle of the inductances.

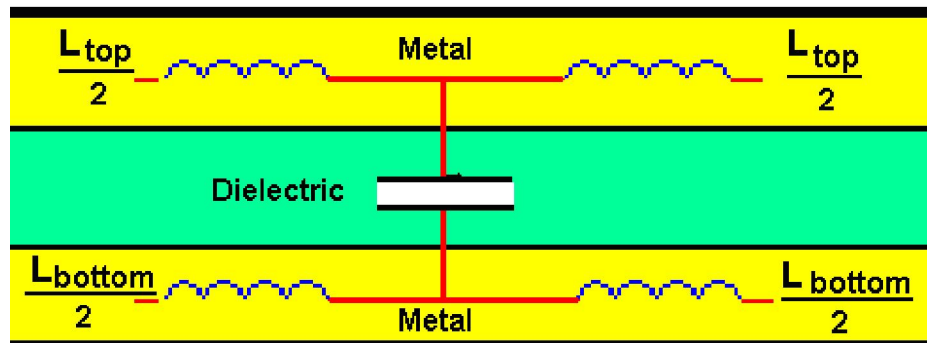


Figure 4.14 Proposed unit cell configuration for distributive loading.

As seen in Figure 4.14, each unit cell has parallel plates with the dielectric region between them, with the given parameters. The numerical circuit equivalent with the connection of bottom to the top layer is depicted in Figure 4.15.

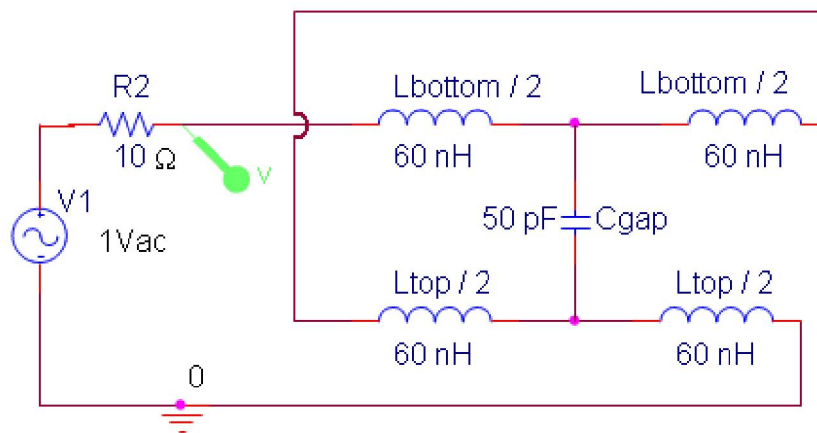


Figure 4.15 Circuit equivalent of structure for  $n=1$ .

10 is an arbitrary value to observe the input impedance of the circuit. It will only affect the amplitude of response dips and their bandwidth, which is used in quality factor calculation. However, this is not a concern yet. The voltage versus frequency is given in Figure 4.16.

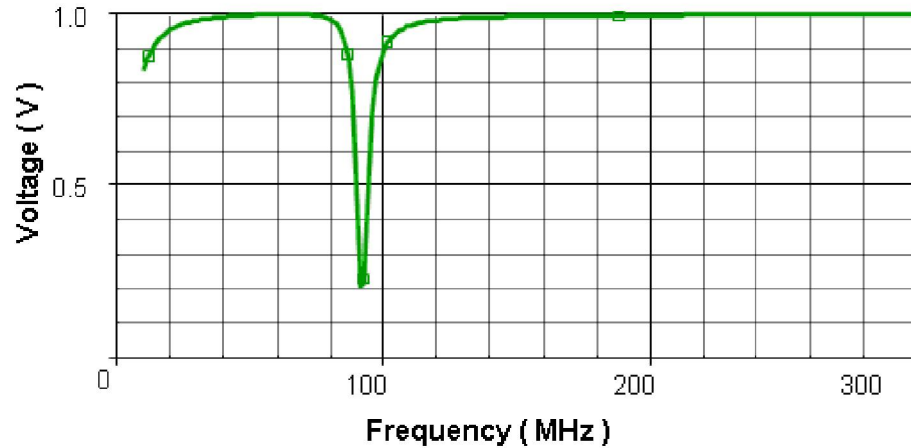


Figure 4.16 Circuit response for  $n=1$ .

As seen from Figure 4.16,  $Z_{in}$ , which is the electrical impedance of the circuit, becomes almost shorted near 92 MHz that results in voltage drop across the terminals. This estimated frequency is too far from the simulation result, which is around 135 MHz. This is due to the lumped model that can not exactly simulate the property of distributed capacitance. In order to be more accurate, we increased  $n=2$  and analyzed the circuit as in Figure 4.17. Each unit cell is now composed of smaller units with smaller inductance and capacitance values.

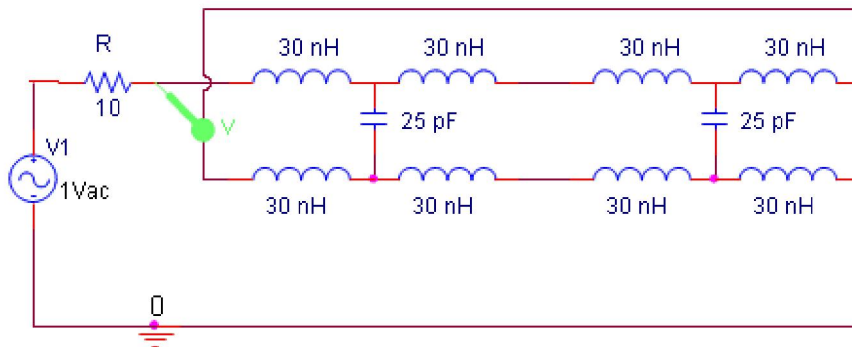


Figure 4.17 Unit cell representation for  $n=2$ .

Here we have two unit cells, each of which has 4 inductances and a capacitance. Via line is seen as if it is a feedback line. Circuit response is given in Figure 4.18.

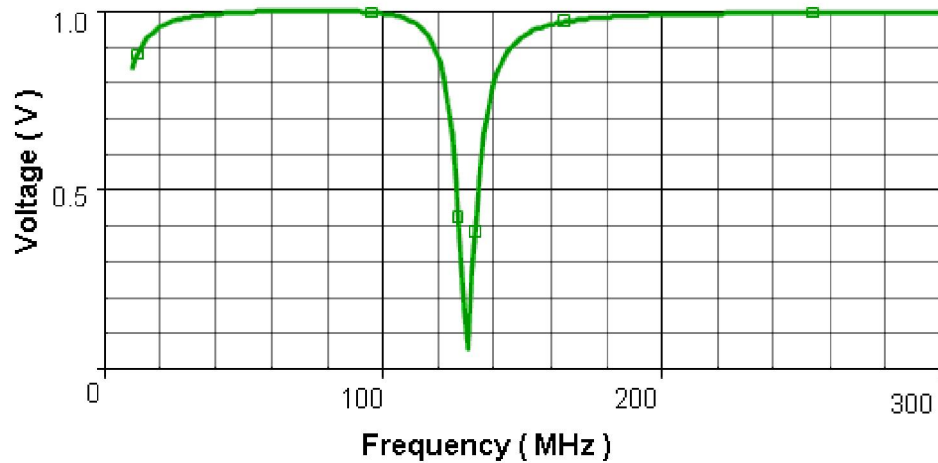


Figure 4.18 Circuit response for  $n=2$ .

The resonance frequency is shifted to 130.4 MHz, which is acceptable without considering the fringe capacitances and approximate values. However, it is surprisingly close, since the exact values of capacitance, inductance can differ from the calculated ones, and fringe effects do not modeled here. To be sure that this not just a coincidence and this method does not diverge, we increased the number of unit cells,  $n$ , and performed the further simulations. Figures from 4.19 to 4.22 show the corresponding simulation results and circuits.

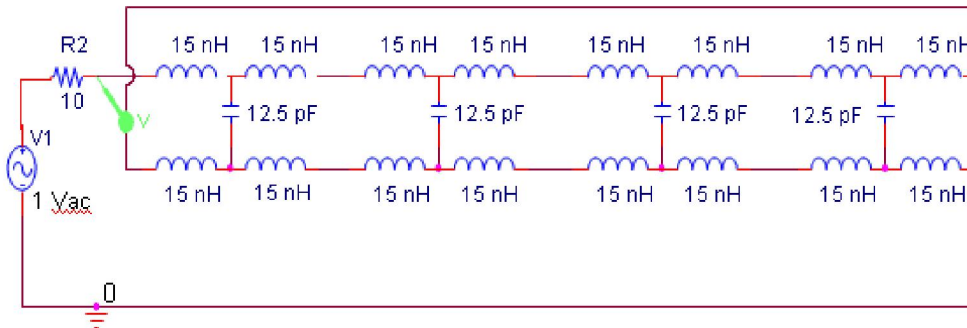


Figure 4.19 Circuit equivalent for  $n=4$ .

We added the series inductances and remodeled the unit cell to simplify the circuit equivalent as given in Figure 4.20.

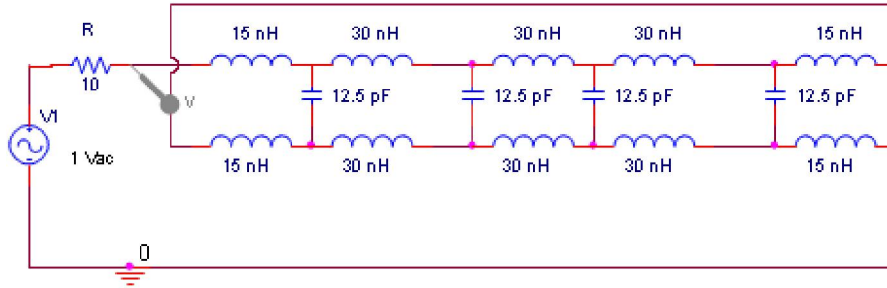


Figure 4.20 Modified circuit equivalent for  $n=4$ .

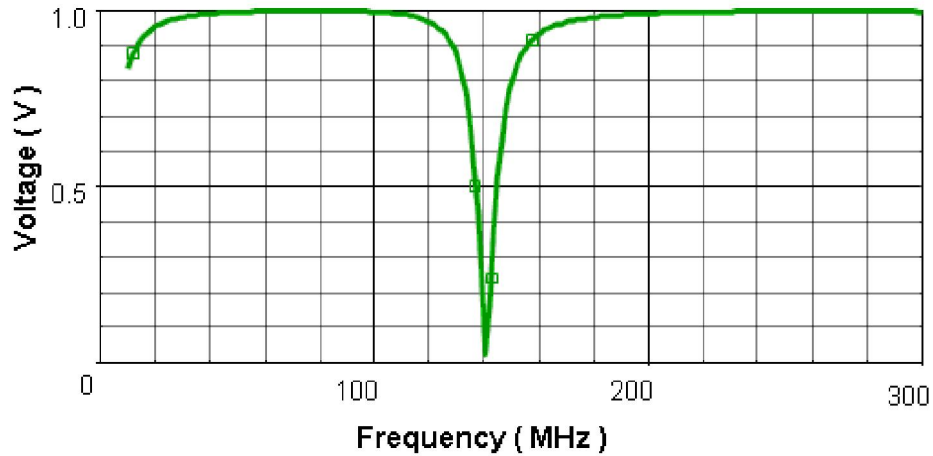


Figure 4.21 Frequency response of the modified circuit for  $n=4$ .

Frequency response of the modified circuit is given in Figure 4.21. this time, the computed resonance frequency is shifted to 140 MHz, which is expected due to more accurate modeling. The convergence study continued until  $n=16$ , which has a very complicated circuit with more than 50 elements. To simplify the circuit representation, inductance values are given as  $L_{16}$  and capacitor values are given as  $C_{16}$  with the corresponding values of 7.5 nH and 3.125 pF, respectively and its circuit equivalent is shown in Figure 4.22.

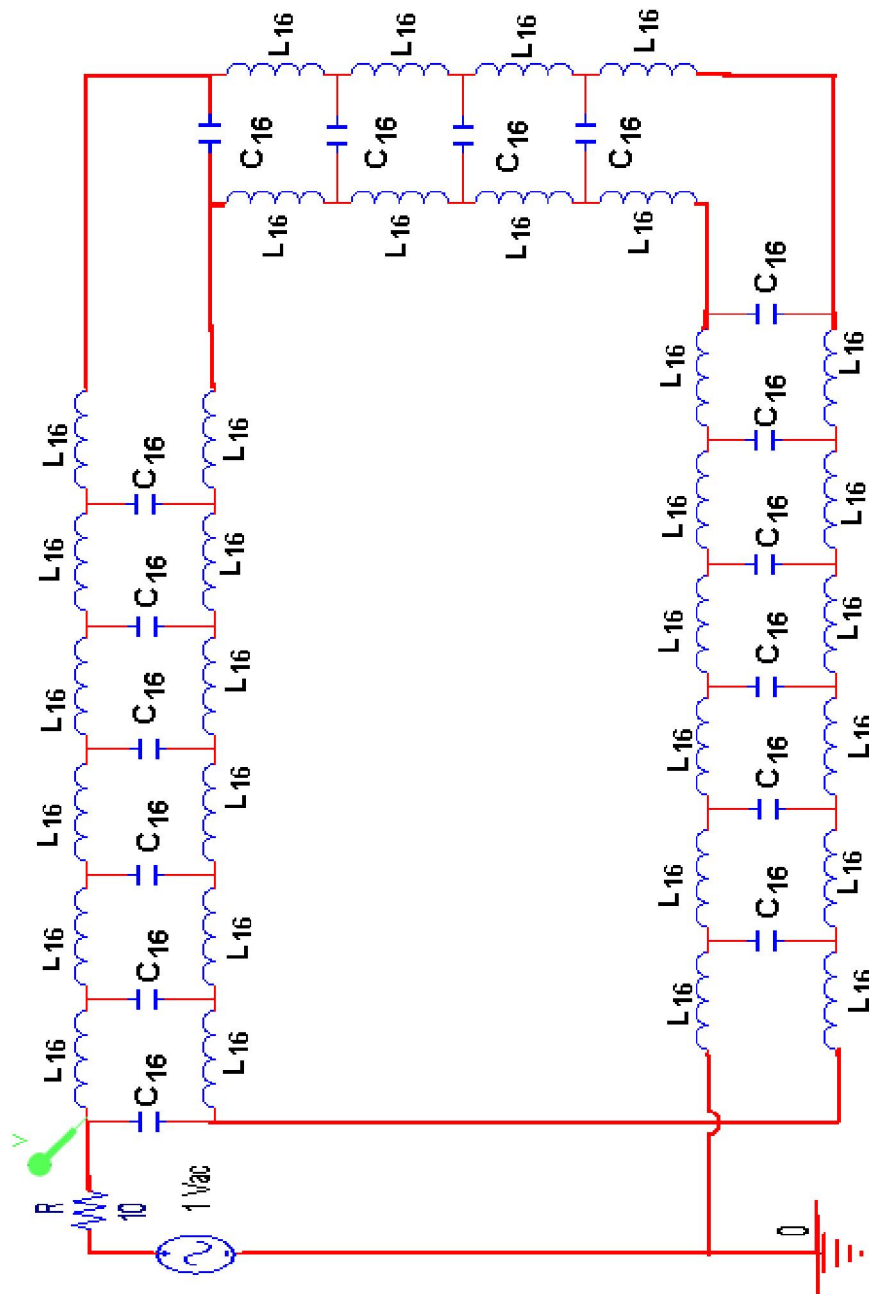
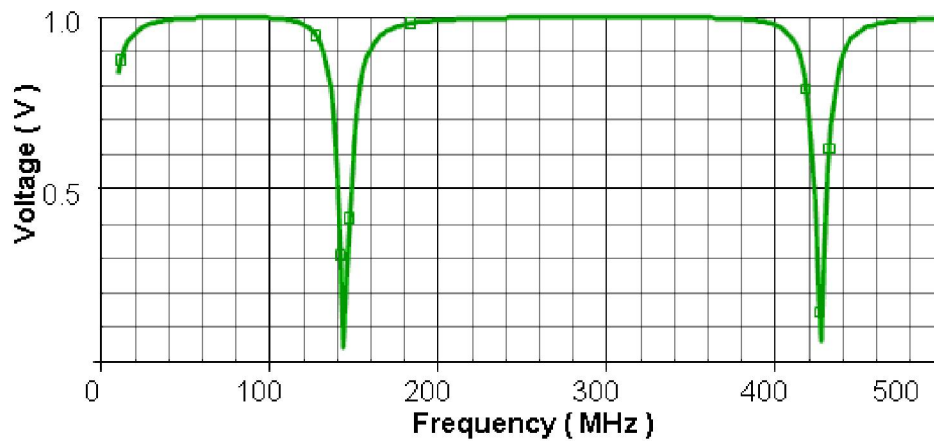


Figure 4.22 Circuit equivalent for  $n=16$ .



**Figure 4.23** Frequency response of the equivalent circuit for  $n=16$ .

Its frequency response is presented in Figure 4.23. The resonance frequency is around 142.1 MHz, which is already in the close margin of  $n$  equals to four and here higher order modes can be observed. Therefore we can even use  $n=4$  case to estimate the resonance frequency of our distributively loaded resonators.

Introducing loss terms is also simple in this unit cell approach. There will be fringe field capacitance,  $C_f$ , in the conductive medium, which is parallel to the gap capacitance with the loss resistance of  $R$ , and the self-capacitance of inductors between the input and output of the unit cell  $C_{self}$ . The principle inductor model includes also a resistance  $R_{ind}$ , connected in series with the inductor. The complete unit cell is now implemented with its loss parameters as shown in Figure 4.24. Previously, it has been proven that the fringe field capacitance does not exceed 10% of the gap capacitance given the associated dimensions [23,24].

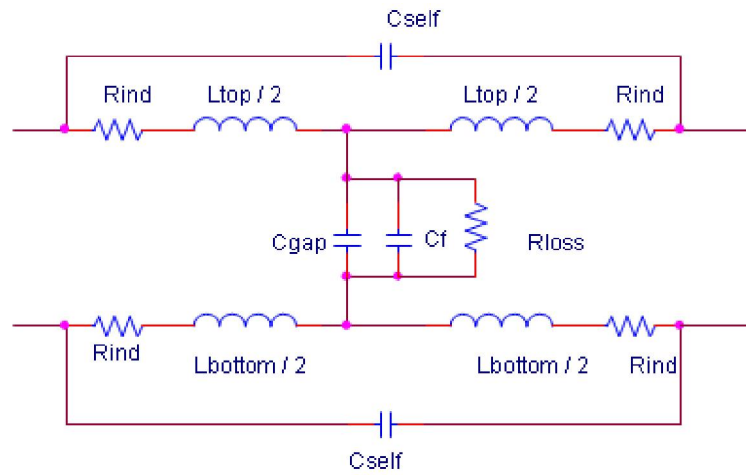


Figure 4.24 Sample unit cell including the loss parameters.

## 4.5 Phantom Simulations for Loss Term Effects

As far as the circuit equivalent models are concerned, loss parameters were not implemented physically in the previous simulations. To model an implantable resonator for in-vivo applications, we need to see the behavior of the resonator in a lossy phantom, called phantom loading of the resonator. Since we will definitely have a biocompatible isolation material to protect the tissue from resonators' conductive lines, we need to add a thin dielectric layer to isolate the resonator from the lossy phantom. To decrease the computational complexity, we will only focus on neighborhood of the field localization regions instead of the complete human body. We chose the size of the phantom to be 20 cm in length in the longitudinal direction. The complete simulation environment is shown in the Figure 4.25

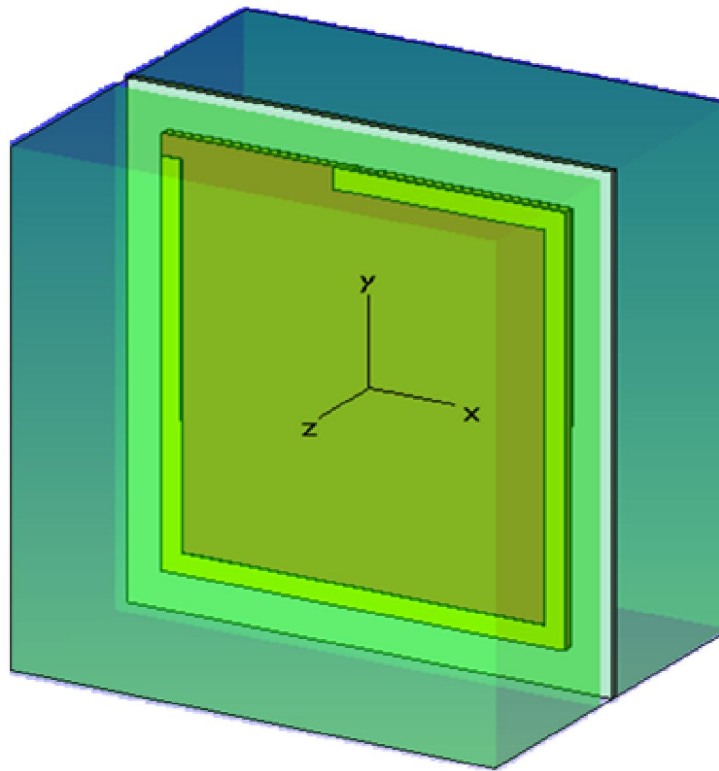


Figure 4.25 Simulation layout for lossy environment.

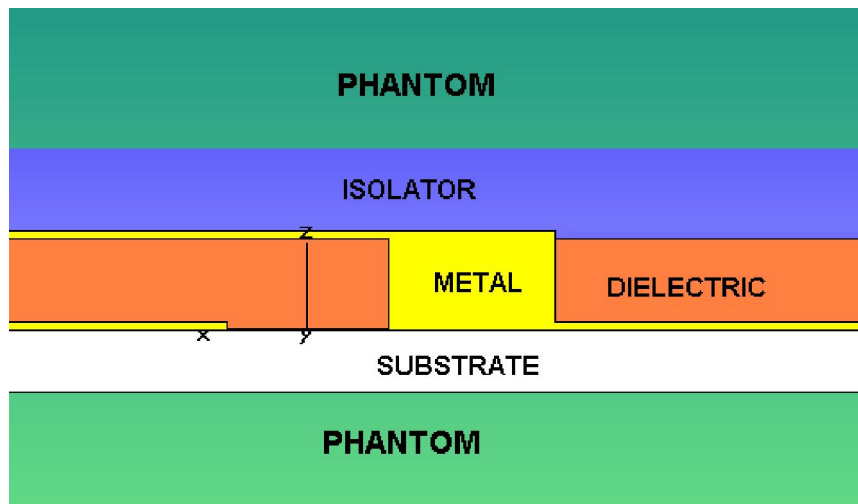


Figure 4.26 Cross section of the simulation environment (not drawn to on scale).

The cross section of the simulation layout is given in Figure 4.26. Isolators are made of biocompatible lossless polymers, which typically have the relative permittivity less than. They will help us to isolate metallic lines electrically from

the environment but should not be too thick not to increase the overall dimensions. For the simulation medium, we took isolator's z-film thickness to be 500  $\mu\text{m}$  to be in a comparable range with the substrate thickness of 380  $\mu\text{m}$  and to cover the whole structure in all other directions. Phantom is set to have a relative permittivity of 75 and conductivity of 1.2 S/m, which are very close to the typical parameters of blood in RF range with the penetration depth of 50 mm. A complete table for the tissues can be found in [25,26 ]. Since the relative permittivity of the phantom is so high, the wavelength of the signal will decrease down to (4.8).

$$\frac{\lambda}{\sqrt{\epsilon_r}} = \frac{244\text{cm}}{\sqrt{80}} \approx 27.3\text{cm} \quad (4.8)$$

The normalized transmission of the resonator inside the phantom is depicted in Figure 4.27.

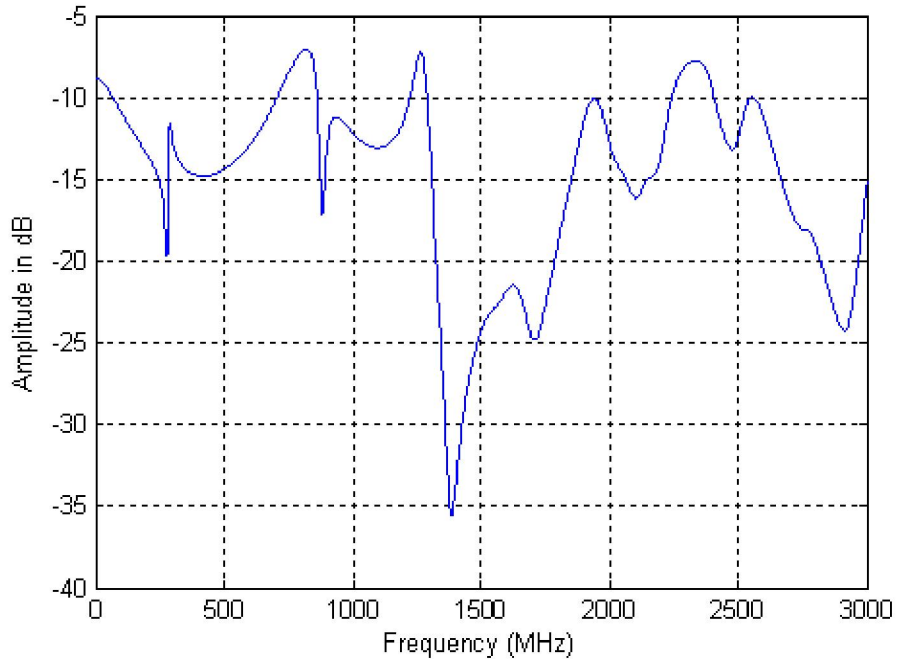


**Figure 4.27 Transmission of a distributive loaded resonator inside the phantom.**

As clearly seen from Figure 4.30, the overall transmission is decreased due to the lossy characteristics of the phantom. This is expected but not desired. It is

difficult to understand the resonance behavior of this structure from such a far observation point. We should work with this data, which will be the real world case. This structure is the same with the one given in Figure 4.11 with a dielectric film thickness of 500  $\mu\text{m}$ . If we compare these two figures, we can clearly see that the resonance frequency is shifted from 350 to 280 MHz. This corresponds to 20% resonance frequency shift compared to the free space case. It seems that the natural medium in the human body will help us to decrease the resonance frequency at a cost of reduced resonance quality. The trade-off between resonance frequency adjustment and the resonance quality is a difficult problem and the preservation of resonance quality has the priority. Another point is the decreased electric field intensity near the resonator that is in complete agreement with the theory of electromagnetic. This degradation is definitely due to the conductivity of phantom. Electric field distributions of the resonator at its resonance frequency for different planes and the current distribution of the resonator, which is also in good agreement with [27], are given in Figure 4.28, 4.29.

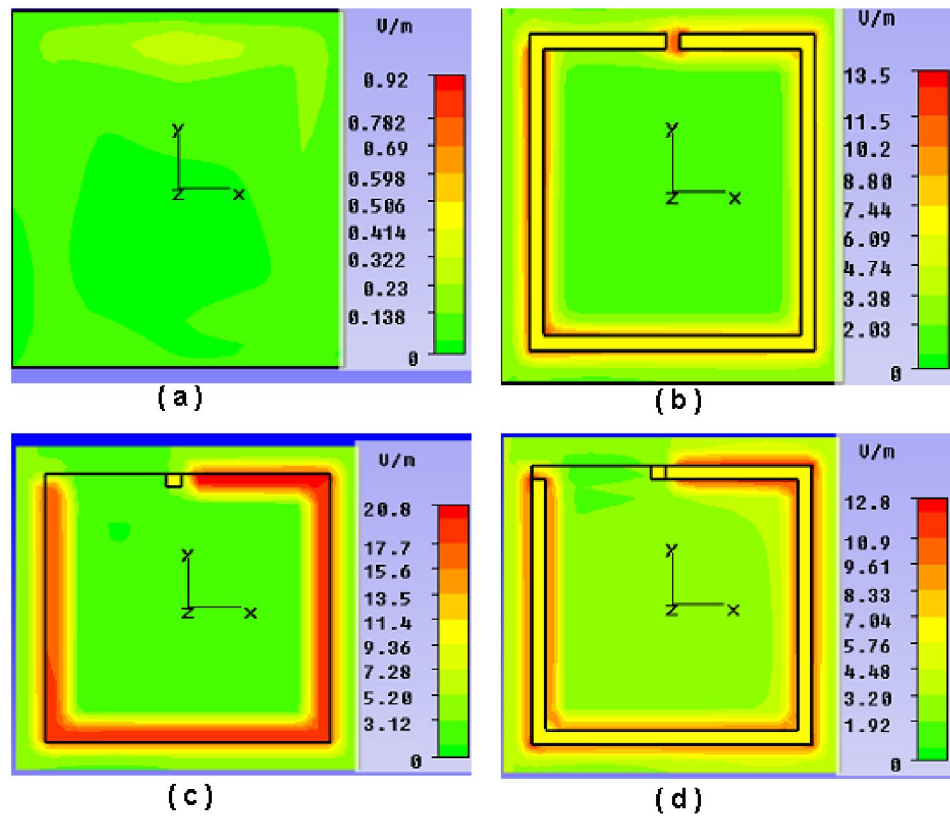


Figure 4.28 Electric field distribution of the structure for different planes: a) 1 mm inside the phantom on the back, b) at the bottom ring, c) in the middle of the plates, and d) at the top ring

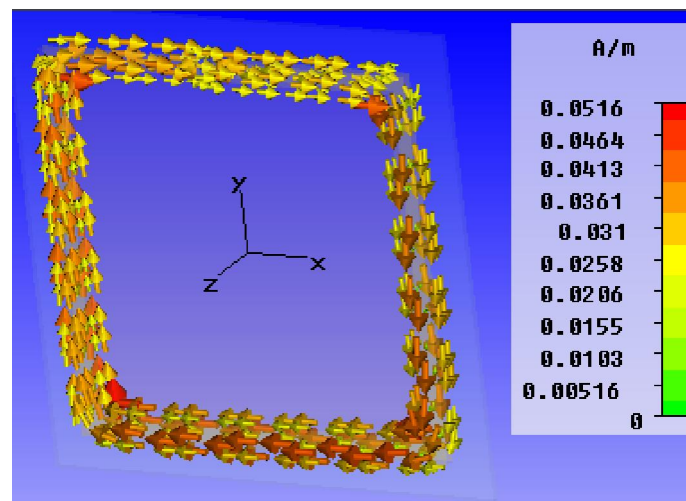


Figure 4.29 Current distribution of the structure.

As seen from the Figure 4.31, field cannot go through the phantom, even at a 1 mm distance from the structure. It decays less than 5% of its value on the resonator. Although most of the field is confined in the phantom located in front of the resonator, it can still confine the field between its parallel plates. It is clear that the major problem with the phantom is the loss due to its conductivity. However, this is not a big concern for us because the nature of the body. This loss will be there, and we will only be dealing with the neighborhood of the resonator.

In conclusion, this structure can handle the loss problems in principle due to field confinement and handles current distribution problems in classical SRRs at lower resonance frequencies. The inductively coupled nature of thin film loaded SRR will grasp more energy from the transmitting coils of the MRI system and, then excite the nuclei more than the normal case, amplifying the signal because of its quality factor. Next chapter will discuss the fabrication steps and its imaging performances of the proposed RF structures from the MRI perspective.

# Chapter 5

## MRI OF DISTRIBUTIVELY LOADED RESONATORS

MRI is a powerful diagnostic technique in clinical studies thanks to its non-invasive and electrically safe nature. Although MRI is a non-invasive method, experimental works show that it is very promising to use it for interventional purposes such as active catheter tracking [28] and catheter based biliary imaging [29], and recently for liver duct imaging [30]. All of the MRI tools used in these works need tuning and matching capacitors to work in the desired frequency, thus requiring large volumes to be implanted into the body if it were permanently. This chapter will concentrate on the fabrication and MRI characterization of our distributively loaded resonators, both for the cases inside and outside the body. In this thesis, experiments were performed using a body-mimicking phantom.

### 5.1 Micro-fabrication of Resonators

As we mentioned earlier, fabrication is one of the milestones of this novel class of resonators. Not only the miniaturization limit but also the flexibility and resonance quality are dependent on the fabrication methods. To follow the chronology, we will start to discuss the fabrication steps of the novel structure on rigid substrates, such as silicon and quartz, and then will overview the fabrication methods of flexible structures.

### **5.1.1 Micro-fabrication of Resonators on a Rigid Substrate**

Determining the size of a resonator for MRI is a difficult task due to the complexity of implantable devices. Microfabrication methods place constraints on the feasible aspect ratios and physical necessary dimensions to construct high quality resonators. Our previously performed simulations and prior expertise of our group were the candles of the fabrication development. Sometimes, it would take months to find the correct material for the right processing methods, or in an even worse, to indentify and correct a sneaky mistake. Our resonator architecture is composed of two metal layers (lower and upper rings) separated with a dielectric film, which also contains a via opening to form an electrical connection between the sandwiching lower and upper metal layers.

The first step of microfabrication is the selection of a correct substrate. For our purposes, it must be a non-conducting, un-doped, (or low-doped) silicon wafer. In classical microfabrication methods, highly doped silicon wafers are very common and widely used for semiconducting on-chip devices. Conductive substrates causes signal degradation and even reflection of incident wave off their surfaces in MRI.

We fabricated our resonators on a 380- $\mu\text{m}$  thick, low-doped silicon substrate with the lattice orientation of [111]. The predefined mask layout of the lower ring has the 20 mm by 20 mm footprint area with a patterned metallic layer of 1 mm feature in width as shown in Figure 5.1. This layout is patterned on a chrome-coated mask to be used in standard lithography steps [31].

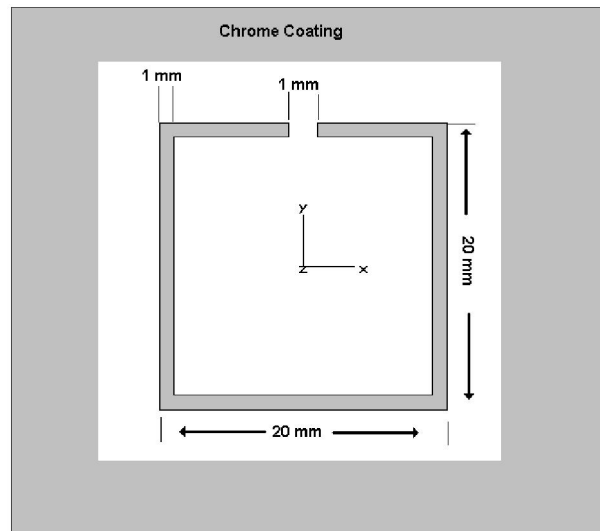


**Figure 5.1 Layout of our chrome coated quartz mask for the lower ring (the first metal layer).**

We start our microfabrication process by cleaning the wafer in piranha solution, which is composed of sulfuric acid and hydrogen peroxide with a ratio of 3:1, for 10 min. followed by a de-ionized (DI) water bath of 2 min. Cleaned wafers are spin-coated with a positive photoresist (AZ5214E) [32], which provides image reversal, at a rate of 5000 rpm for 50 s followed by prebaking at 110 °C for 60s to make it photosensitive. The coated resist is then exposed to ultraviolet (UV) light at a wavelength of 365 nm, with an intensity of 3 mW/cm<sup>2</sup> for 30 s under the hard contacted mask followed by a soft baking procedure at 120 °C, for 120 s. The prepared structure is exposed to the UV for 10 s again to achieve image reversal. The development of the exposed structure takes about 30 s to be completely removed off the wafer using AZ 400K developer. At this stage, the layout of the structure now can be seen with a bare eye.

The fabrication process continues with the thermal evaporation of a 10 nm thick titanium (Ti) film as the adhesive layer between the substrate and the upper 100 nm thick gold (Au) layer. Subsequent lift-off is carried out by using acetone ((CH<sub>3</sub>)<sub>2</sub>CO) to remove residues of the photoresist from untreated spots. In the next step, rapid thermal annealing (RTA) allows Ti/Au layer to make alloy, which is necessary before the electroplating step. To eliminate skin depth effect,

it is necessary to thicken our metallic lines at least to 14  $\mu\text{m}$ , which is two times the skin depth of gold at 123 MHz. Therefore, we electroplate an about 20  $\mu\text{m}$  Au film to have sufficiently thick conductive lines. After mechanical polishing of the lower ring following electroplating, we obtain non-uniformity level less than 2  $\mu\text{m}$  on the surface, which would be a problem if the dielectric layer thickness is less than 2  $\mu\text{m}$  [33].

Next, dielectric coating is a straightforward process, which consist of spin-coating SU-8 (3050) photoresist [34] at 4000 rpm of 2 min. This results in a 40  $\mu\text{m}$  thick resist film, which will completely bury the patterned lower ring within this dielectric layer. The contact point is opened via a hole using the recommended developer (supplied by Micro•Chem™) by applying standard UV photolithography techniques as outlined above. We electroplated a gold via on top of the lower ring through the opening to be planar with the dielectric layer, which is important to lay down a good metallic contact to the upper ring.

The same processing steps of the lower ring are repeated for the upper ring with the same materials and durations, except for the polishing step. There is no need to polish the structure after the upper ring since we will not further coat it with another layer. The geometry of the upper ring is slightly different than the lower ring due to the need for intentional physically overlapping regions. The mask for the upper ring is presented in Figure 5.2.

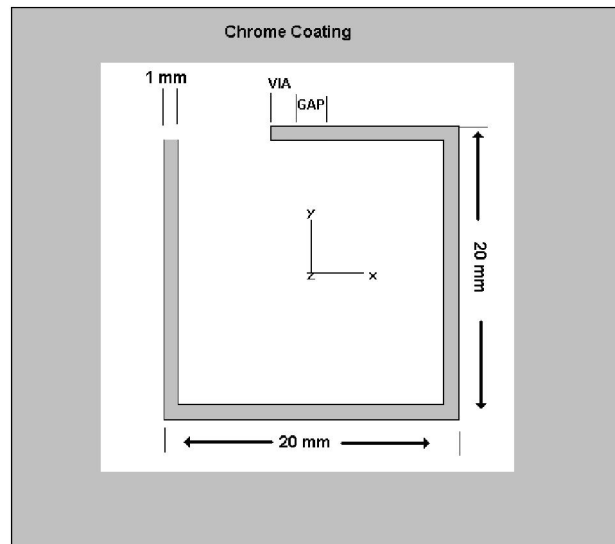


**Figure 5.2** Layout of the chrome coated quartz mask for the upper ring (the second metal layer).

The completed resonator structure is indeed like a helix-shaped ring as previously given in the simulation layouts. This device is now ready to be tuned and used for imaging experiments. The complete fabrication flow can be seen in the cross-section view of the fabricated chip step by step in the Figure 5.3.

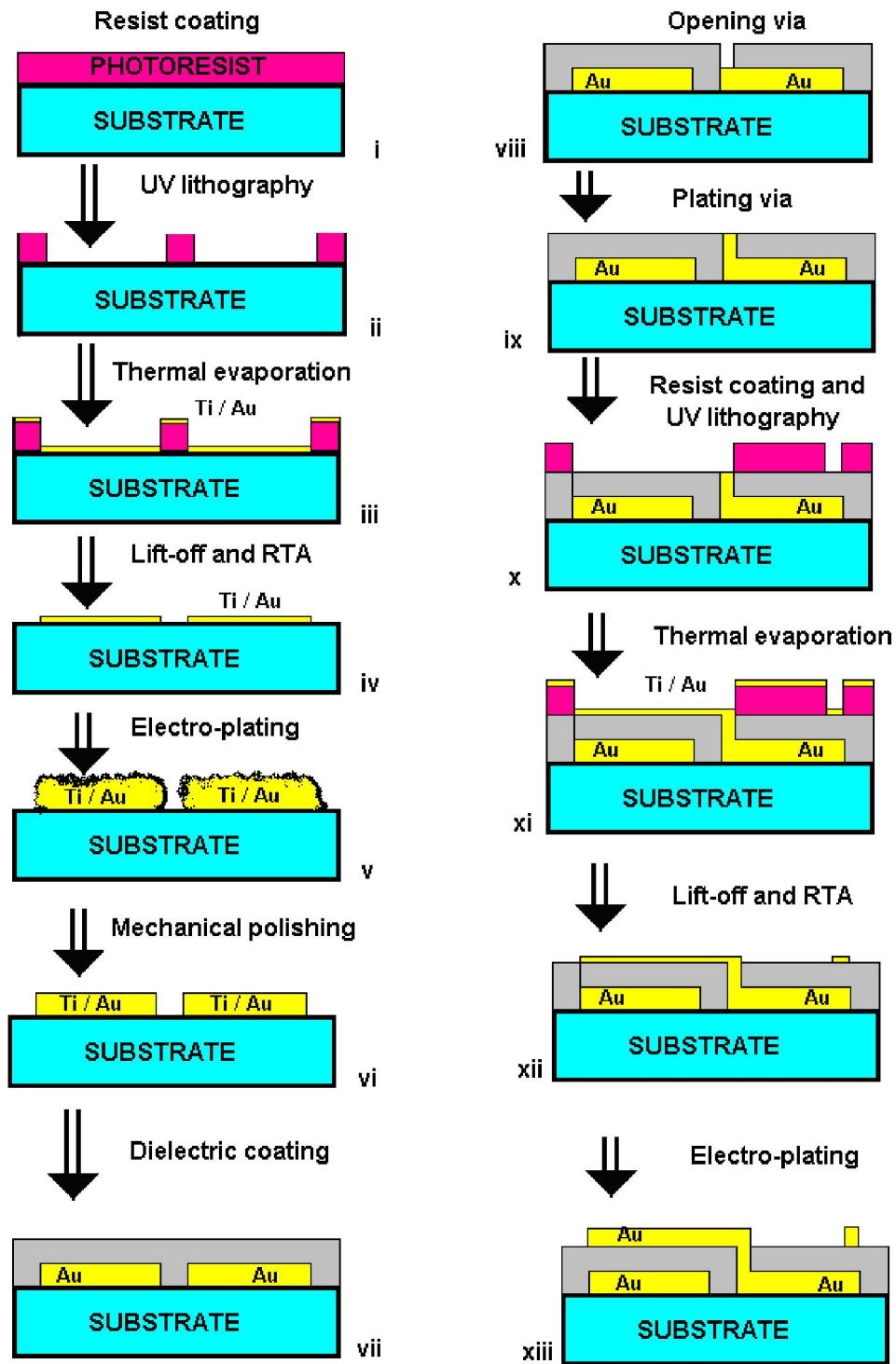


Figure 5.3 Process flow for fabrication on a rigid substrate.

## 5.1.2 Micro-fabrication of Resonators on a Flexible Substrate

It is necessary to fabricate this resonator structure also on a flexible substrate to make it more useful for non-planar tissue surfaces and implantable devices. Depending on the application, this structure can be embedded inside the body permanently or temporarily. However, in either case, it should be biocompatible. For that reason, we choose Kapton® (HN100) polyimide film, acquired from DuPont™ Corporation, as the substrate for our structure [35]. It is biocompatible and has been already used for in-vivo applications by Melik et al [20] in our group. Different from the fabrication on a rigid substrate, here the Kapton® film serves not as the substrate of the structure, but also as the dielectric of the resonator to make the resulting device overall thinner.

The relative permittivity of the Kapton® film is given to be approximately 3.3 in the RF range and stable over a wide range of frequencies. Simulation results showed that, for a 25  $\mu\text{m}$  thick Kapton®, it will be possible to reach 123 MHz of resonance frequency with our previously determined footprints of 20 mm by 20 mm. By using the Kapton film also, as the dielectric region, we can decrease the overall device thickness to be around 75  $\mu\text{m}$ . Such a thin structure can be very flexible in transverse plane, which allows it to be bent easily and cover non-planar surfaces.

Both the flexible nature of the Kapton film and the brittle nature of the plated gold layer cause obstruction and introduce technical challenges in the fabrication of this resonator structure. Thus, the fabrication steps have to be modified to overcome these difficulties. As the starting point, the Kapton is cleaned by piranha solution to remove organic contamination from its surface and fixed to a rigid substrate to be mechanically handled during lithograph. The standard lithography steps, as mentioned in previous section, are carried out for the upper side of the film. This is followed by the metal evaporation of titanium and gold with film thicknesses of 20 nm and 100 nm, respectively. Then, the Kapton film is turned upside down and the upper ring layer is coated and patterned with the

same metallic layers with proper alignment to the lower ring layer. This two side coated structure is annealed by RTA 300°C for 2 min.

One of the different steps from the previous process how for a rigid substrate is the milling to form a via. Milling is done at this stage. Now we obtain a two side coated thin film structure with an opening, which does not have a contact between the upper and bottom layers at this point. Also the metallic layer is too thin (120 nm) to be used in RF region. The Kapton substrate is therefore fixed from its corners again and attached to a rigid substrate to start electroplating. On the upper metallic line is plated first a 20  $\mu\text{m}$  thick Au film, on which the connection to the lower ring is also made because of isotropic property of this technique. The thickened upper ring is now isolated with a 75  $\mu\text{m}$  thick part of the Kapton tape to prevent metallic lines from splitting at this step. The substrate is again turned upside down to be electrodeposited from the lower ring. This layer also thickened to 20  $\mu\text{m}$  to be more conductive in RF region. We now have the resonator structure with a thickness of 65  $\mu\text{m}$  with the isolation of 75  $\mu\text{m}$  in thickness from each side. The total thickness is almost 215  $\mu\text{m}$  with a less than 10% thickness deviation due to the electroplating process. Complete microfabrication process flow is presented in Figure 5.4.

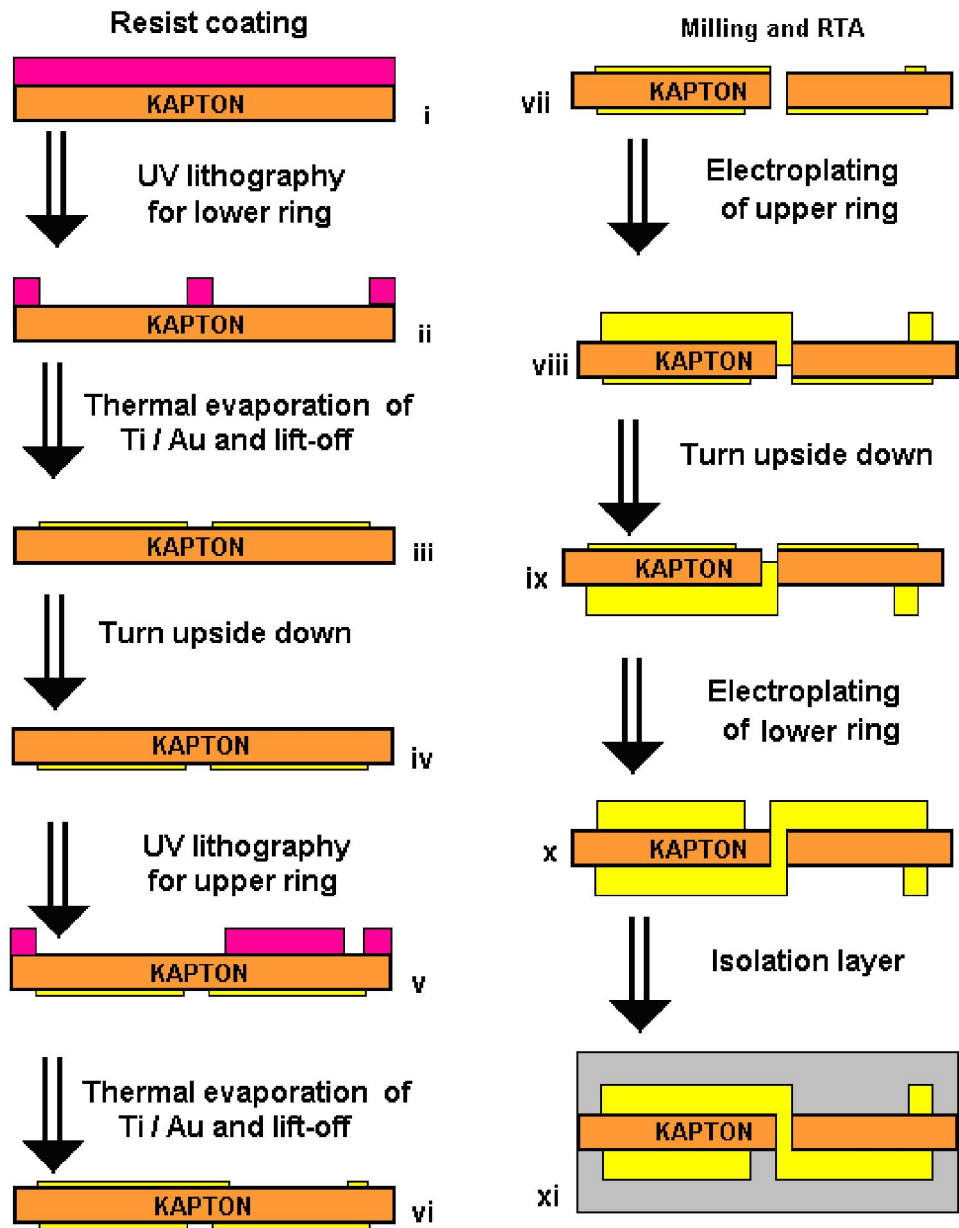


Figure 5.4 Process flow for fabrication on a flexible substrate.

## 5.2 Resonators Employed as External Devices

Imaging the body from outside with a homogenized field distribution is a challenging work. As explained in the beginning of the thesis, closed coil geometries such as birdcage coil can amplify fields at the internal spatial points. Since the bandwidth of the MR environment is below 200 kHz, it is considered as a narrow band, non-dispersive medium. These properties attracted attention of the metamaterial society in the previous years [36,37]. The mapping of frequency to spatial points allows scientists to focus MRI signals to the receiver antennas by using artificial lenses [38,39]. According to these reports, this does not affect the signal processing of MRI and thus does not introduce any extra noise to the system.

Basic explanation to the operating principle of a resonator relies on two major mechanisms: flip angle modification and signal coupling to the receiver coils. The first one is effective at the lower flip angle excitations, where as the second is effective for all imaging angles and sequences. For smaller flip angle excitation phantom does not emit much power, yielding a weaker signal level, which in turn results in low signal-to-noise ratio (SNR). The resonator receives some of the power from the RF coils by inductive coupling and re-aligns the nuclei near it with higher flip angles, which leads to high SNR and bright image areas.

When the flip angle of the image is increased, the phantom also emits stronger signals, which results in brighter images at every point, with the resonator artifacts. Of course this is not a desired condition and can be solved both by software and by hardware separately. The first method includes modification of the sequence parameters, which is not convenient for radiologists due to specific tissue characteristics. The second method, which is more convenient and widely used by RF coil designers to eliminate these artifacts, is the decoupling of resonators using back-to-back connection of schottky diodes. This method is easy to apply for bigger coils and resonators, but decreases the field

amplification factor [40]. Even in this case, the resonator can emit more power than the phantom at some points, which is known as the coupling enhancement.

For external imaging practices, we fabricated the previously described self-resonating structures on rigid and flexible substrates and, attaching them to the surface of phantom, their coronal images are then received. This phantom is prepared by dissolving 4 g of copper sulfide ( $\text{Cu(II)SO}_4$ ) with an additional 2 g of sodium chloride ( $\text{NaCl}$ ) in 1 L of water. The phantom has a bright blue color with some un-dissolved solid particles, featuring a T1 relaxation time around 400 ms with a conductivity of around 1 S/m and relative permittivity of around 80. These properties make the phantom electromagnetically mimic blood. This is called the body-mimicking phantom for the rest of this thesis. These images were received by using gradient echo (GE) signal sequence, with a repetition time (TR) of 100 ms, and an echo time (TE) of 10 ms. The field of view is 120 mm and the resolution of 256 pixels by 256 pixels in X-Z plane corresponds to  $0.47 \text{ mm} \times 0.47 \text{ mm} \times 5.00 \text{ mm}$  voxel dimensions. The received images for different flip angles are given in Figures 5.5-5.16 to show the relation between the flip angle and the intensity enhancement.

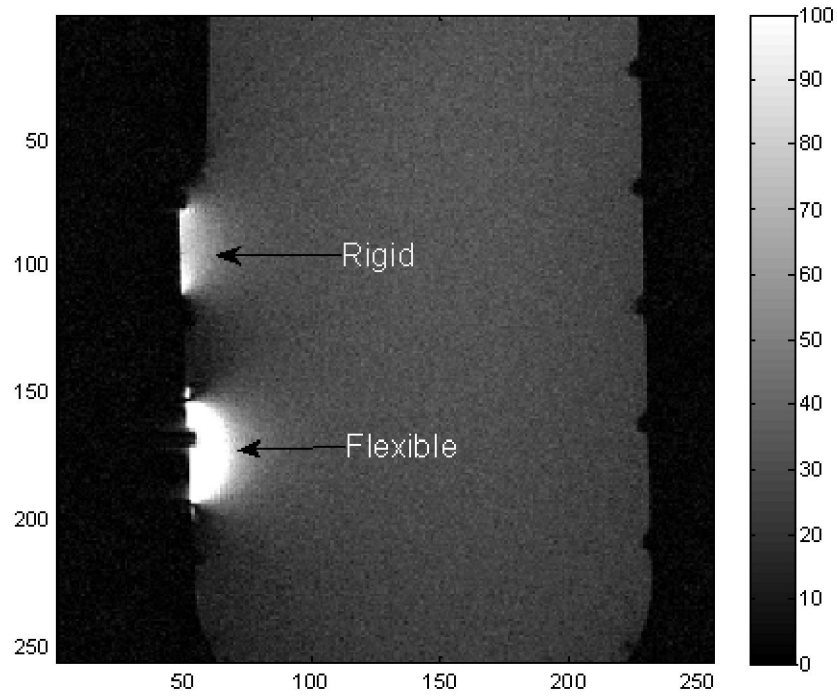


Figure 5.5 MRI of the resonators with a flip angle of 5°.

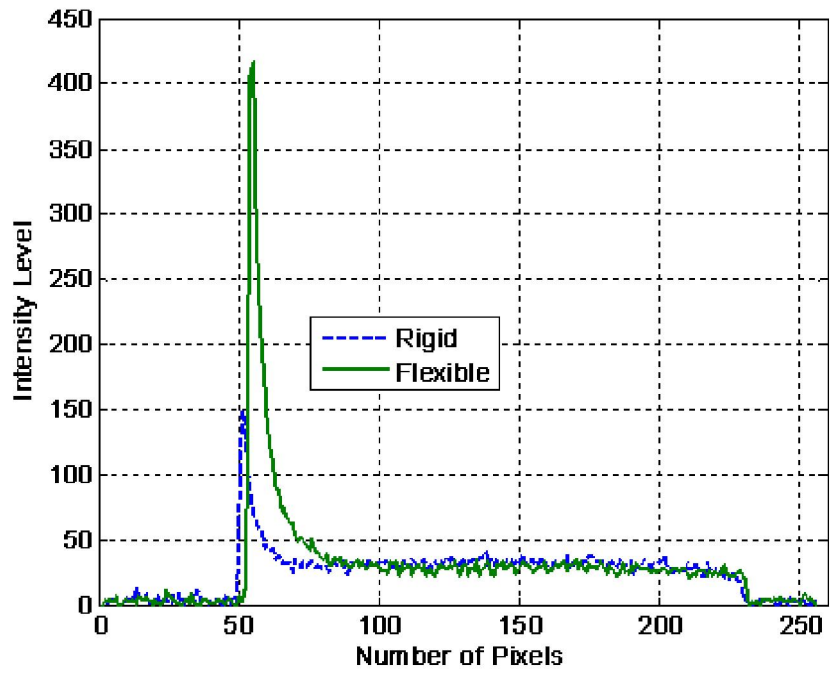


Figure 5.6 Intensity level distribution along the horizontal axes of the resonators.

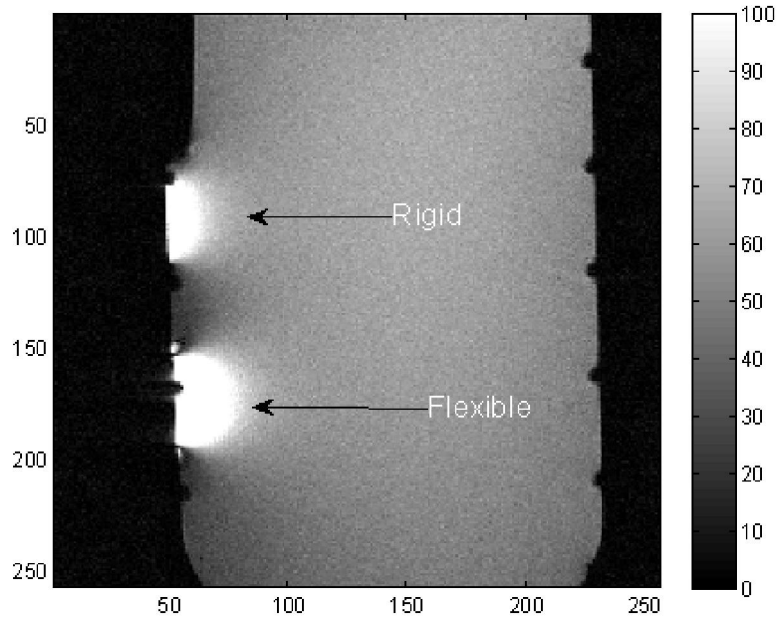


Figure 5.7 MRI of the resonators with a flip angle of  $10^\circ$ .

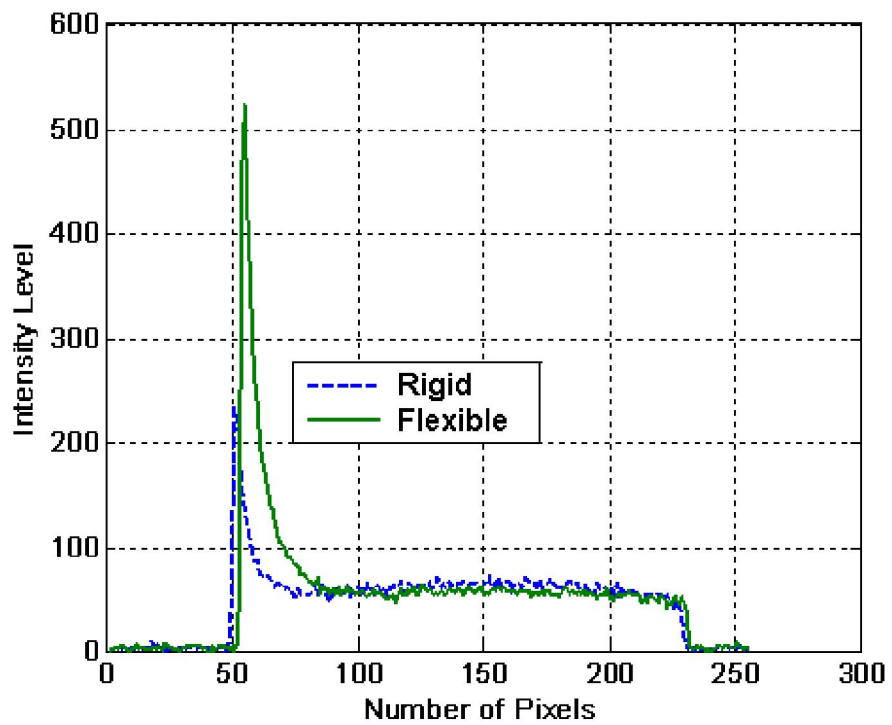


Figure 5.8 Intensity level distribution along the horizontal axes of the resonators.

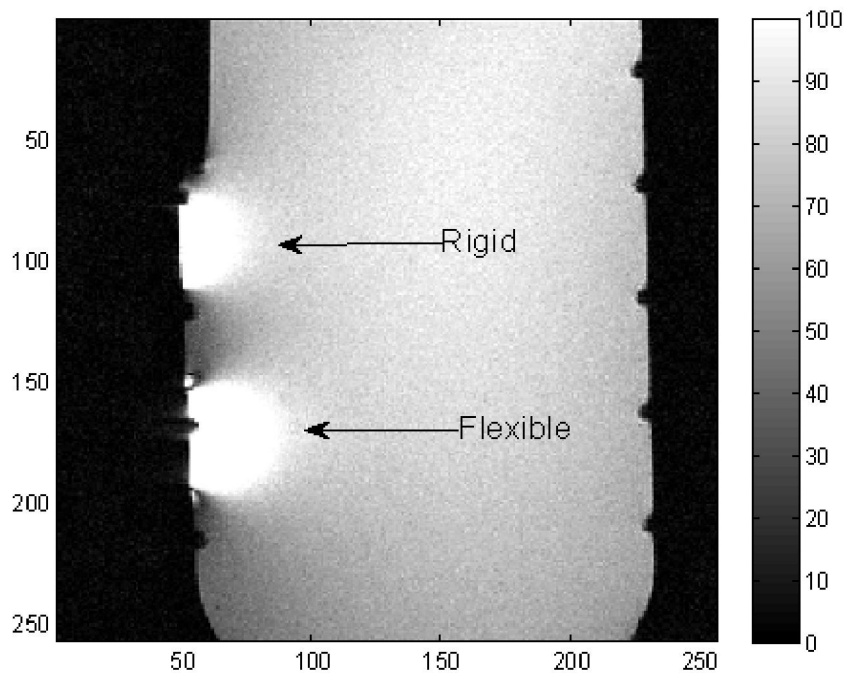


Figure 5.9 MRI of the resonators with a flip angle of 15°.

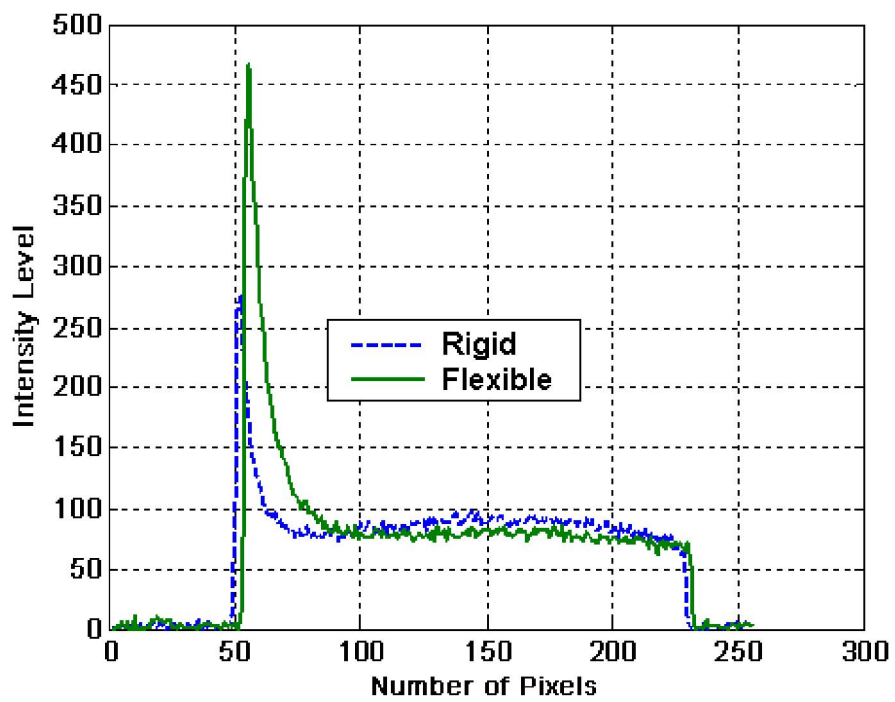


Figure 5.10 Intensity level distribution along the horizontal axes of the resonators.

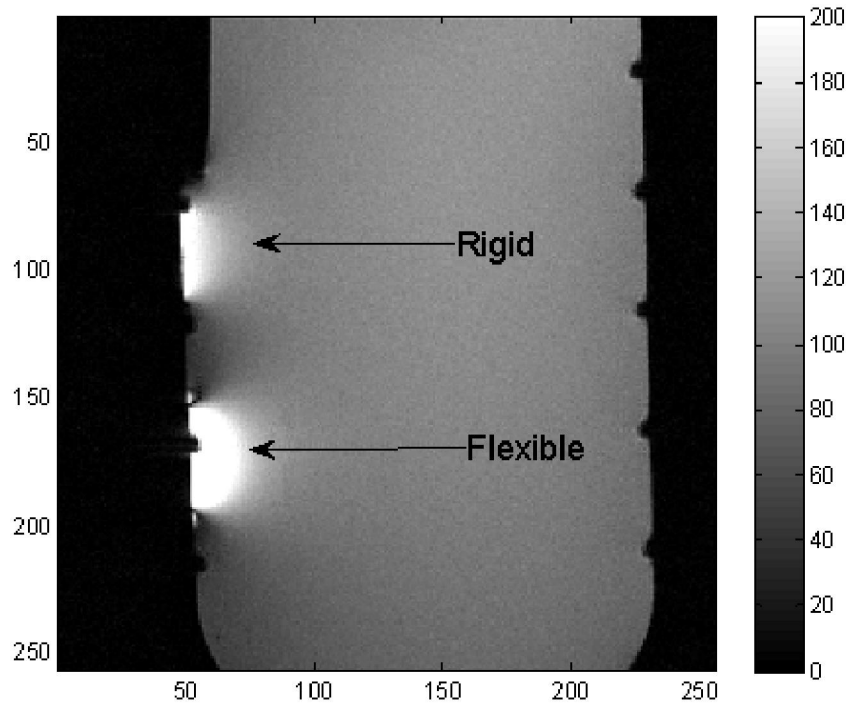


Figure 5.11 MRI of the resonators with a flip angle of 20°.

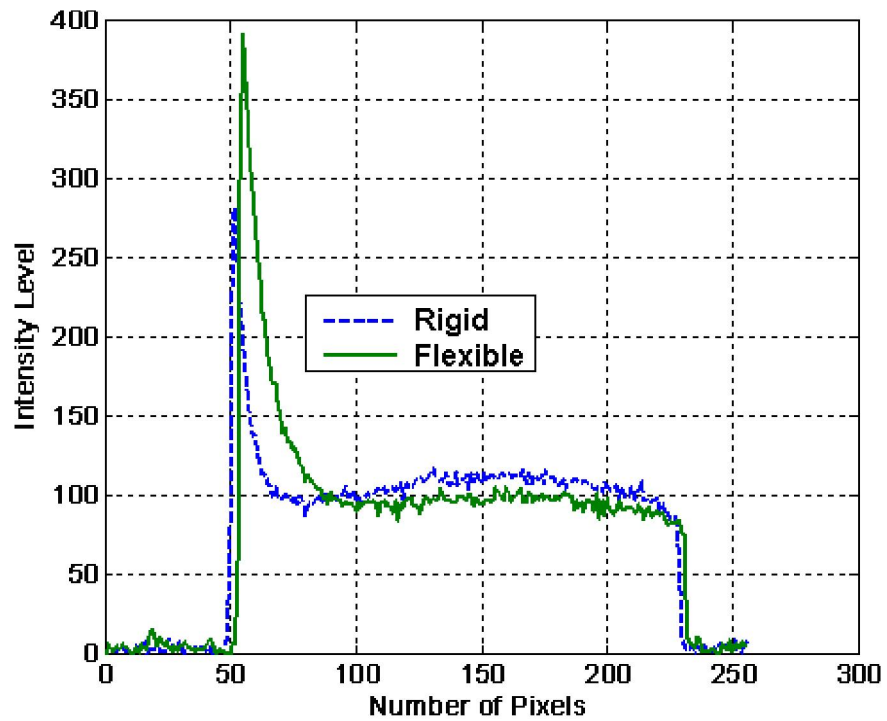


Figure 5.12 Intensity level distribution along the horizontal axes of the resonators.

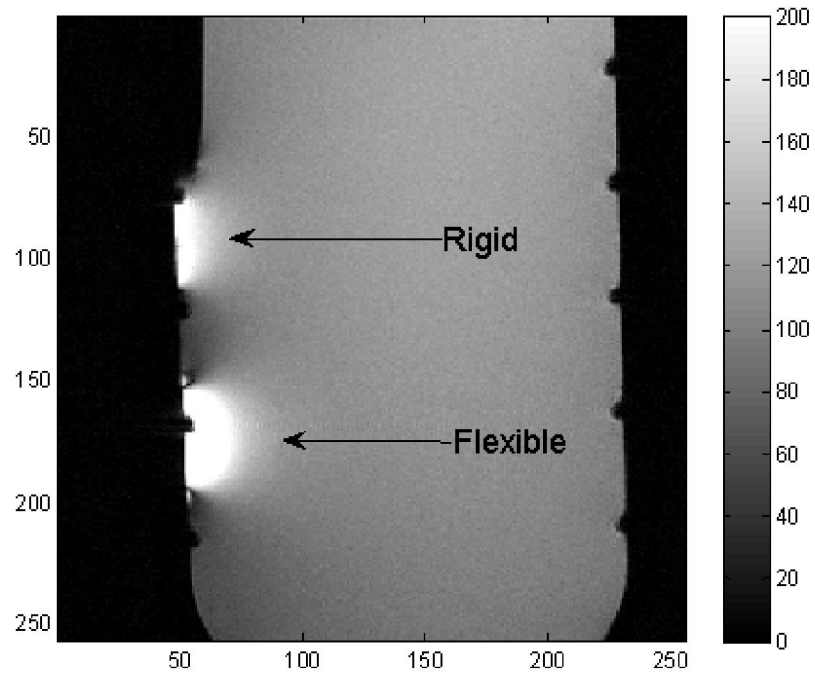


Figure 5.13 MRI of the resonators with a flip angle of 25°.

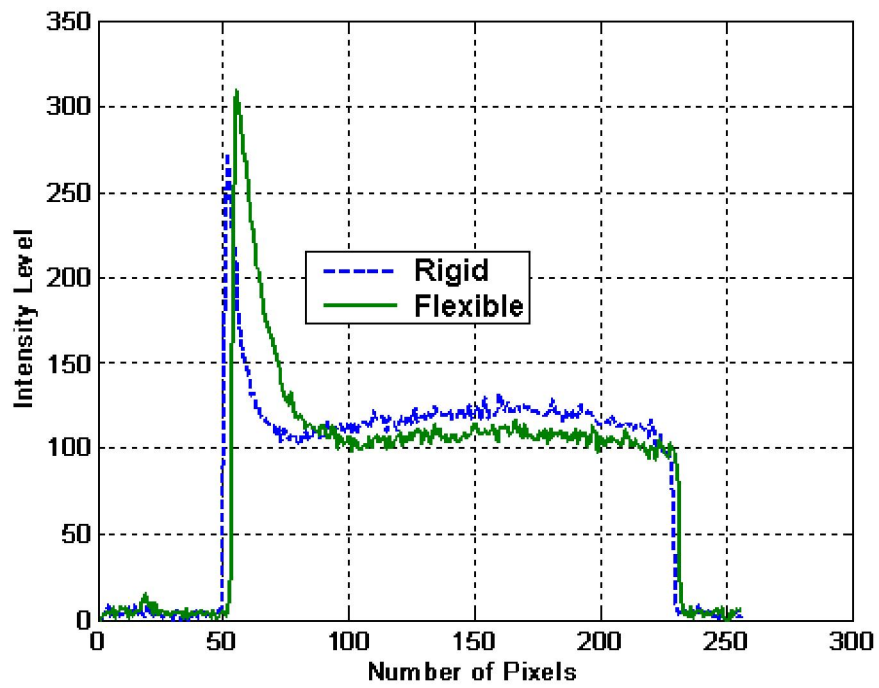


Figure 5.14 Intensity level distribution along the horizontal axes of the resonators.

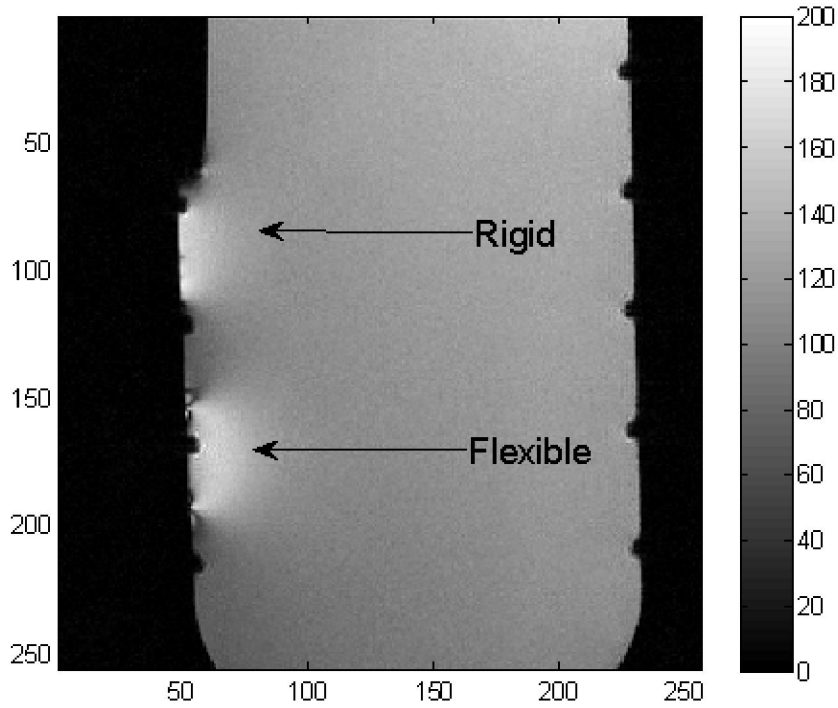


Figure 5.15 MRI of the resonators with a flip angle of 50°.

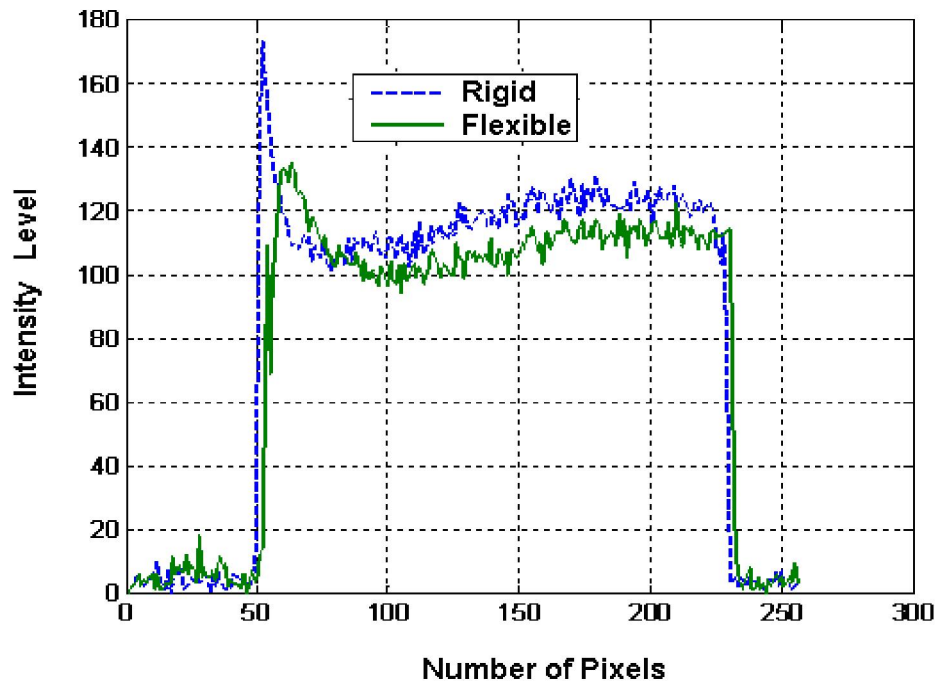


Figure 5.16 Intensity level distribution along the horizontal axes of resonators.

As clearly seen from the figures above; the flexible resonator structure can cover the cylindrical surfaces better than the rigid structure, thus leading to wider effective areas with higher field intensities. The problem here is the distribution of these points along the phantom. Since the loss mechanism of the phantom does not allow resonators to affect far points, we cannot achieve an image enhancement in the depth of phantom. Intensity traces following each MR image show the intensity distributions along the central axes of the resonators. They clearly indicate that the intensity distribution diminishes rapidly into the depths of the phantom due to the loss.

An additional conclusion for these characterizations is the intensity enhancement of the resonators varies as the flip angle excitation changes. To clarify this point, we recorded the maximum intensity level that can be reached by using the respective resonator and the resulting intensity level of phantom for different flip angles. Figure 5.17 clearly shows the flip angle behavior of the resonators and the magnetization signal of the phantom.

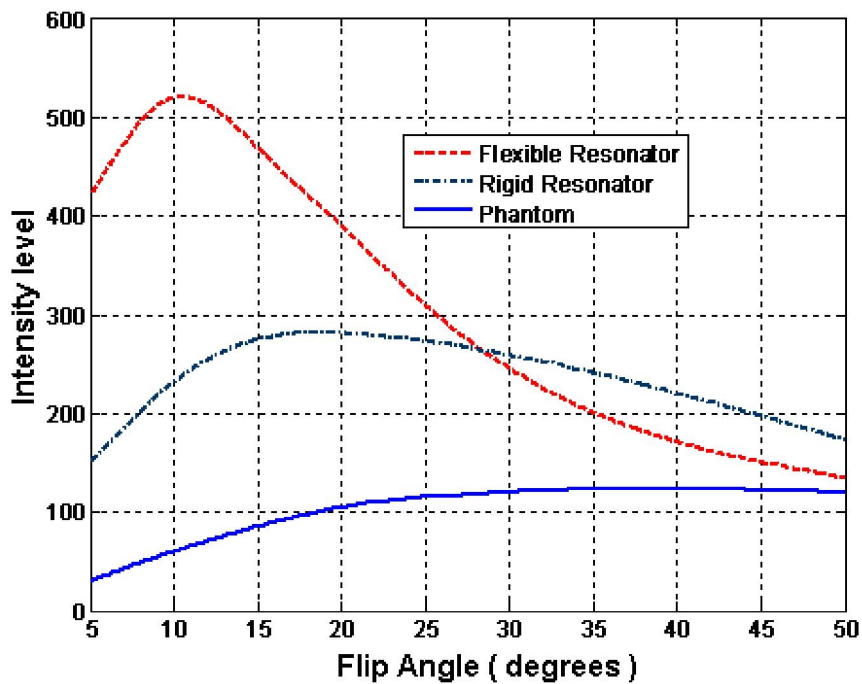


Figure 5.17 Intensity amplification of the resonators for different flip angles.

As clearly seen from the Figure 5.17, these inductively coupled resonators can best work in smaller flip angles for external imaging. Another conclusion that can be derived from this figure is the extraordinary signal level increment around 5° of excitation, which is around 14 folds with respect to the phantom levels without a resonator.

To analyze the MRI performances of the structures, we proposed the following performance metrics. Enhancement factor (E.F( )) is defined as the ratio of maximum intensities of the images with resonator to the resonator free cases for the same flip angles. Enhancement limit (E.L( )) is defined as the ratio of image intensities for the resonator case at each flip angle to the best case of the resonator free case, which also called the Ernst angle as implemented in (5.3). These metrics are given in 5.1 and 5.2 as follows.

$$E.F(\theta) = \frac{I_{resonator}(\theta)}{I_{phantom}(\theta)} \quad (5.1)$$

$$E.L(\theta) = \frac{I_{resonator}(\theta)}{I_{phantom\ best}} \quad (5.2)$$

where  $\theta$  is the flip angle and the I corresponds to the image intensity.  $I_{phantom\ best}$  can be considered as the image intensity with an excitation flip angle of Ernst' angle as formulated by (5.3)

$$\theta_E = \cos^{-1}\left(e^{-\frac{TR}{T_1}}\right) \quad (5.3)$$

Due to the Ernst angle formulation, the maximum signal level, for the phantom only case, can be achieved around 39° of excitation for TR=100 ms and T1=400 ms. Here, the maximum signal level for the phantom only case is around 120, where the maxima are 280 and 520 for rigid and flexible resonators respectively. This effect is due to the quality factors of the resonators.

Figure 5.18 represents the enhancement factor (E.F) for each excitation angle, whereas Figure 5.19 shows the enhancement limit for both resonators, respectively.

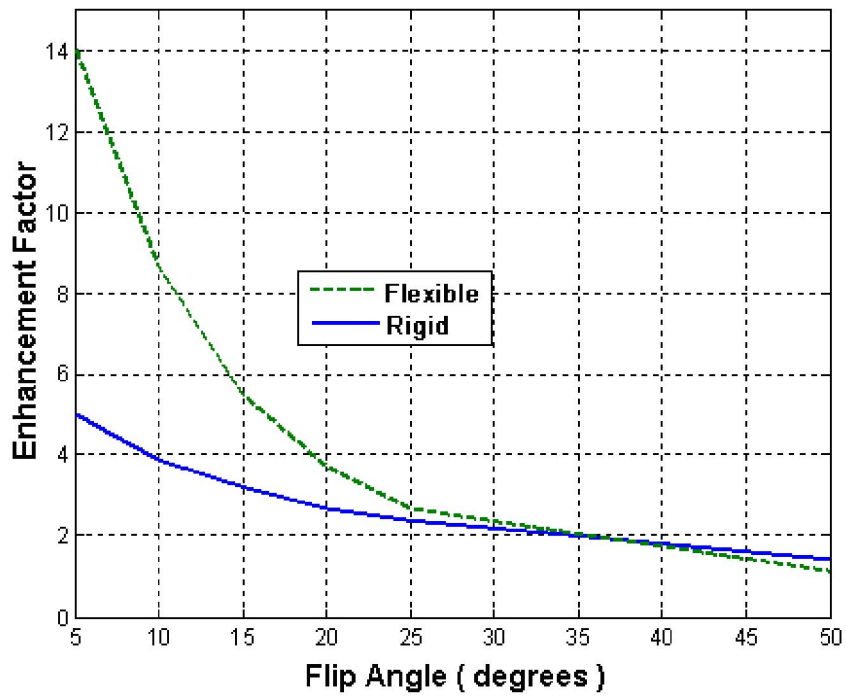


Figure 5.18 Enhancement factor due to flip angle excitation.

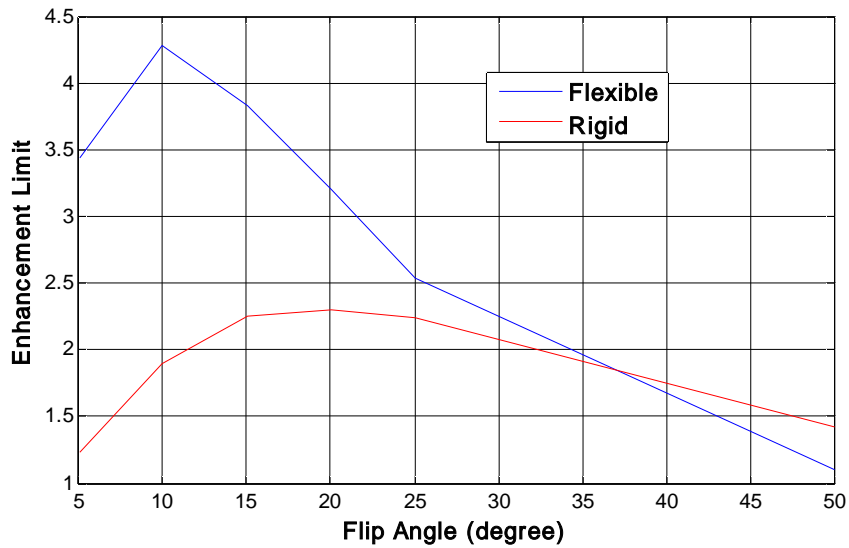


Figure 5.19 Enhancement limit for external imaging due to different flip angles.

In operation, a resonator receives MR signal from the phantom and couples it to the receiver antennas as in ICRF coils [41]. This direct forward application encourages us to study internal imaging setups with the same phantom.

## 5.3 Resonators Employed as Internal Devices

### 5.3.1 Phantom Imaging Using Classical Resonator

It is a well-known phenomenon that the wireless resonators inside the body can re-distribute the flip angles of the nuclei in near field thus leading flip angle amplification. A sample image of an SRR tuned by lumped capacitors inside a phantom can be seen in Figure 5.19.

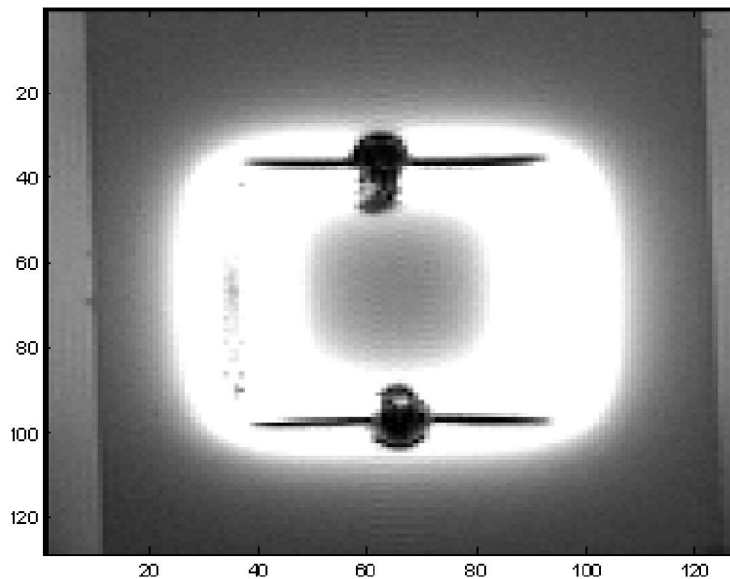
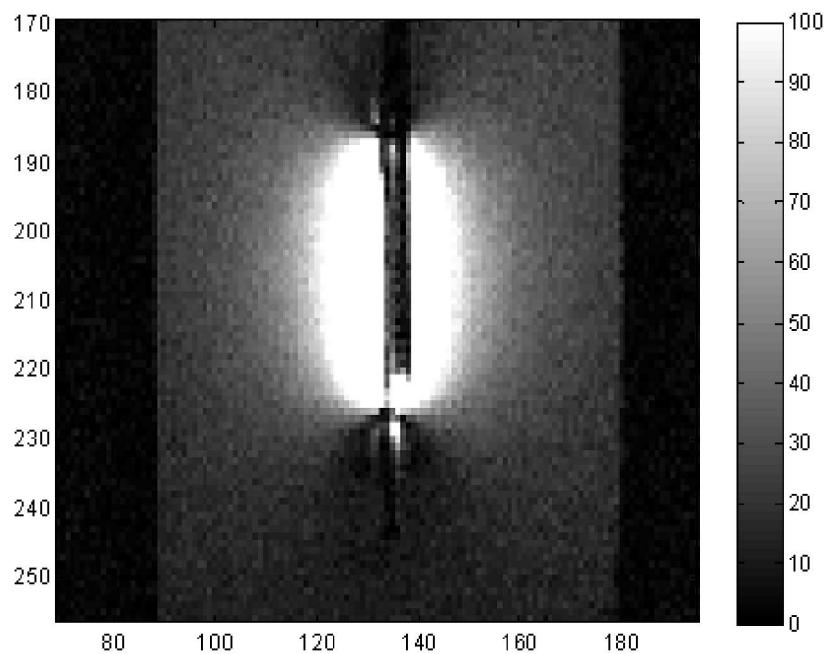


**Figure 5.20** A sample image of an SRR inside the phantom.

It is clear that the signal coming from the metallic lines of the SRR is higher than the far regions. For this sample image, this signal level is increased at most 5 times compared to the far regions and can still amplify the imaging signal around 1 cm away from it. This isolated SRR, with its two capacitors loading its splits, is too bulky to be implanted even for smaller ring diameters. It is also clear that the image intensity drops near the capacitors due to the transformation of conduction current to displacement current. Although capacitors are non-magnetic, there are black regions instead of bright areas, meaning that non-amplified regions exist near the lumped capacitors due to isolation material, which is not MR visible.

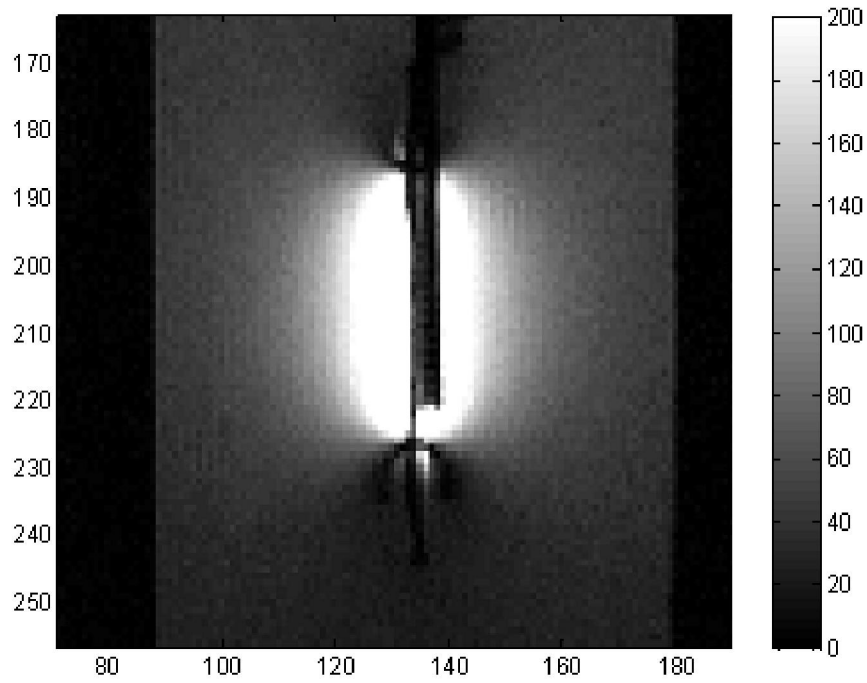
### 5.3.2 Phantom Imaging Using Novel Rigid Resonators

The proposed novel resonating structure with its distributed capacitance can also amplify the field in the vicinity of its metallic lines without any constraint unlike the classical ones. Figure 5.21 shows an example sagittal image of the fully loaded resonator on a rigid substrate excited with a flip angle of  $5^\circ$ . Here each pixel corresponds to 0.47 mm in both directions.

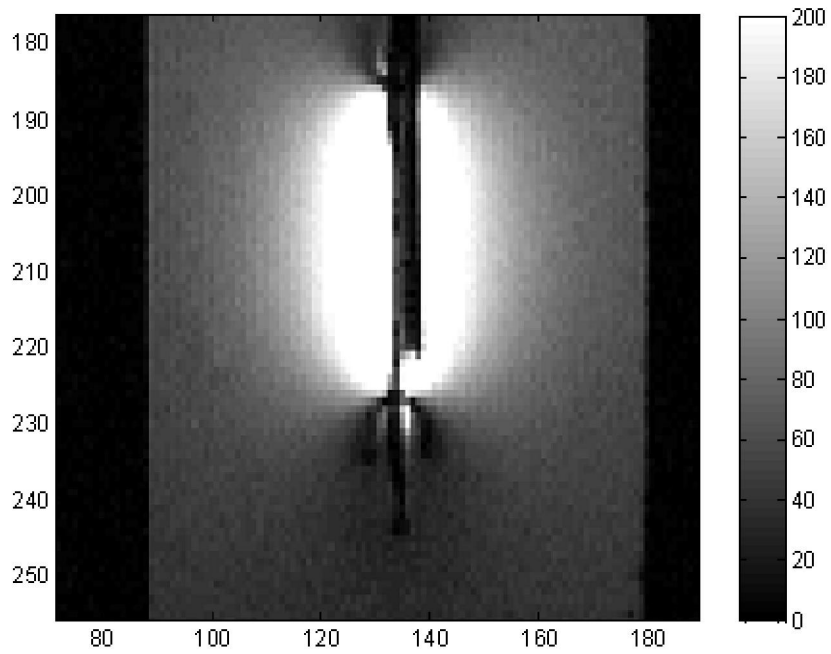


**Figure 5.21 MRI of the novel resonating structure on a rigid substrate for a flip angle of  $5^\circ$ .**

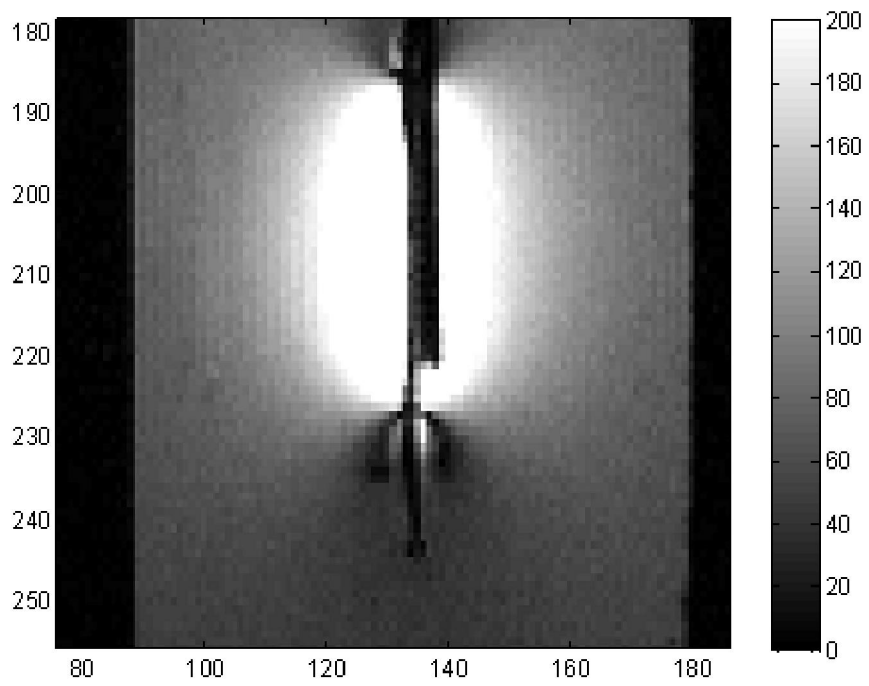
The noise level in this image is around 8 while the intensity of the image for the phantom is around 28. The distance in horizontal direction, where the image intensity is 2 folds of the phantom is around 20 mm and the maximum intensity enhancement is around 350, which is almost 12 times the phantom only case. MR images of the structure for different flip angles are given in the following figures. The noise level and phantom intensity increase with the flip angle, where the maximum signal intensity decreases as the flip angle increases. Figures 5.22-25 show the MR images of the novel resonator on a rigid substrate with different flip angle excitations.



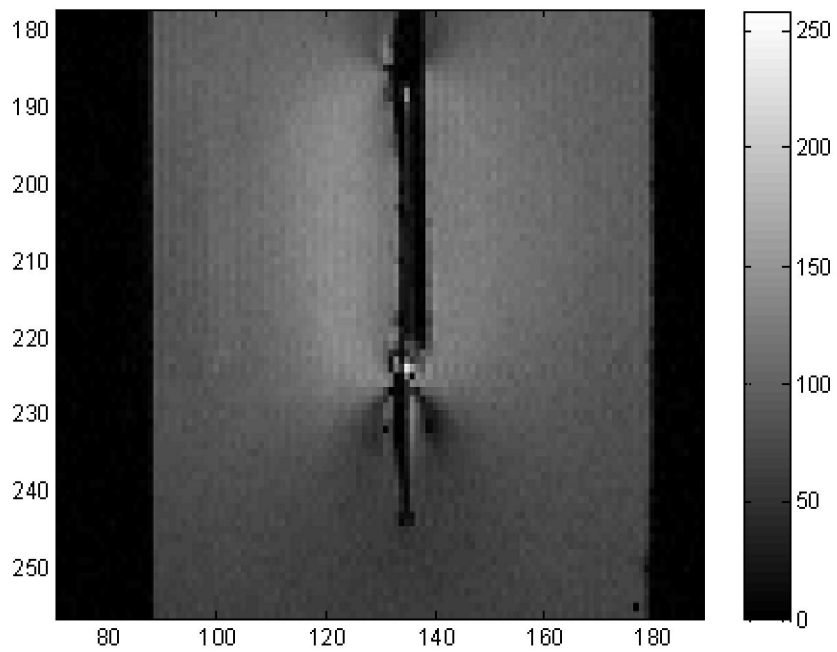
**Figure 5.22 MRI of the novel resonator structure on a rigid substrate for 10° flip angle.**



**Figure 5.23 MRI of the novel resonator structure on a rigid substrate for 15° flip angle.**

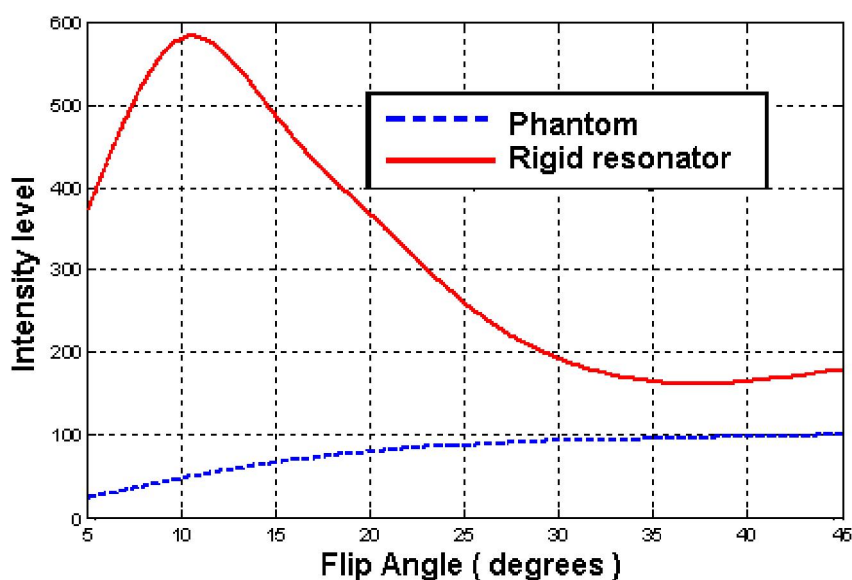


**Figure 5.24** MRI of the novel resonator structure on a rigid substrate for a flip angle of  $20^\circ$ .



**Figure 5.25** MRI of the novel resonator structure on a rigid substrate for a flip angle of  $45^\circ$ .

The distance of 2-fold amplification is always more than 9 mm in both directions, which makes 18 mm in total, for any flip angle distribution smaller than  $25^\circ$ . As clearly seen from the figures, intensity distribution decreases rapidly as we move away from the resonator due to the lossy phantom, but it is still effective around 1 cm away in both directions. To analyze the behavior of the resonator in phantom, we need to sweep the flip angle and record the maximum intensity level, presented in Figure 5.26.



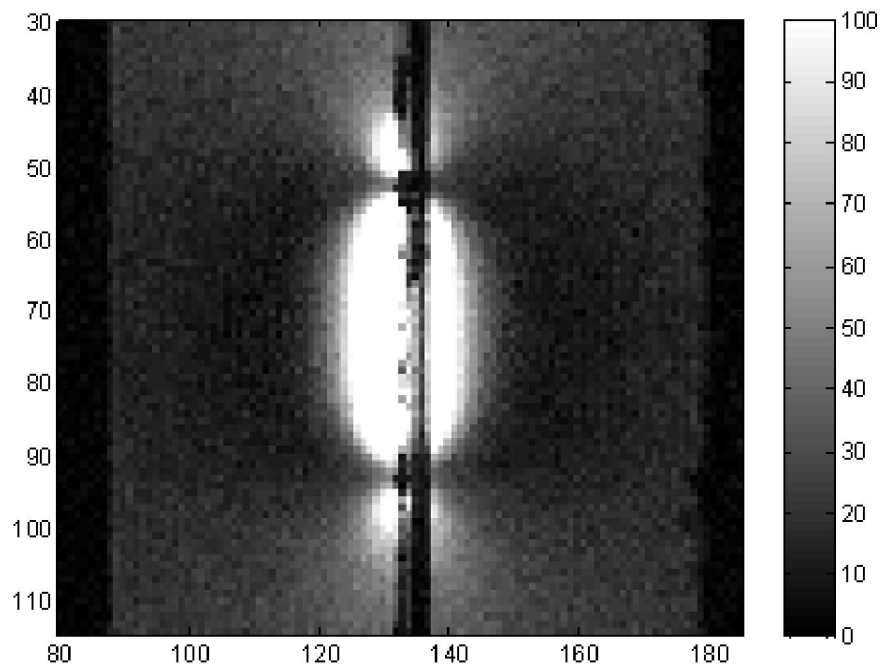
**Figure 5.26** Characteristic of rigid resonator due to different flip angles.

Figure 5.26 shows the relationship between the intensity level and the flip angle excitation with and without the resonator. Using the Ernst angle calculation, the maximum magnetization occurs around  $39^\circ$ , which is already much smaller than the maximum intensity of the resonator for any flip angle excitation. It is clear that the enhancement in the signal because of the resonator is larger for lower flip angles and it decreases as the flip angle increases as shown in Figure 5.32. Here decoupling of the resonator, due to the inductive coupling to the transmitting antennas, is necessary to prevent the previously seen artifacts.

### 5.3.3 Phantom Imaging Using Novel Flexible Resonators

#### 5.3.3.1 Planar Imaging with the Flexible Resonators

The flexible resonator offers attractive properties even for planar configuration. Although it has imaging artifacts (due to inductive coupling), this concern is not studied for these initial designs. Figure 5.27 shows an MRI of a flexible resonator in planar configuration, which was received inside the same phantom as the previous images.



**Figure 5.27 MRI of the novel resonator structure on a flexible substrate for 5° flip angle (planar configuration).**

Here the noise level and the phantom intensity levels are 8 and 28 respectively. The distance of 2-fold amplification is 6 mm in both directions, giving a total of 12 mm. The maximum intensity level using the flexible resonator is around 620, which is 2 times of the rigid one. This structure has imaging artifacts due to flip angle amplification of the resonating structure inside the phantom. Figures 5.28-5.31 show the MRI of the flexible structure in planar configuration at different flip angles.

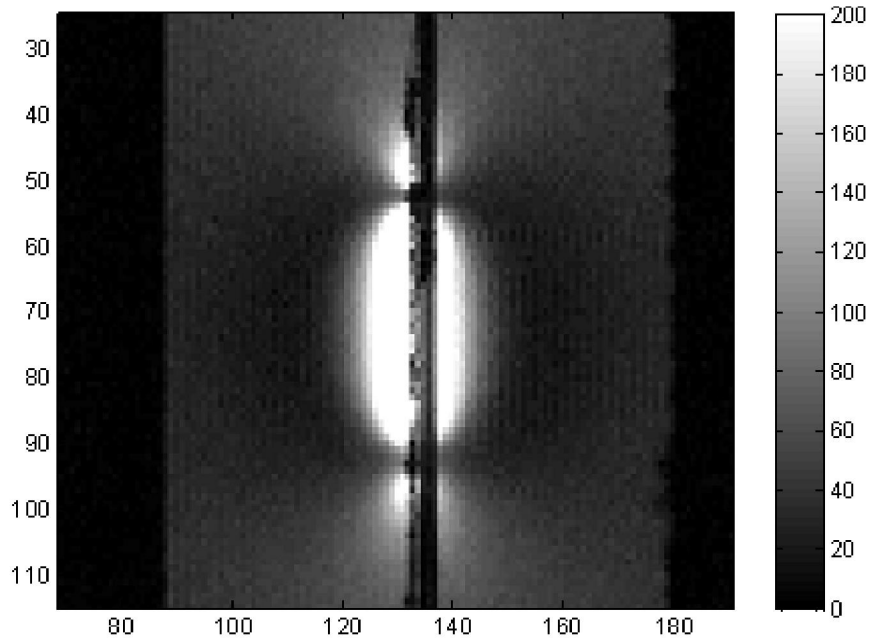


**Figure 5.28 MRI of the novel resonator structure on a flexible substrate for  $10^\circ$  flip angle (in planar configuration).**

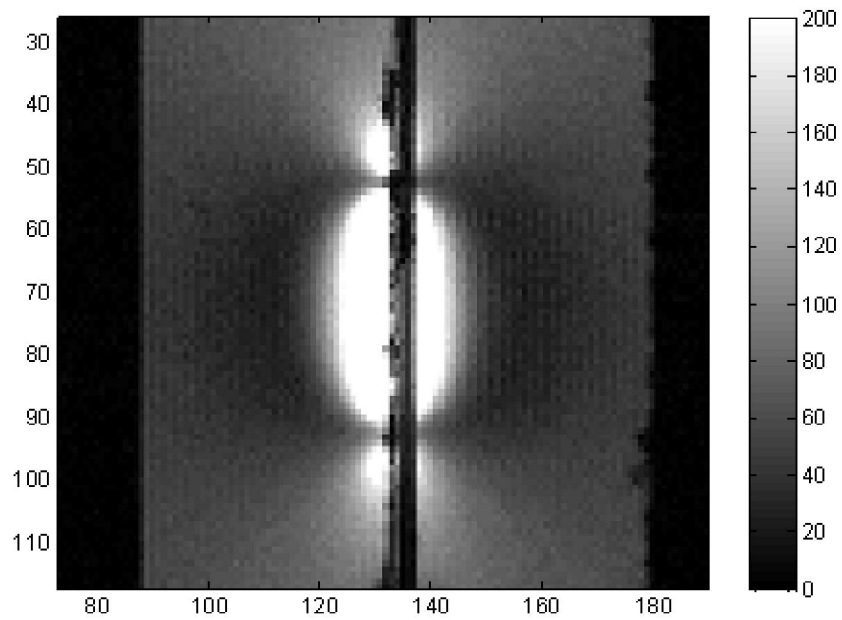


**Figure 5.29 MRI of the novel resonator structure on a flexible substrate for  $15^\circ$  flip angle (in planar configuration).**

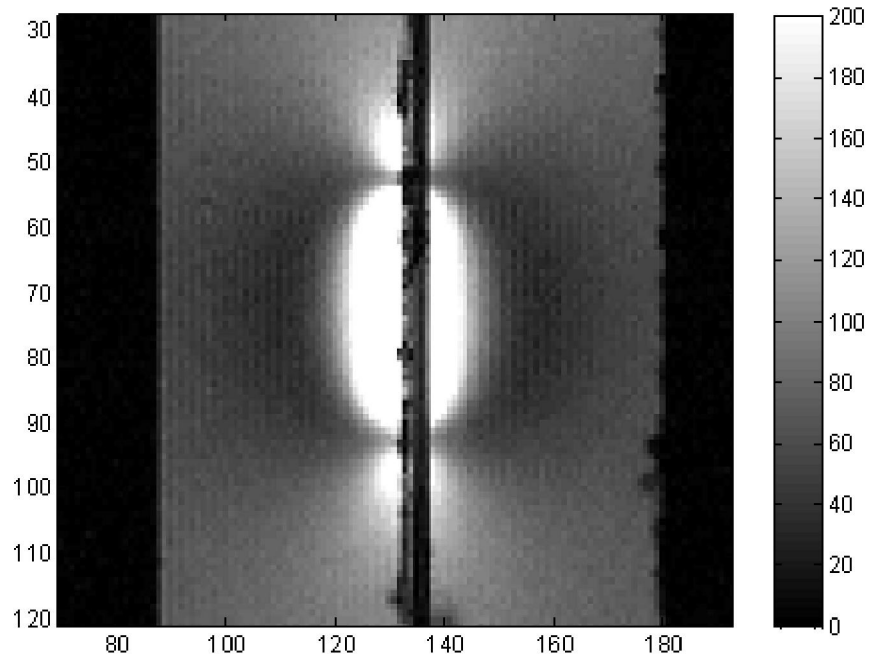


**Figure 5.30 MRI of the novel resonator structure on a flexible substrate for 20° flip angle (in planar configuration).**

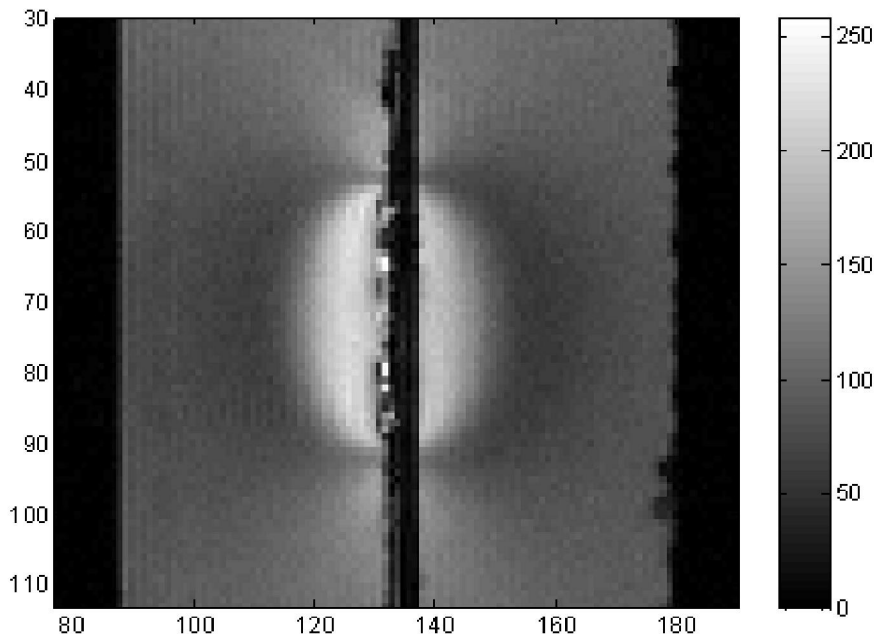


**Figure 5.31 MRI of the novel resonator structure on a flexible substrate for 45° flip angle (in planar configuration).**

The distance of 2-fold amplification is always more than 6 mm in both directions, which makes 12 mm in total, for any flip angle distribution smaller than 25°. Conventional methods generally use flip angles less than 30° and do not exceed 45°. Flip angle characteristics of the flexible resonator, together with that of the rigid one is given in Figure 5.32. The enhancement factor and the enhancement limit for both the rigid and the flexible resonators are given in Figures 5.33 and 5.34, respectively.

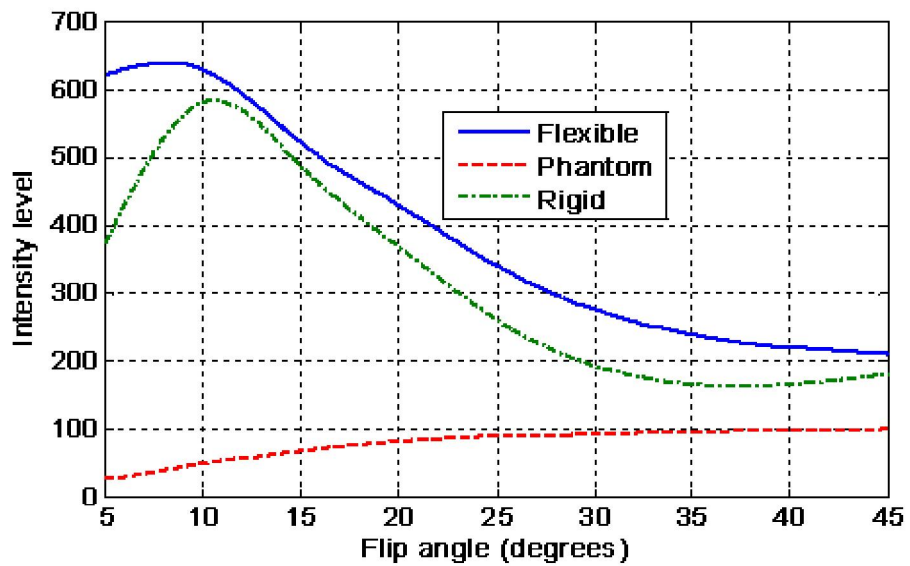


Figure 5.32 Comparison of the flexible and rigid resonators for different flip angles.

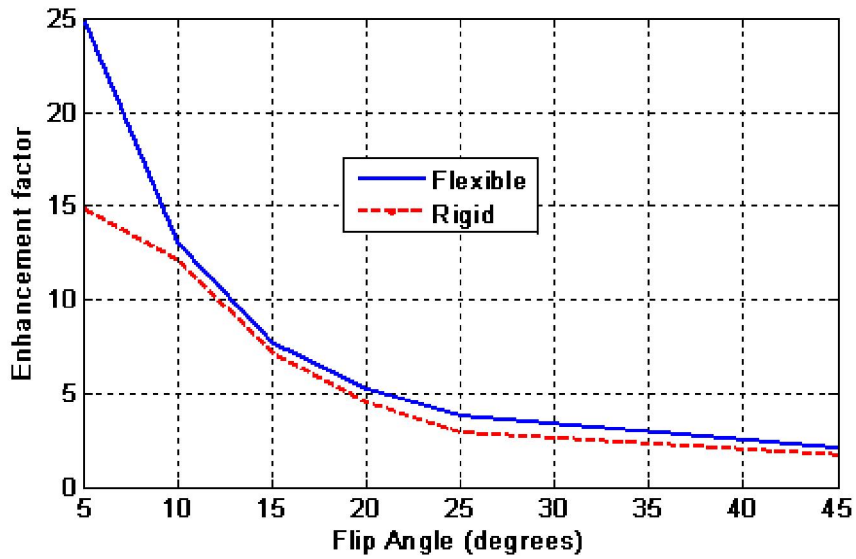


Figure 5.33 Enhancement factor of the resonators for different flip angles.

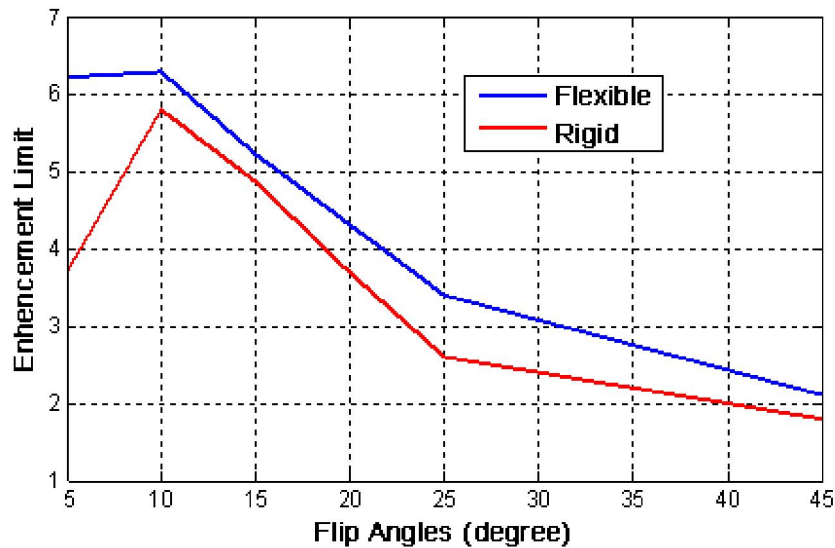


Figure 5.34 Enhancement limit for internal planar imaging due to different flip angles.

The flexible resonator is working the best with the lower flip angles. It seems it is more effective at smaller flip angles but we have to be careful about the physics of the system. Here, its thinner isolation layer allows spin to be affected more than the rigid case, which is mostly effective at the lower flip angles. This effect is strong in the proximity. The maximum field level analysis of this structure with such a thin isolation layer should not be misleading. Physics of the system and imaging area should always also be considered.

### 5.3.3.2 Nonplanar Imaging with the Flexible Resonators Having Different Curvatures

Changing the size of loop definitely changes its inductance and thus, shifts its resonance frequency. From classical electromagnetic theory, it is well known that the bending of a loop will decrease its inductance and hence, increases its resonance frequency. On the other hand, loading of a loop with a medium with a higher relative dielectric permittivity also increases the self-capacitance of the metallic lines, which results in lower resonance frequency. For our flexible resonator structure, the frequency shift due to loading is around 8 MHz in planar configuration. To match the resonance frequency of 123 MHz in phantom, which is the characteristic frequency of the 3 T scanner at UMRAM, we tuned the flexible resonator to 125 MHz, which will be decreased to 117 MHz when loaded with phantom, and will then be increased to 123 MHz by bending it. It is almost impossible in practice to be fair in bending and adjusting the resonance frequency of different samples to the same level. Here we study the effect of bending on resonance frequency shift. For lower bending ratios, the curvature coefficient is smaller and, resultantly, the resonance frequency shift is smaller than that for the higher curvature ratios, as given in Equation (5.4)

$$\rho = \frac{1}{R} \quad (5.4)$$

where  $\rho$  is the curvature coefficient and the R is the curvature radius as shown in Figure 5.35.

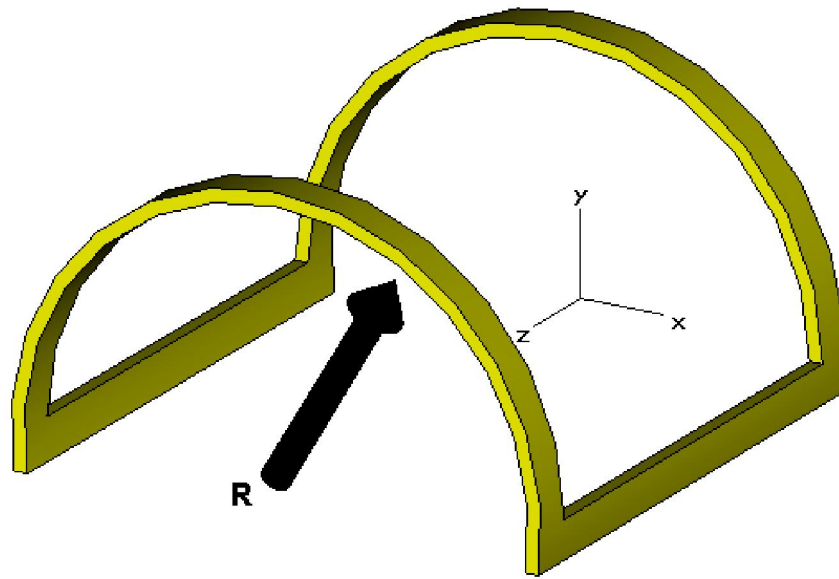


**Figure 5.35 Sketch of the flexible resonator.**

The flexible structure can be bent from any line and in any directions. To keep the bending simple, we choose the configuration given in Figure 5.35. The first curvature radius is used at  $R=12$  mm, with a curvature of  $\kappa = 83.3 \text{ m}^{-1}$  and central angle of  $\theta = 0.584$  rad, with a corresponding cross-section illustrated in Figure 5.36. MRIs of the flexible resonator in this configuration in phantom are shown for different flip angles in Figures 5.37-5.41.

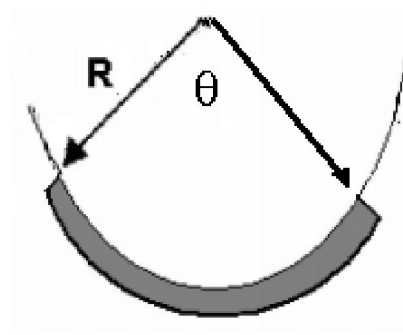


**Figure 5.36 Side view of the bent resonator.**

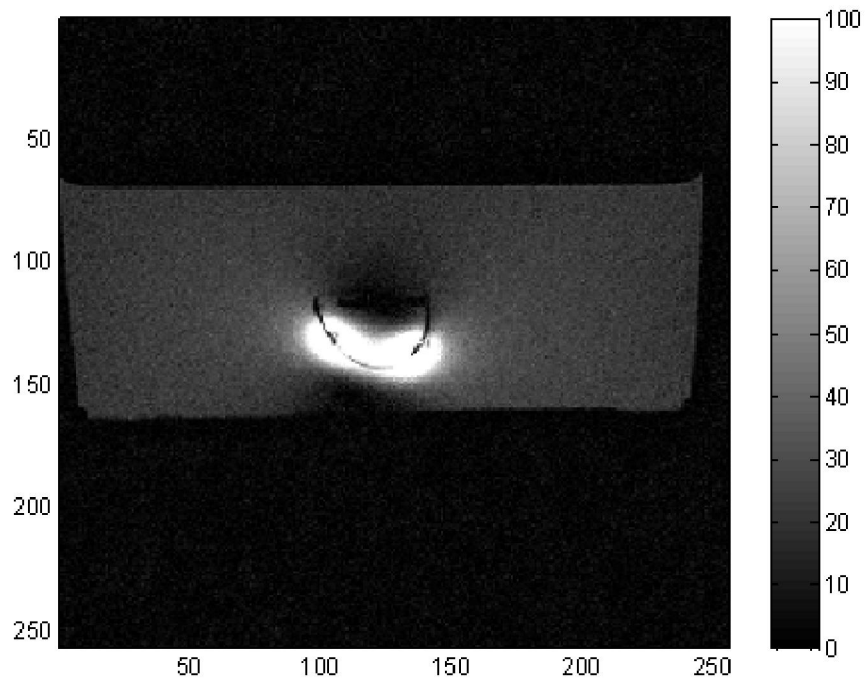


Figure 5.37 MRI of the bent resonator for 5° flip angle (in nonplanar configuration).

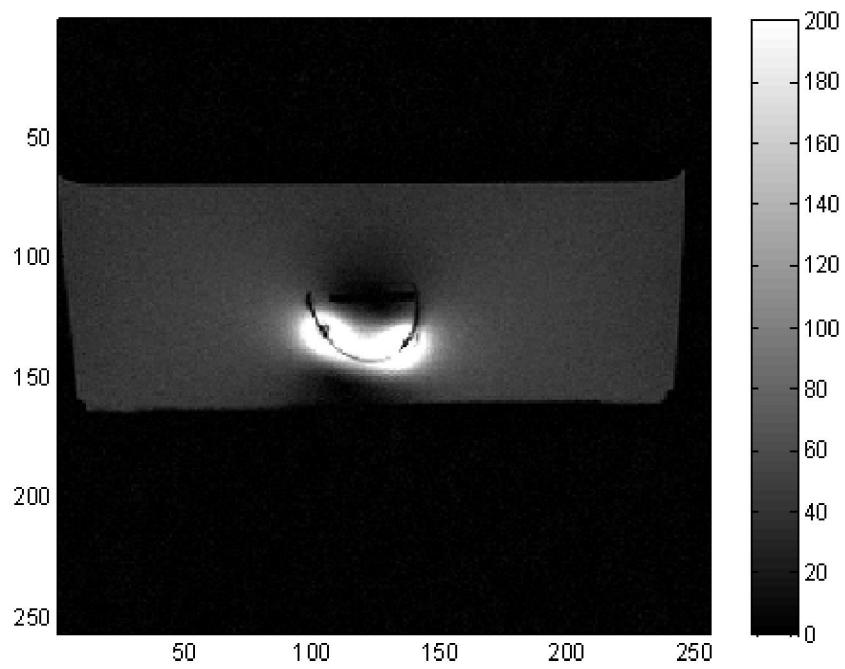
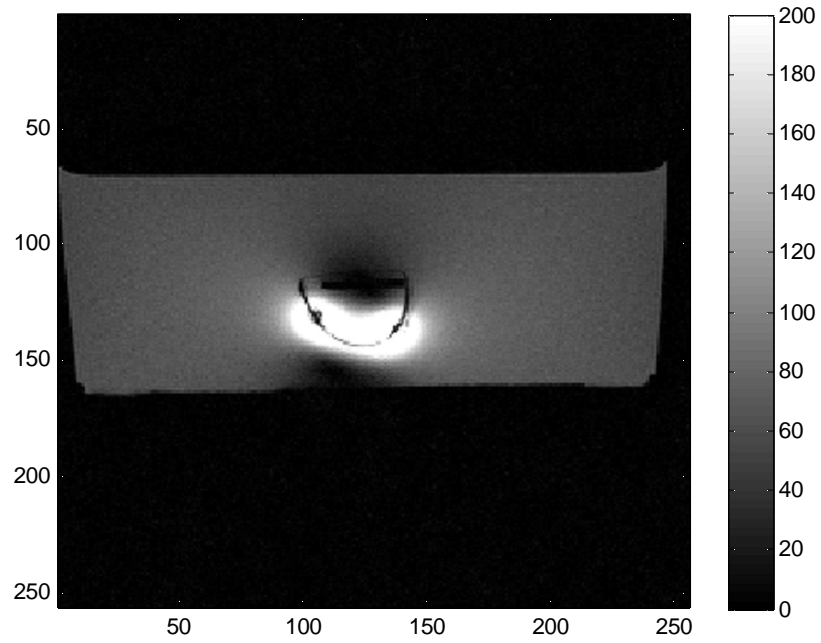
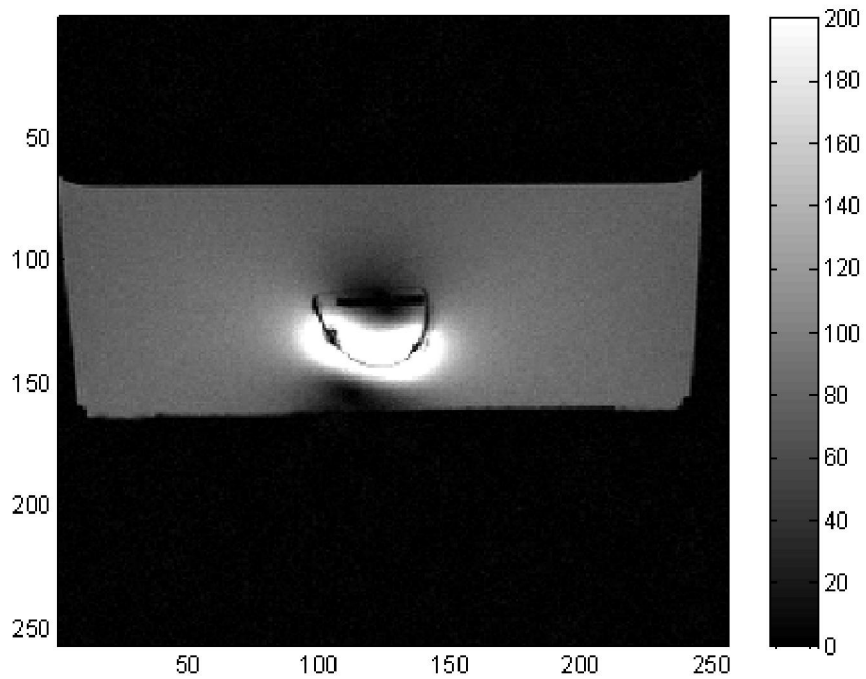


Figure 5.38 MRI of the bent resonator for 10° flip angle (in nonplanar configuration).



**Figure 5.39 MRI of the bent resonator for 15° flip angle (in nonplanar configuration).**



**Figure 5.40 MRI of the bent resonator for 20° flip angle (in nonplanar configuration).**

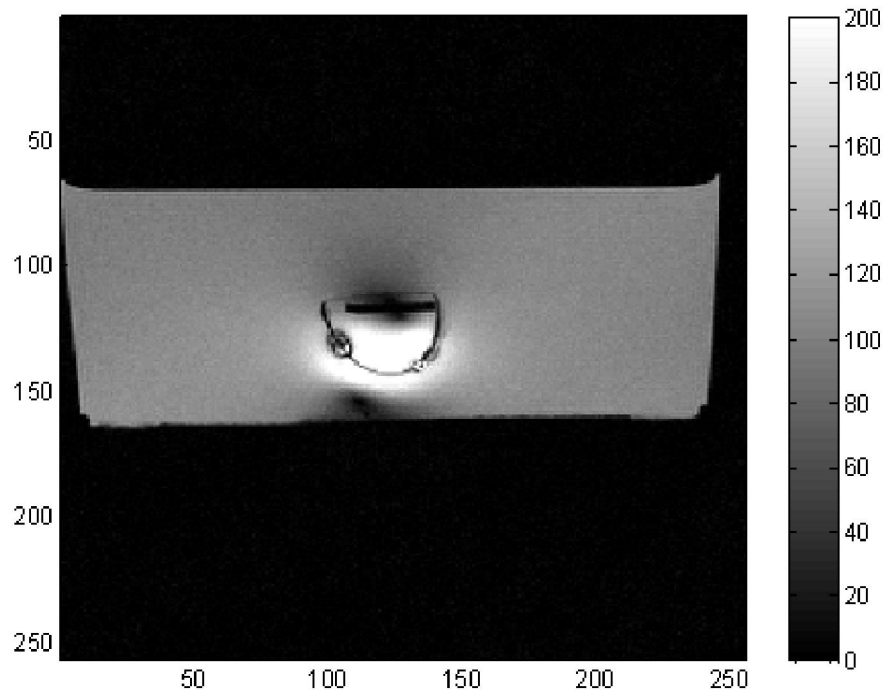


**Figure 5.41 MRI of the bent resonator for 45° flip angle (in nonplanar configuration).**

It is clear that the pattern of the flexible resonator structure is not strictly dependent on the flip angle as in the previous cases. Imaging artifacts still exist due to the inductive coupling of the resonator to the transmitter antennas and flip angle distributions. The distance of 2-fold amplification is around 10 mm inside the bent geometry and 5 mm away from both sides of the structure outside. This tells us that the bending would result in higher field amplification in internal regions and homogenization of the internal fields might be achieved by proper designs. The analysis of the maximum intensity as a function of the excitation flip angle is given in Figure 5.42.

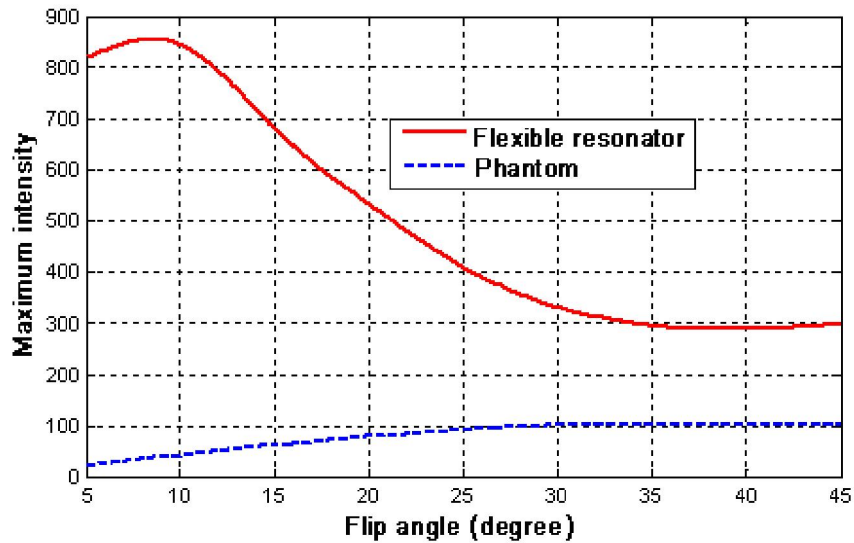


Figure 5.42 Maximum intensity characteristics of the bent resonator for different flip angles (in nonplanar configuration).

This clearly shows that the intensity of the phantom is amplified by at least 3 times at higher flip angles and almost 40 times for the best case around flip angle of 5° as in Figure 5.43.

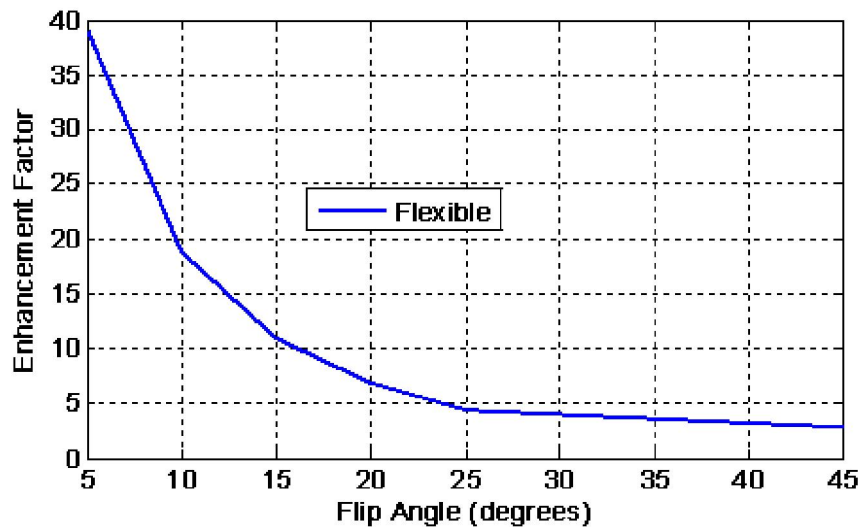
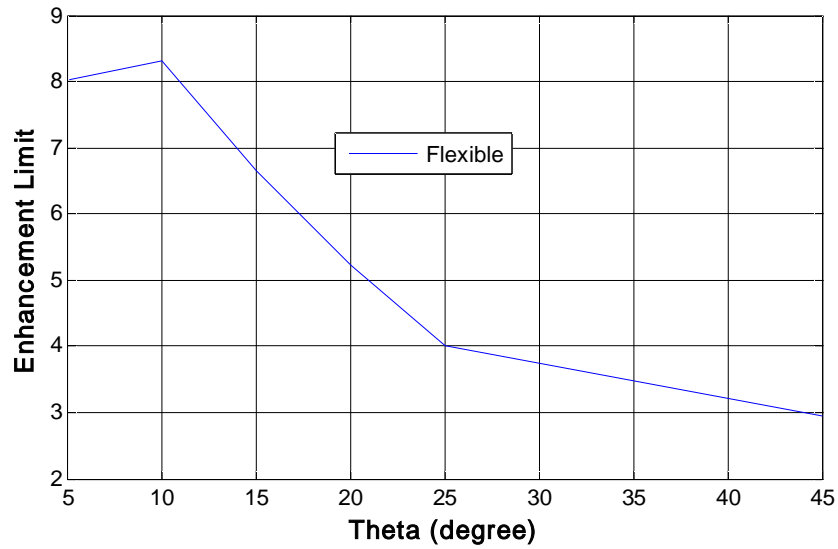


Figure 5.43 Enhancement factor of the bent structure with a curvature of 83.3 m<sup>-1</sup>(in nonplanar configuration).

The flexible resonator is working best with the flip angles smaller than  $10^\circ$  in this non-planar configuration of  $\kappa = 83.3 \text{ m}^{-1}$ . Its enhancement limit is depicted in Figure 5.44.



**Figure 5. 44 Enhancement limit of the bent structure with a curvature of  $83.3 \text{ m}^{-1}$  (in nonplanar configuration).**

Furthermore, to understand the characteristics of the flexible resonator for different curvatures and bending directions, we also changed the bending radius to  $R=6 \text{ mm}$ , corresponding to curvature of  $\kappa = 166.7 \text{ m}^{-1}$ , as sketched in Figure 5.45.

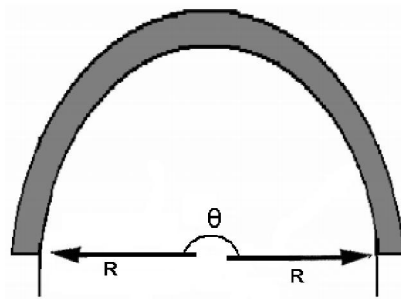


**Figure 5.45 Side view of the flipped and bent resonator.**

Now the resonator completely covers the upper semi-circle of the layout with the central angle of  $\theta = 1.17 \text{ rad}$ , and to understand its low flip angle behavior, we performed the experiments starting from  $1^\circ$  as given in Figures 5.46-5.55.

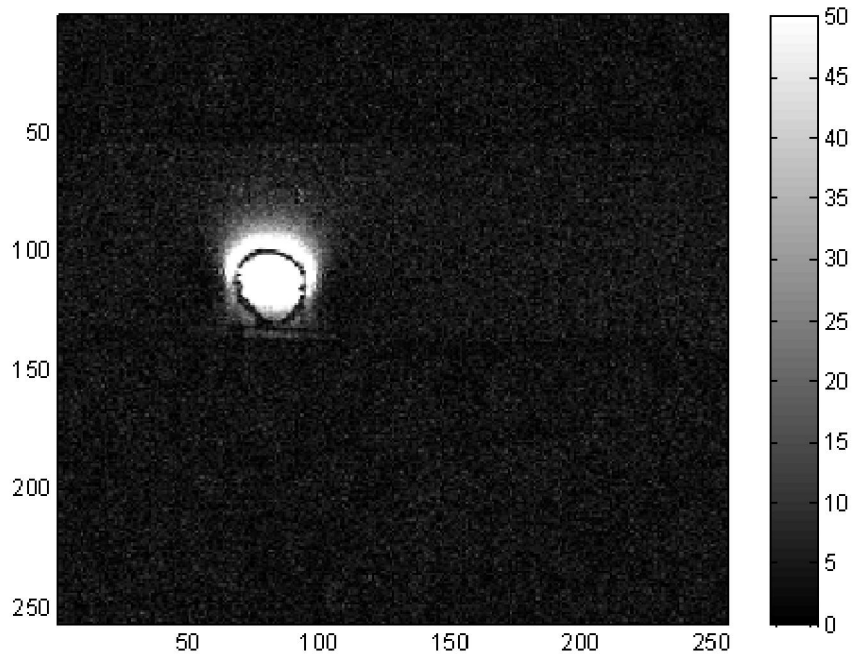


**Figure 5.46 MRI of the flipped and bent resonator for  $1^\circ$  flip angle (in nonplanar flipped configuration).**

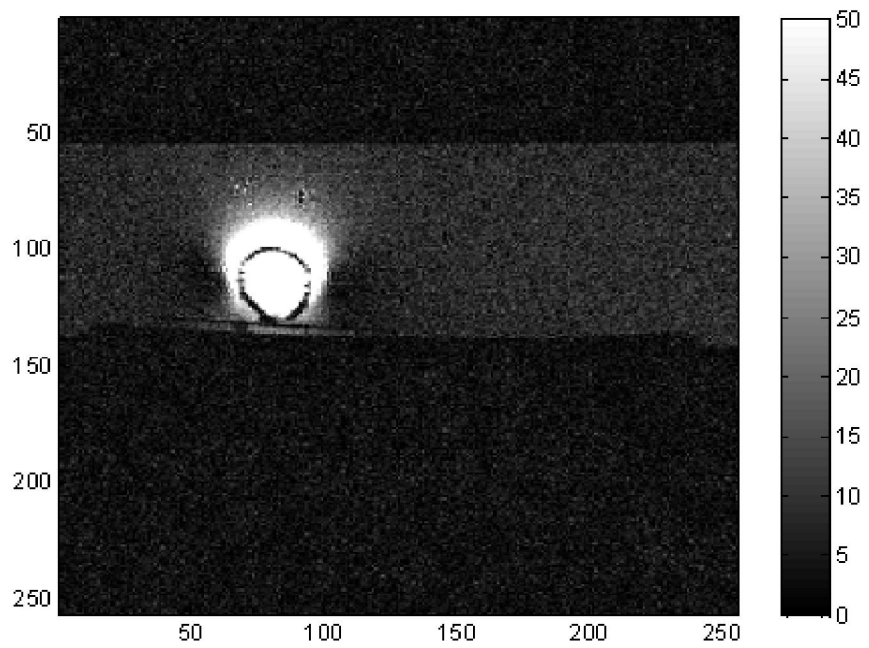


**Figure 5.47 MRI of the flipped and bent resonator for  $2^\circ$  flip angle (in nonplanar flipped configuration).**

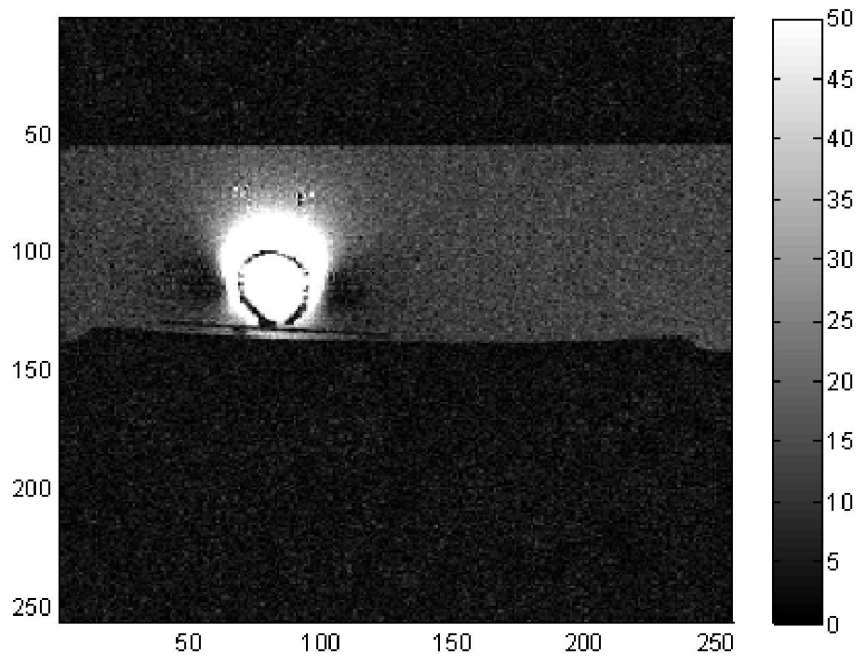


**Figure 5.48 MRI of the flipped and bent resonator for 3° flip angle (in nonplanar flipped configuration).**

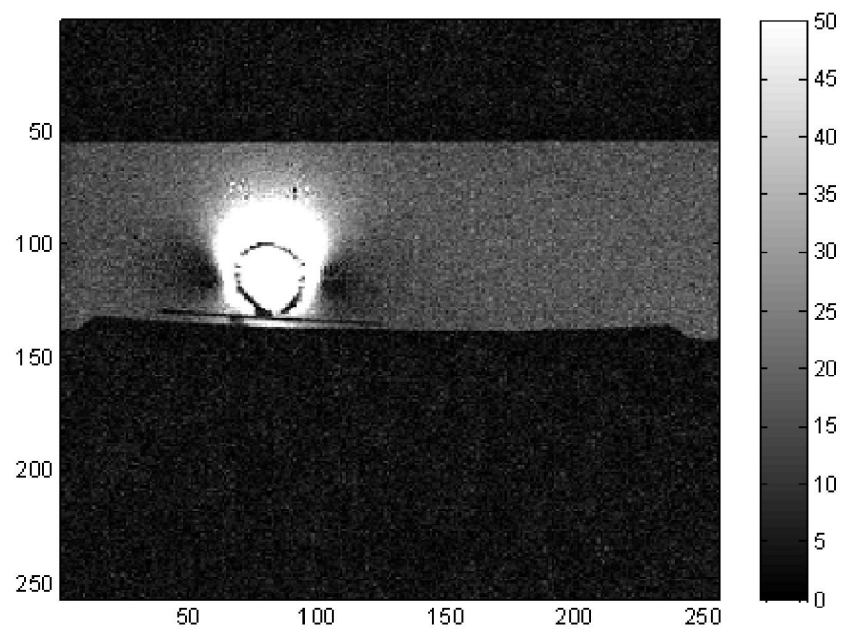


**Figure 5.49 MRI of the flipped and bent resonator for 4° flip angle (in nonplanar flipped configuration).**

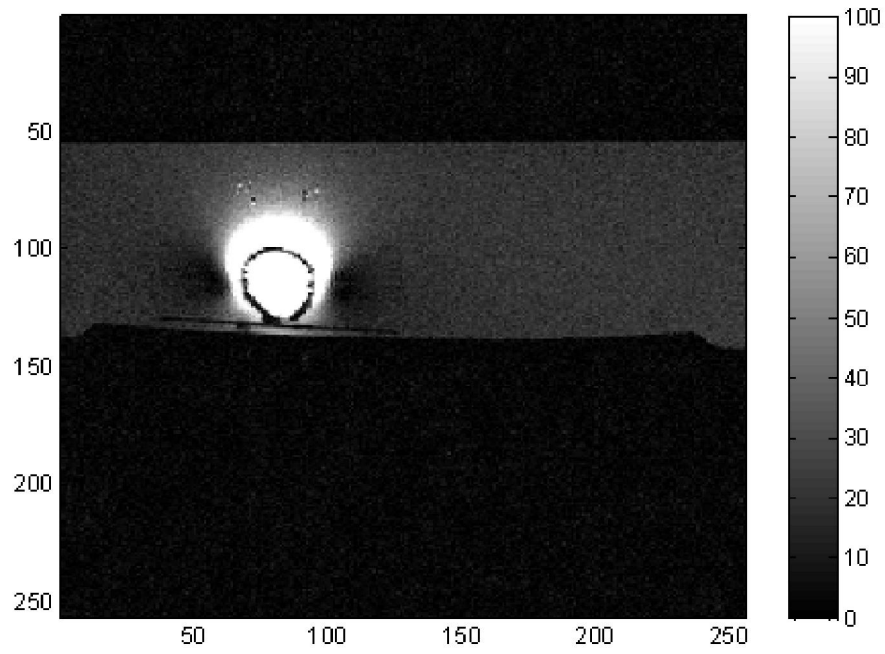


**Figure 5.50 MRI of the flipped and bent resonator for 5° flip angle (in nonplanar flipped configuration).**

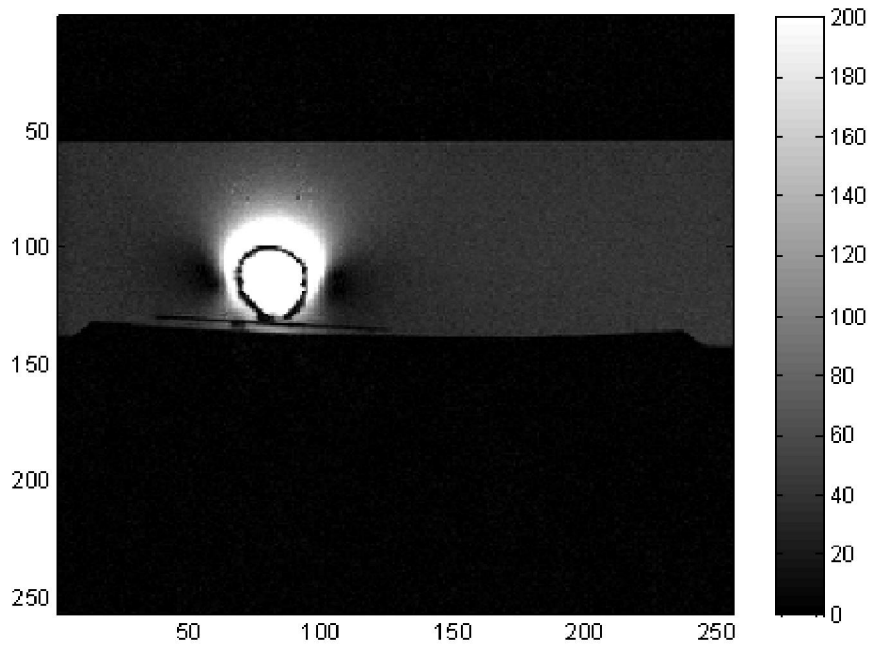


**Figure 5.51 MRI of the flipped and bent resonator for 10° flip angle (in nonplanar flipped configuration).**

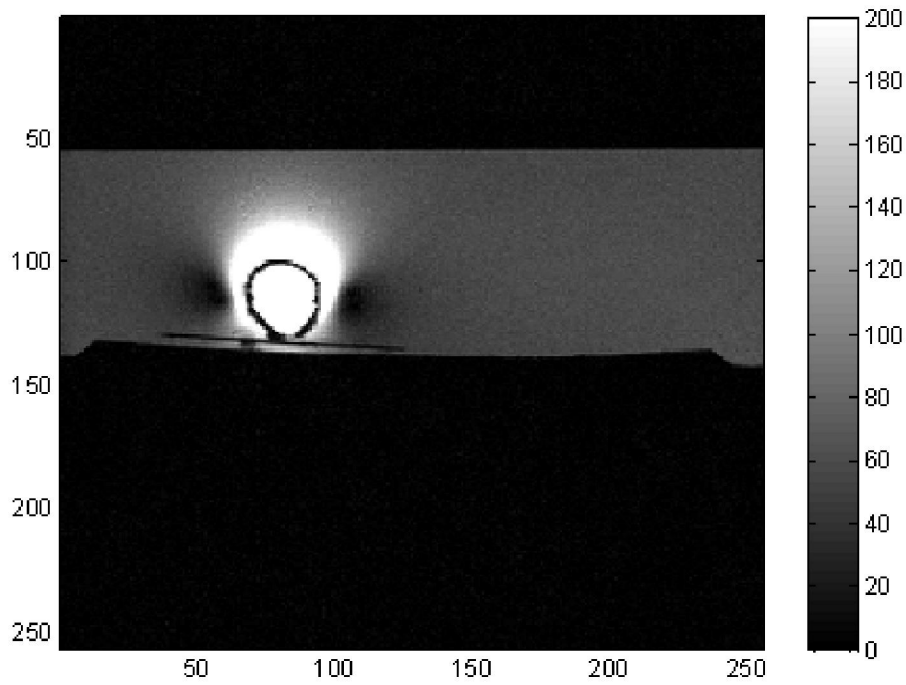


**Figure 5.52 MRI of the flipped and bent resonator for 15° flip angle (in nonplanar flipped configuration).**

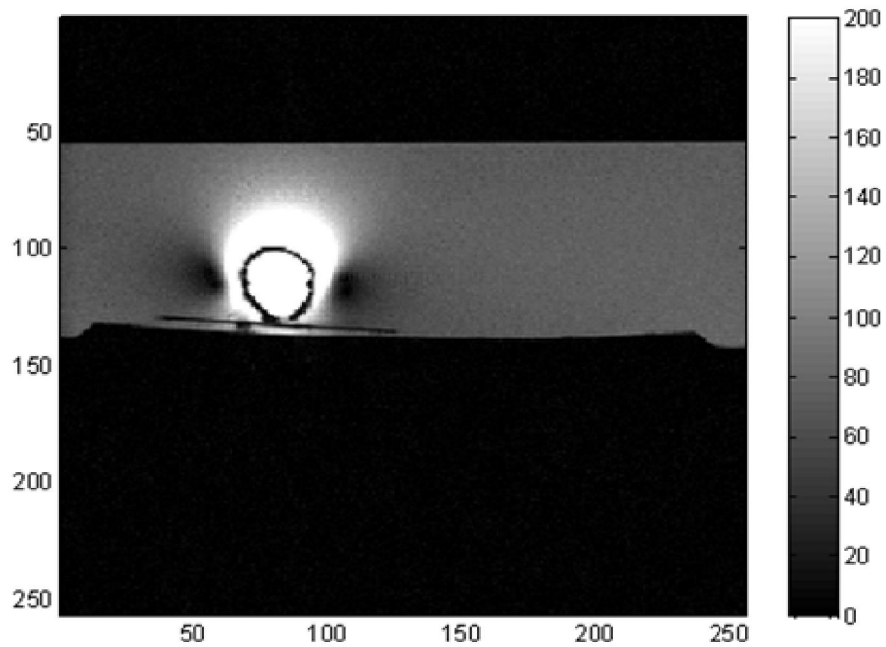


**Figure 5.53 MRI of the flipped and bent resonator for 20° flip angle (in nonplanar flipped configuration).**

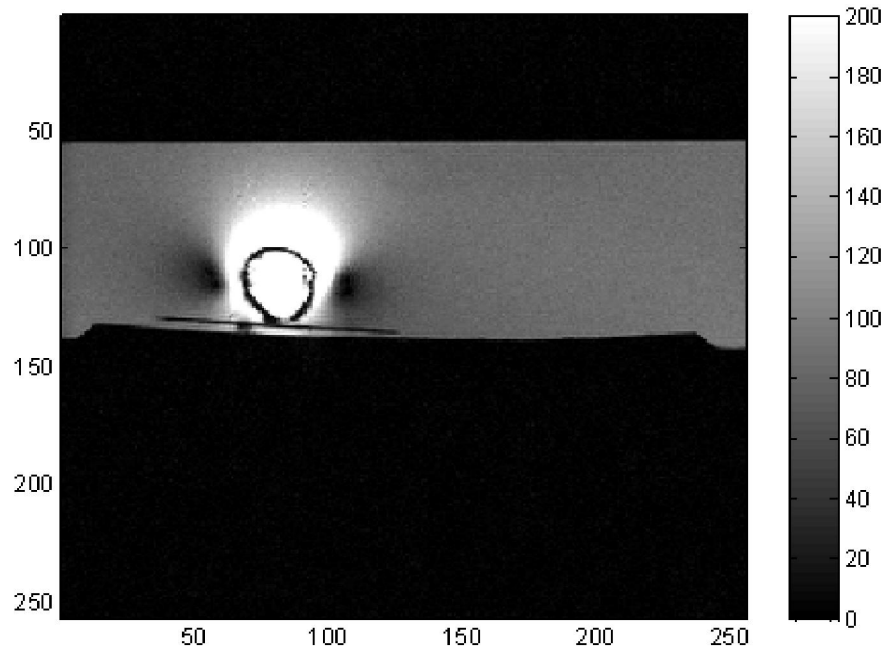


**Figure 5.54** MRI of the flipped and bent resonator for  $25^\circ$  flip angle (in nonplanar flipped configuration).

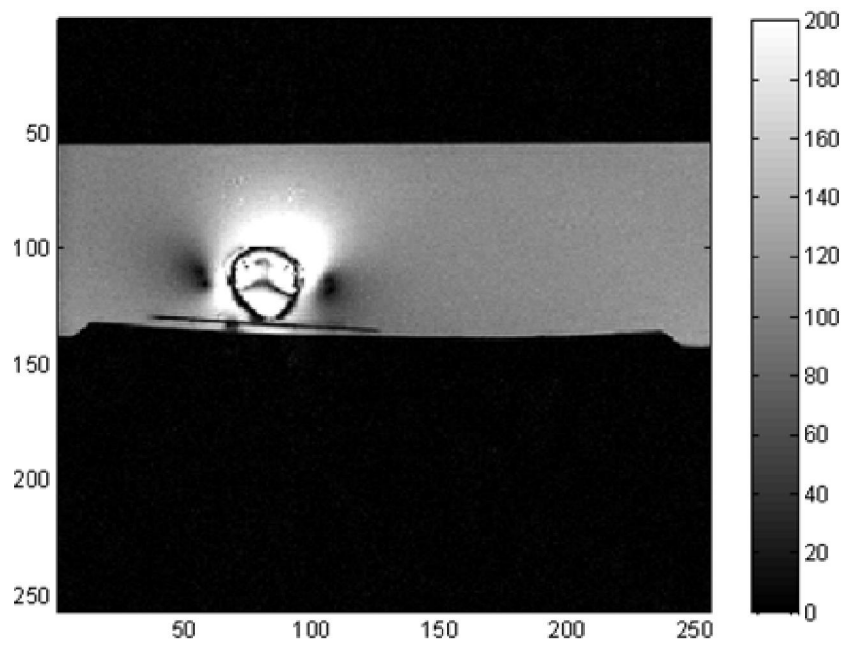


**Figure 5.55** MRI of the flipped and bent resonator for  $45^\circ$  flip angle (in nonplanar flipped configuration).

As clearly seen from these figures, the noise level is very dominant on the phantom up to 5° of excitation and the resonator is working the best around these angles. Further increasing the flip angle improves SNR in general but not as much as the resonator can do. Another point is the image amplification area of the resonator. For the flip angles smaller than 25°, the distance of the 2-fold amplification in the vertical direction is more than 10 mm outside and around 20 mm inside. Although the resonator does not cover the complete cylindrical surface in this experiment, it can amplify across the entire area. For higher flip angles, imaging artifacts become significant inside the structure, which also supports the observation that this resonator works the best for the lower flip angles. The artifacts in the horizontal direction are due to the longitudinal metallic lines of the resonator. The flip angle characteristic of the flipped and bent resonator is depicted in Figure 5.56.

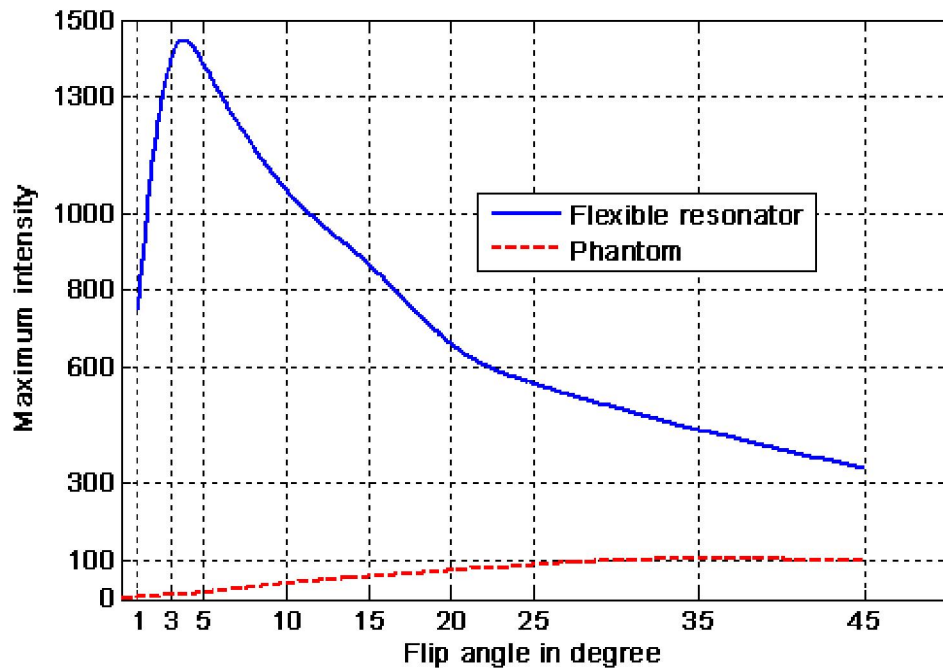


Figure 5.56 Characteristic of bent resonator due to different flip angles.

This flexible structure resonates around 123 MHz in phantom and exhibits maximum intensity amplification ratios ranging from 150 to 3 for the flip angles of 3° - 45° as given in Figure 5.57.

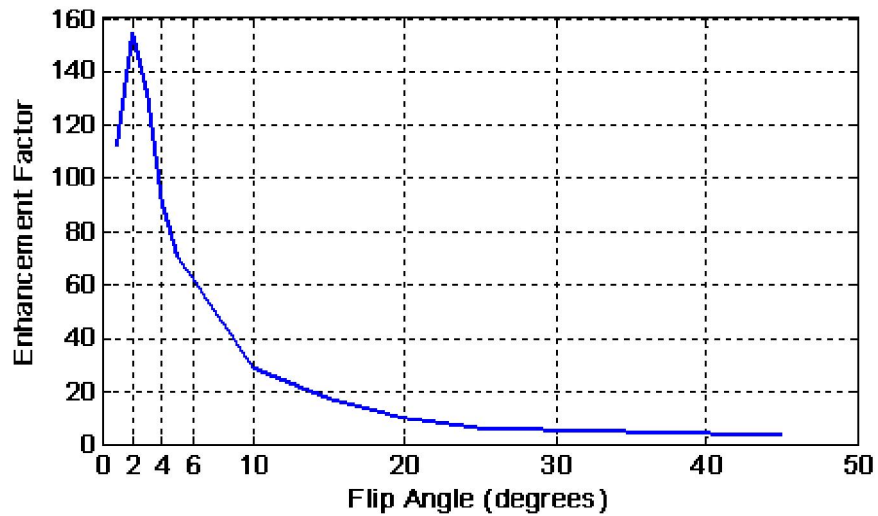


Figure 5.57 Enhancement factor of the bent structure with a curvature of  $166.7 \text{ m}^{-1}$  (in nonplanar configuration).

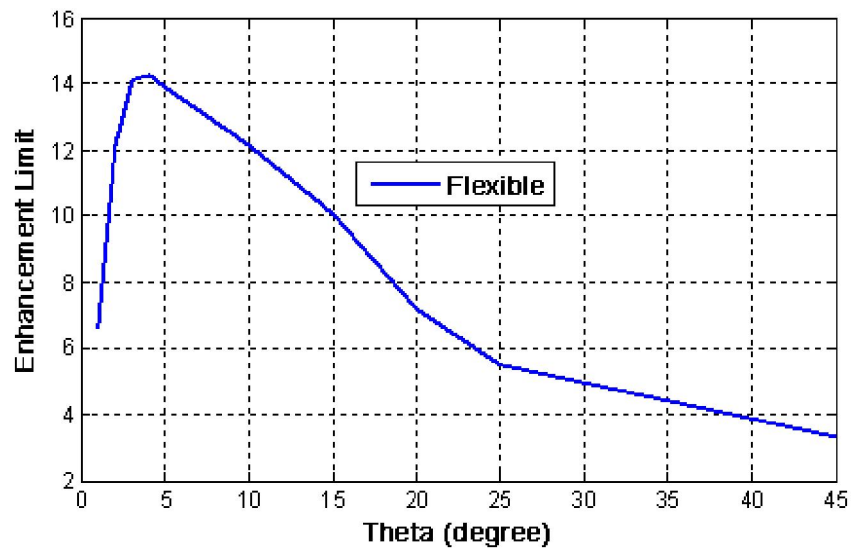


Figure 5.58 Enhancement limit of the bent structure with a curvature of  $166.7 \text{ m}^{-1}$  (in nonplanar configuration).

Figure 5.58 shows the enhancement limit of the structure for various flip angles. This resonator structure, with a full coverage of the continuous cylindrical area when flipped and bent at  $=166.7 \text{ m}^{-1}$ , enhances the internal field with a factor of more than 150 times, which increases the resolution more than 12 times under the same RF power.

# CHAPTER 6

## CONCLUSIONS AND FUTURE WORK

In this thesis, we have proposed and demonstrated implantable, MRI-compatible, local resonators that can be fabricated both on rigid and flexible substrates for imaging planar and nonplanar surfaces by using the idea of distributive loading. Conventional capacitors are too bulky to tune a resonator for permanent implants and not biocompatible to be used even for temporary implants. It is possible to coat them with biocompatible materials, but this further enlarges the dimensions of the capacitor. All of these handicaps, together with the high quality factor that can be achieved by the proposed novel resonator structures, point out that such implantable, chip-size resonators offer an enabling technology for future MRI implants.

Thin film loading is a known phenomenon used in active catheter guiding systems in MRI but is not sufficient to satisfy the needs of permanent implants to stay inside the body for years. Unused areas due to these capacitive regions and the bending difficulties of these plates prevent them from being used as implantable resonators both for in-vivo and ex-vivo applications. Isolation of these regions will also increase their dimensions, which again hinders their use as the permanent implants.

The resonator designs proposed in this thesis enable a high field confinement inside the capacitive region, which is distributed along its own conducting plates, and the first order isolation of electric field confinement is achieved with these metallic plates. This confinement inside the metallic layer allows these resonators to achieve higher quality factors even with a thinner isolation layers.

Biocompatibility of these resonator chips is satisfied by using gold as the metallic lines and the silicon or polyimide as the substrate. Also, it is the best to use nitrides as the dielectric layers in these designs. Although it was suggested

that some types of photoresists are also biocompatible and can be used for permanent implants they are not guaranteed for long-term use unlike nitrides.

Bending of these distributively loaded flexible resonator structures does not damage their resonance quality due to the capacitive region deformation unlike conventional thin film loading. The conventional thin film loaded architecture has a lumped capacitive region at a single place connected to the inductive part and is strongly affected from the deformation. However, the distributive loading of the proposed resonators helps to tolerate these bending effects. This can be understood by considering the series connection of the capacitors, which have an equivalent capacitance and the equivalent capacitance is insensitive to the change in one capacitor.

Coverage of the nonplanar surfaces is another property of the distributively loaded flexible resonator structures. They can work as a wearable antenna of a specific shape, which is designed specifically to work with its load in the targeted configuration. It would be possible to design and tune the distributively loaded flexible resonator that completely works for a given implant in principle (e.g. for subdural electrodes before epilepsy surgery).

The field patterns of the proposed resonator structure show that the field amplification is higher inside of the bent resonator and can be modified by shape and the bending of the resonator. For example, it can be rectangular, circular, or any other fantastic shape as shown in Figure 6.1 for the sake of demonstration.

Figure 6.1 supports the idea that the resonators can be designed in any shape of closed loops. Their intensity patterns will be significantly different; however, their performance in MRI can be strongly dependent on the flip angle and should be studied carefully for the targeted implant application.

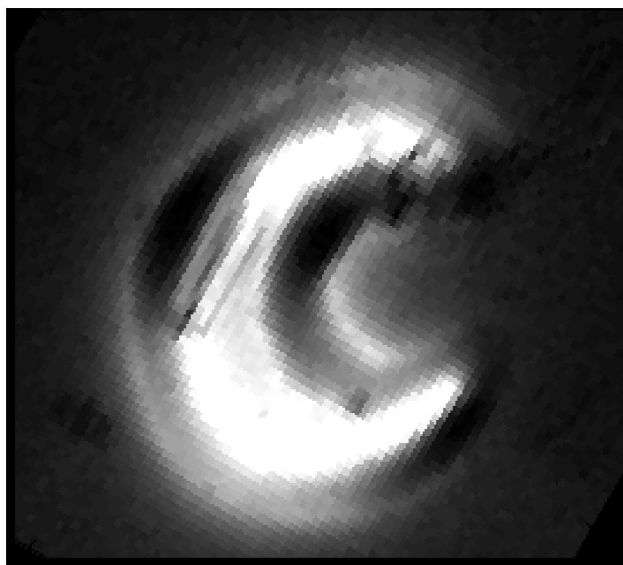


**Figure 6.1 A novel flexible resonator designed in the shape of a crescent moon for MR imaging.**

It should be also noted that all of these benefits come at a cost. Since the resonator structure has the self-resonating property, it cannot be easily modified once fabricated unless additional tuning mechanisms are utilized. This may not be a problem for a permanent implant, but could become an issue in the long-term use, e.g., due to the tissue modifications in the body, if not considered and addressed. Therefore, it is necessary to study this kind of aftermath effects.

Locally resonating structures do not have higher resistance, thus they are not supposed to cause tissue heating due to their resistive losses. The more effective reason for tissue heating is the eddy currents near the metallic structures due to the wider skin depth of the tissues. For example, for blood, skin depth is around 5 mm at 123 MHz, where the induced currents cannot penetrate through the tissue and causes non-radiating Eddy currents to heat up the tissues. The temperature characteristics and MRI safety of these distributively loaded structures, which will definitely contribute to the Eddy currents, should be studied carefully.

Another consideration is the frequency shift of the resonator structure due to the loading. As we mentioned in the circuit equivalent model, each section of the

unit cell is loaded with the body, thus leading to an increase in the capacitance with the same ratio. The loading of the capacitive layer needs to be handled carefully and will be one of the topics of our future work given a specific implant. Different connection of capacitive layers may offer freedom to deal with loading, which however comes at a cost of fabrication complexity.

Imaging artifacts of the proposed resonator is another drawback. It is a conventional problem and possible solutions differ from each other depending on the approach to take. For example modification of the sequence parameters allows one to deal with these non-uniformities, but this is not a convenient way to solve this problem. Hardware solutions typically needs schottky diodes, which uncouple the resonator from transmitting antennas and eliminate the flip angle enhancement factor for lower excitation angles. This would be better for larger flip angles, but would severely decrease the amplification at an order of magnitude for smaller angles [40]. This can be acceptable in certain applications but does not offer a satisfactory solution for all cases. To date, there is no other solution proposed to address this problem in the literature. This will be one of the future works of this research to solve these problems.

# BIBLIOGRAPHY

---

- [1] F. Bloch, W. W. Hansen, and M. Packard, “Nuclear Induction”, *Physical Review Letters*, 69, 127 (1946)
- [2] E. M. Purcell, H. C. Torrey and R. V. Pound, “Resonance Absorption by Nuclear Magnetic Moments in a Solid”, *Physical Review Letters*, 69 37 (1946)
- [3] “Nobel Prize for Physics, 1952”, *Nature* **170**, 911-912 (29 November 1952)
- [4] E. Abaci, “Analysis of the Electromagnetic Fields Inside the Gradient Coils and Investigation of Nerve and Cardiac Stimulation Risk for the Patients During MRI”, MS. Thesis, July 2008
- [5] E. Asano, C. Juhasz, A. Shah, S. Sood, and H. T. Chugani, “Role of subdural electrocorticography in prediction of long-term seizure outcome in epilepsy surgery”, *Brain, A journal of neurology*, 2009: 132, 1038-1047
- [6] National Magnetic Resonance Research center, <http://umram.bilkent.edu.tr/>
- [7] D. G. Nishimura. “Principles of Magnetic Resonance Imaging”, 1996
- [8] G. J. Stanisz, E. E. Odobina, J. Pun, R. M. Henkelman, “T1, T2 Relaxation and Magnetization Transfer in Tissue at 3T”, *Magnetic Resonance in Medicine* 54:507–512 (2005)
- [9] P. C. Lauterbur, “Image Formation by Induced Local Interactions: Examples Employing Nuclear Magnetic Resonance”, *Nature* 242, 190 - 191 (16 March 1973)
- [10] Filler, AG, “The history, development, and impact of computed imaging in neurological diagnosis and neurosurgery: CT, MRI, DTI”, *Nature Proceedings*

- 
- [11] L. Wen-Tao, Z. Dong-Lin, and T. Xin, "A novel approach to designing cylindrical-surface shim coils for a superconducting magnet of magnetic resonance imaging", *Chin. Phys. B* Vol. 19, No. 1 (2010) 018701
- [12] J. M. Jin, "Electromagnetic Analysis and Design in Magnetic Resonance Imaging", CRC Press 1996
- [13] K. Chang, "Microwave Ring Circuits and Antennas", Wiley Series in Microwave and Optical Engineering, 1996
- [14] F. E. Terman, "Radio Engineers' Handbook", Mc-Graw Hill, 1943
- [15] J. J. Carr, J. M. Brown, "Introduction to Biomedical Equipment Technology", Prentice Hall, 2001
- [16] R. Melik, N. K. Perkgoz, E. Unal, C. Puttlitz and H. V. Demir, "Bio-implantable passive on-chip RF-MEMS strain sensing resonators for orthopedic applications", *Journal of Micromechanics and Microengineering*, 18 (2008), 115017
- [17] R. Melik and H. V. Demir, "Implementation of High Quality-Factor on-Chip Tuned Microwave Resonators at 7 GHz", *Microwave and Optical technology Letters*, Vol. 51, No. 2, February 2009
- [18] R. Melik, E. Unal, N. K. Perkgoz, C. Puttlitz and H. V. Demir, "Metamaterial-Based Wireless Strain Sensors", *Applied Physics Letters*, 95, 011106, 2009
- [19] R. Melik, E. Unal, N. K. Perkgoz, C. Puttlitz and H. V. Demir, "Flexible Metamaterials for Wireless Strain Sensing", *Applied Physics Letters* 95, 181105, 2009

- 
- [20] R. Melik, E. Unal, N. K. Perkgoz, B. Santoni, D. Kamstock, C. Puttlitz and H. V. Demir, “Nested Metamaterials for Wireless Strain Sensing”, *IEEE Journal of Selected Topics in Quantum Electronics*, Vol. 16, No. 2, 2010
- [21] C. A. Balanis, “Advanced Engineering Electromagnetics”, John Wiley & Sons, 1989
- [22] I. Bahl, “Lumped Elements for RF and Microwave Circuits”, Artech House, Boston-London, 2003
- [23] A. Elhavi, J. Stiens, C. De Tandt, W. Ranson and R. Vounckx, “An Equivalent Circuit Model of Single Circular Open-Ring Resonators”, *IEEE Journal of Selected Topics in Quantum Electronics*, vol. 16, No. 2, 2010
- [24] Lung-Hwa Hsieh and K. Chang, “Equivalent Lumped Elements G, L, C and unloaded Q’s of Closed- and Open-Loop Ring Resonators”, *IEEE Transactions on Microwave Theory and Techniques*, vol.50, no.2, 2002
- [25] <http://niremf.ifac.cnr.it/tissprop/htmlclie/htmlclie.htm>
- [26] <http://transition.fcc.gov/oet/rfsafety/dielectric.html>
- [27] V. Acikel, “Modeling of Radio Frequency Induced Currents on Lead Wires During MR Imaging Using a Modified Transmission Line Method (MoTLiM)”, MS. Thesis, 2010
- [28] E. Atalar, P. A. Bottomley, O. Ocali, L. C. L. Correia, M. D. Kelemen, J. A. C. Lima, E. A. Zerhouni, “High Resolution Intravascular MRI and MRS by Using Catheter Receiver Coil”, *Magnetic Resonance in Medicine*, 36, 596-605 (1996)
- [29] M. M. Ahmad, R. R. A. Syms, I. R. Young, B. Mathew, W. Casperz, S. D. Taylor-Robinson, C. A. Wadsworth and W. M. W. Gedroyc, “Catheter-based

---

flexible microcoil RF detectors for internal magnetic resonance imaging”,  
Journal of Micromechanics and Microengineering, 19 (2009), 074011

[30] R. R. A. Syms, I. R. Young, M. M. Ahmad, M. Rea, C. A. Wadsworth and S. D. Taylor-Robinson, “Thin-Film Detector System for Internal Magnetic Resonance Imaging”, Sensors and Actuators A: Physical, 163 (2010), 15-24

[31] J. J. Allen, “Micro-Electro-Mechanical System Design”, Taylor & Francis Group, LLC, 2005

[32] [www.microchemicals.com/photoresist/photoresist\\_az\\_5214\\_e\\_eng.htm](http://www.microchemicals.com/photoresist/photoresist_az_5214_e_eng.htm)

[33] S. Franssila, “Introduction to microfabrication”, J. Wiley, c 2004

[34] <http://www.microchem.com/Prod-SU83000.htm>

[35] [http://www2.dupont.com/Kapton/en\\_US/](http://www2.dupont.com/Kapton/en_US/)

[36] J.B. Pendry, A.J. Holden, D.J. Robbins and W.J. Stewart, “Magnetism from Conductors and Enhanced Nonlinear Phenomena”, IEEE Transactions on Microwave Theory and Techniques, Vol. 47, No. 11, 1999

[37] M. C. K. Wiltshire, J. B. Pendry, I. R. Young, D. J. Larkman, D. J. Gilderdale and J. V. Hajnal, “Microstructured Magnetic Materials for RF Flux Guides in Magnetic Resonance Imaging”, Science, Vol. 291, 2001

[38] M. J. Freire, R. Marques and L. Jelinek, “Experimental demonstration of a  $\mu=-1$  metamaterial lens for magnetic resonance imaging”, Applied Physics Letters, 93, 231108, 2008

[39] M. A. Lopez, M. J. Freire, J. M. Algarin, V. J. Behr, P. M. Jakob, “Nonlinear split-ring metamaterial slabs for magnetic resonance imaging”, Applied Physics Letters, 98, 133508, 2011

---

[40] H. H. Quick, M. O. Zenge, S. Massing, M. E. Ladd, “Wireless active catheter visualization: Passive decoupling methods and their impact on catheter visibility”, Proc. Intl. Soc. Mag. Reson. Med. 13 (2005)

[41] H. Celik, “Novel RF Coil Technologies for MRI”, MS. Thesis, June 2006